

ELECTRON DIFFRACTION FROM TWO DIMENSIONAL MATERIALS

Yu Xiang

Submitted in Partial Fulfillment of the Requirements
for the Degree of

DOCTOR OF PHILOSOPHY

Approved by:

Dr. Gwo-Ching Wang, Chair
Dr. Toh-Ming Lu, Co-Chair
Dr. Humberto Terrones
Dr. Jian Shi



Department of Physics, Applied Physics and Astronomy
Rensselaer Polytechnic Institute
Troy, New York

[December 2019]
Submitted December 2019

© Copyright 2019

By

Yu Xiang

All Rights Reserved

TABLE OF CONTENTS

LIST OF TABLES.....	v
LIST OF FIGURES	vi
ACKNOWLEDGEMENT	xv
ABSTRACT.....	xvii
1. INTRODUCTION	1
1.1 Motivation.....	1
1.2 Diffraction Basics	3
1.3 Experimental Methods	5
1.3.1 Synthesis	5
1.3.1.1 Chemical Vapor Deposition (CVD) Growth of Epitaxial Graphene .	5
1.3.1.2 Graphene Transfer.....	6
1.3.1.3 Metal Organic Vapor Deposition (MOCVD) Growth of MoS ₂	6
1.3.1.4 Thermal Evaporation Deposition of SnS	7
1.3.1.5 Vapor Transport Deposition (VTD) Growth of CdTe	8
1.3.1.6 Exfoliation of CdTe Film From Mica	10
1.3.2 Characterization	12
1.3.2.1 Atomic Force Microscopy (AFM)	12
1.3.2.2 Reflection High-Energy Electron Diffraction (RHEED) and Azimuthal RHEED	14
1.3.2.3 High-Resolution Low-Energy Electron Diffraction (HRLEED)	14
1.3.2.4 X-ray Diffraction (XRD).....	17
1.3.2.5 Transmission Electron Microscopy (TEM)	17
1.3.2.6 Other Characterization Techniques.....	18
1.4 Calculation and Simulation.....	19
1.4.1 Geometrical Superlattice Area Mismatching (GSAM).....	19
1.4.2 Density Functional Theory (DFT) Calculations	20
2. ARHEED CHARACTERIZATION OF GRAPHENE	21
2.1 Introduction.....	21
2.1.1 Motivation.....	21
2.1.2 Background of RHEED 2D Texture Analysis	22
2.2 Experimental.....	25
2.2.1 Graphene Growth and Transfer	25
2.2.2 RHEED Data Collection	26
2.3 Results and Discussion	26
2.3.1 Commercial Graphene	26
2.3.1.1 SEM and AFM	26
2.3.1.2 RHEED.....	27
2.3.2 Homemade Epitaxial Graphene	33
2.3.2.1 SEM, AFM and EBSD	33
2.3.2.2 RHEED.....	37
2.4 Conclusion	44
3. ARHEED CHARACTERIZATION OF TRANSITION METAL DICHALCOGENIDES ..	45
3.1 Introduction.....	45
3.2 Results and Discussion	47

3.2.1	MoS ₂ -Sapphire Interface.....	47
3.2.2	3D Reciprocal Space Map	56
3.3	Conclusion	67
4.	HRLEED CHARACTERIZATION OF EPITAXIAL GRAPHENE ON COPPER(111)	70
4.1	Introduction.....	70
4.2	Experimental	71
4.2.1	Sample Holder Design	71
4.2.2	Calibration.....	72
4.2.3	Instrument Response.....	75
4.3	Results and Discussion	76
4.3.1	AES and AFM.....	76
4.3.2	HRLEED.....	78
4.4	Conclusion	84
5.	RHEED CHARACTERIZATION OF THIN FILMS GROWN VIA VAN DER WAALS EPITAXY	85
5.1	Introduction.....	85
5.2	van der Waals Epitaxy of SnS on Graphene	87
5.2.1	SEM, AFM and EBSD.....	87
5.2.2	XRD and Pole Figure.....	91
5.2.3	RHEED	94
5.3	van der Waals Epitaxy of CdTe on Mica.....	99
5.3.1	AFM and RHEED.....	99
5.3.2	HRLEED.....	101
5.4	Conclusion	101
6.	FUTURE WORK.....	104
	REFERENCES	106
	APPENDIX A: 1D INCOMMENSURATE DOMAIN MODEL - ANALYTICAL SOLUTION	119
	APPENDIX B: 2D INCOMMENSURATE DOMAIN MODEL - NUMERICAL SIMULATION	123
	APPENDIX C: EFFECT OF INNER POTENTIAL ON THE RHEED PATTERNS	126
	APPENDIX D: HRLEED PATTERN AND IV SIMULATION FROM MONOLAYER CADMIUM TELLURIDE.....	128

LIST OF TABLES

Table 2.1: Theoretical prediction of peak positions and experimentally measured peak positions and FWHMs of peaks	30
Table 3.1: Literature reported CVD grown ML MoS ₂ to sapphire distances	56
Table 4.1: A comparison between ARHEED and HRLEED.....	70
Table 4.2: Atomic concentration analysis of graphene/Cu(111)/spinel sample from the AES spectrum shown in Fig. 4.4(a).....	77

LIST OF FIGURES

Figure 1.1: (a) Wave scattering parameters and conditions from a 2D lattice. (b) The plane-like Ewald sphere (red plane) cut of the reciprocal rods	4
Figure 1.2: (a) A schematic of the thermal evaporator setup. Major components are labeled by numbers. 1. Glass chamber wall, 2. Substrate holder, 3. Substrate, 4. Source boat holder, 5. SnS powder source, 6. Light reflector, 7. Halogen lamp, 8. Substrate clamp, 9. Thermocouple wires, 10. Alumina coated tungsten basket. (b) A schematic of SnS layer on graphene/SiO ₂ /Si(100) substrate	8
Figure 1.3: A schematic of the VTD setup: 1. Ar gas cylinder, 2. Mass flow controller, 3. Multi-channel controller, 4. Valve, 5. Quartz tube (OD = 5.5 cm), 6. Three-zone furnace, 7. Alumina boat containing the CdTe source powders, 8. Mica substrate, 9. Graphite support, 10. Lint free cleanroom wipe, 11. Cooling water case, 12. Digital pressure gauge, 13. Valve, 14. Cooling water tube, 15. Flex hose, 16. Mechanical pump, 17. Furnace temperature and ramping rate controller. The thermocouples are embedded inside the furnace.	9
Figure 1.4: A schematic showing the process of CdTe exfoliation from a mica substrate: 1. Vapor transport deposition growth of CdTe film on a mica substrate, 2. Spin coating a thin layer of epoxy on the CdTe film with 5000 RPM for 1 minute, then cure the epoxy on a hot plate at 150 °C for 8 minutes, 3. Spin coating a thin layer of epoxy on the Si wafer with 5000 RPM for 1 minute, 4. Flip the spin coated CdTe/mica sample and attach it to the spin coated Si wafer. Apply a gentle force to make sure they make a good contact, 5. Cure the layer of epoxy on Si on a hot plate at 150 °C for 8 minutes, then cut away the edge parts of the mica substrate, 6. Slowly put the whole sample with an inclined angle into a Petri dish filled with water. Try it several times until mica starts to detach from the CdTe film at the edge, 7. Peel off the mica substrate to reveal the flat CdTe surface.	11
Figure 1.5: (a) van der Waals interaction force vs. tip-surface distance for a typical AFM. (b) Vibration amplitude vs. drive frequency with and without a tip-surface interaction.	13
Figure 1.6: (a) Schematic of the RHEED system: 1. X-axis micrometer, 2. Y-axis micrometer, 3. Z-axis micrometer, 4. Azimuthal rotation manipulator, 5. Tilt micrometer, 6. Vacuum chamber, 7. Phosphor scree, 8. Stainless steel vacuum hose to the turbo pump, 9. Electron gun, 10. Digital camera, 11. X-ray photoelectron spectroscopy (XPS) cylindrical mirror analyzer, 12. Ion pump. (b) Schematic of the sample holder for the RHEED system: 1. Central shaft, 2. Stepping motor, 3. Stepping motor shaft, 4. Sample tilt-adjust screws, 5. Sample tilt-adjust stage, 6. Sample.	15
Figure 1.7: (a) A schematic of a conventional LEED electron optics: 1. Electron gun, 2. Phosphor screen, 3. Screen grids, 4. Sample. (b) A schematic of the HRLEED optics: 1. Electron gun, 2. Channeltron detector, 3. Phosphor screen, 4. Screen grids, 5. Screen octupole, 6. Crystal octupole, 7. Crystal lens, 8. Sample. (c) A schematic of the HRLEED vacuum chamber layout: 1. View port, 2. Ion gun, 3. Stainless steel vacuum hose, 4. Cylindrical mirror analyzer (CMA) for Auger electron spectroscopy (AES), 5. Tungsten filament, 6. Sample holder housing, 7. Sample, 8. Ion gauge, 9. View port, 10. Channeltron detector, 11. Phosphor screen, 12. Electron gun, 13. View port.	16

Figure 2.1: (a) A schematic of the reciprocal space structure of a 2D hexagonal lattice, (b) a schematic showing how the Ewald sphere cuts through the reciprocal rods. The curly red arrow represents the rotation around the sample normal direction at various azimuthal angle φ , (c) a simulated RHEED pattern, and (d) a schematic of the 2D reciprocal space structure of a 2D hexagonal lattice looking into the negative k_z direction. 23

Figure 2.2: (a) A schematic of the real space structure of a 2D material consisted of randomly oriented grains. The curved red arrows represent random rotated grains and the straight up pointing green arrows represent the direction perpendicular to the substrate. (b) A schematic showing the 3D reciprocal space structure of the 2D material and how it cuts through the Ewald sphere, the curly red arrow represents the rotation around the sample normal direction at various azimuthal angle φ . (c) A simulated RHEED pattern, and (d) a schematic of the 2D reciprocal space structure of the 2D material with randomly oriented grains. 24

Figure 2.3: (a) An SEM image and (b) an AFM image showing different areas of the graphene surface. The arrows in both figures indicate bi-layer graphene islands. The z-scale bar indicating the surface height in the AFM image is shown on the right side of AFM image. The AFM line scan is represented by a white dashed line in (b). The darker wavy lines in (a) and brighter wavy lines in (b) are grain boundaries. The faint wavy lines in (a) and (b) are wrinkles in graphene. 27

Figure 2.4: (a) A RHEED pattern collected from a commercial graphene sample with the 20 keV electron beam incident at $\varphi = 0.0^\circ$. The yellow coordinate system is centered at the straight through (S.T.) spot. The k_{\parallel} axis and k_{\perp} axis are parallel and perpendicular to the shadow edge, respectively. The inset in (a) shows an intensity line scan along the k_{\perp} axis. The black squares in (b) show the experimentally measured intensity along the k_{\parallel} axis, $I(k_{\parallel})$. The seven fit peaks and the cumulative fit peak are plotted in different colors. The peak number and the corresponding color are shown in the legend. 28

Figure 2.5: (a) The RHEED 2D reciprocal space structure measured from the commercial graphene sample. (b) The theoretical 2D reciprocal space structure of the graphene layer. The cyan spots are 2D reciprocal lattice points of a single crystal graphene with the corresponding (hk) indices labeled. The yellow spots are rotated 30° from the cyan spots with the k_{\perp} direction as the rotation axis. $k_x = k_{\parallel} \sin \varphi$ and $k_y = k_{\parallel} \cos \varphi$. The arrows on the right side indicate the in-plane directions for graphene, $[2\bar{1}\bar{1}0]$ and $[01\bar{1}0]$ along $\varphi = 0^\circ$ and 90° , respectively. (c) and (d) show the $I(k_{\parallel}, \text{inner})$ and $I(k_{\parallel}, \text{outer})$ plotted in the polar coordinate system. These intensity distributions of the inner peaks and outer peaks are extracted from the RHEED 2D reciprocal space structure in (a). 31

Figure 2.6: (a) SEM image of the Cu film without twin domains on a sapphire(0001) substrate after thermal annealing and graphene growth; overlay shows a Raman spectrum acquired from this sample. G and 2D peaks are labeled in the spectrum. (b) EBSD crystallographic orientation map of the Cu film without twin domains on a sapphire(0001) after thermal annealing and graphene growth using IPF-Z mapping component. (c) EBSD Cu{111} pole figure of the Cu film without twin domains on a sapphire(0001) after thermal annealing and graphene growth. (d) SEM image of the Cu film with twin domains on a sapphire(0001) substrate after thermal annealing and graphene growth; overlay shows a Raman spectrum acquired from this sample. (e) EBSD crystallographic orientation map of the Cu film with twin domains on a sapphire(0001) substrate

after thermal annealing and graphene growth using IPF-Z mapping component. (f) EBSD Cu {111} pole figure of the Cu film with twin domains on a sapphire(0001) after thermal annealing and graphene growth..... 34

Figure 2.7: (a) Optical image of the continuous monolayer graphene sheet transferred to a SiO₂/Si substrate. (b) Collected Raman spectra from random areas on the continuous monolayer graphene sheet transferred to a SiO₂/Si substrate. (c) SEM image of the monolayer graphene sheet transferred to a SiO₂/Si substrate. (d) AFM image and (e) three line scan profiles across the wrinkles in the monolayer graphene transferred to a SiO₂/Si substrate. 36

Figure 2.8: (a, b) RHEED patterns of the monolayer graphene on a twin-free Cu(111) film when the electron beam incident at azimuthal angles $\varphi = 0$ and 30.6°, respectively. The two-dimensional Miller index (hk) is labeled in (a) and (b). The \vec{b}_1 and \vec{b}_2 are unit vectors in the reciprocal space. The scale bar is 5 Å⁻¹. (c) Schematics showing the directions of blue and red dashed lines in the reciprocal space (RHEED patterns) of a monolayer graphene shown in (a) and (b), respectively. (d) Intensity profiles along the blue and red dashed lines in (a) and (b), respectively. (e) Experimentally acquired reciprocal space structure of the monolayer graphene on a twin-free Cu(111) film. The (hk) pole locations are labeled and circled by dashed circles. (f) Experimentally acquired reciprocal space structure of the monolayer graphene on a twinned Cu(111) film..... 38

Figure 2.9: (a) Optical image of the bilayer graphene sheet transferred from a twinned Cu(111) film to a SiO₂/Si substrate. (b) Optical image of the multilayer graphene sheet transferred from a twinned Cu(111) film to a SiO₂/Si substrate. The dashed outlines are speculated to reflect the twin boundaries in Cu films. 40

Figure 2.10: (a) RHEED pattern of the monolayer graphene transferred to a SiO₂/Si substrate collected at the azimuthal angle $\varphi = 59.4^\circ$. (b) Experimentally acquired reciprocal space structure of the monolayer graphene transferred to a SiO₂/Si substrate. (c, d) Decomposition of (b) to show (c) inner six spots and (d) outer six spots. 41

Figure 2.11: (a) RHEED pattern of the multilayer graphene transferred to a SiO₂/Si substrate collected at the azimuthal angle $\varphi = 180^\circ$. (b) Experimentally acquired reciprocal space structure of the multilayer graphene transferred to a SiO₂/Si substrate. (c) Intensity profiles vs momentum transfer perpendicular to the substrate (k_\perp) along the yellow dashed lines in RHEED patterns shown in Figure 2.10(a) and Fig. 2.11(a). S.T. stands for the straight through incident electron beam landed on the phosphorus screen. (d) Peak fitting of the intensity profile in the lower part of (c) after background subtraction..... 42

Figure 3.1: RHEED patterns along (a) ZA = [21̄10] and (b) ZA = [101̄0]. The Miller index for each visible diffraction streak is labeled. The horizontal dashed line indicates the shadowing edge. The two arrows perpendicular to each other represents the k_{\parallel} and k_{\perp} directions. (c) and (d) Line profiles scanned along k_{\parallel} direction in the corresponding RHEED patterns shown in (a) and (b), respectively. The inset illustrates the scan direction (the dashed line) in the reciprocal lattice (the red dots) with base vectors a^* and b^* . The ZA direction is indicated with a long arrow with Miller index labeled. (e) and (f) Line profiles scanned along the k_{\perp} direction in the corresponding RHEED patterns shown in (a) and (b). The upper part of each figure shows the raw data (solid curve) and

the smooth background (dashed curve) while the lower part shows the curve after the background subtraction..... 48

Figure 3.2: The cross-section views of (a) HAADF-STEM and (c) HRTEM images along the [1̄100] zone axis of sapphire from the MoS₂/sapphire interface without any image processing. Zoomed-in view (b) HAADF-STEM and (d) HRTEM images from the yellow square denoted in (a) and (c), respectively. (e) The DFT calculated atomic structure of a ML MoS₂ on a S passivated sapphire. The vertical distances are labeled on this schematic. An atomic ball model of the structure in (e) has been superposed on (d) to demonstrate the close match between theory and experiment. 50

Figure 3.3: (a) HAADF-STEM image and (b) a combined EDX mapping from the MoS₂/sapphire interface. Individual EDX mapping from (c) Mo, (d) S, (e) Al and (f) O elements..... 50

Figure 3.4: A series of simulated RHEED (a) intensity of specular diffraction spot and (b) the corresponding Fourier transform along k_{\perp} direction with various electron penetration depth. (c) The DFT calculated atomic structure of a ML MoS₂ on a S passivated sapphire. The penetration depths are color coded and indicated by the dashed arrows connecting (b) and (c)..... 52

Figure 3.5: (a) The AFM image from the MoS₂/sapphire surface showing three distinct regions corresponding to the S passivated sapphire surface, 1 ML and 2 ML MoS₂. The four colored dashed lines indicate where the line profiles are extracted from. (b) An atomic ball model showing 1 ML MoS₂ and 2 ML MoS₂ on a stepped sapphire surface with a S passivation layer at the interface. Some typical vertical distances are labeled on the figure. (c) The height distribution of the AFM image shown in (a). (d) and (e) AFM line profiles scanned across MoS₂ islands and the sapphire terraces. The curves are plotted in four different colors in accordance with the colors used in (a). 53

Figure 3.6: (a) The fast Fourier transform image of the AFM image shown in Fig. 3.5(a). Two bright spots show up at $R = 14.3 \mu\text{m}^{-1}$ from the center. Therefore, the corresponding real space periodicity is $L = 1/R \approx 70 \text{ nm}$, which corresponds to the average sapphire terrace width. (b) The slope distribution of the AFM image shown in Fig. 3.5(a), plotted as the probability density distribution ρ of the inclination angle from the horizontal plane..... 54

Figure 3.7: (a) A snapshot of the 3D reciprocal space map measured by ARHEED from MoS₂/sapphire. (b) Experimentally constructed ARHEED 2D reciprocal space map sliced from (a) at $k_z = 3.97 \text{ \AA}^{-1}$. The radial axis represents the momentum transfer parallel to the surface (k_{\parallel}) and the azimuthal angle ranges from 0° to 360°. (c) GIXRD azimuthal scans from sapphire {11̄20} (upper) and MoS₂ sapphire {11̄20} (lower). Their peaks line up, which implies a parallel epitaxial relationship: [11̄20]_{MoS₂} || [11̄20]_{sapphire}. (d) The theoretical simulation of the 2D reciprocal space map from MoS₂. Some low order Miller indices are labeled on (d)..... 57

Figure 3.8: (a) A bubble plot of ΔA vs. ϕ_R resulting from the GSAM simulation of MoS₂ on c-sapphire. The range of ϕ_R is chosen from 0 to 60°, because both basal planes of TMDC and c-sapphire have a six-fold symmetry and thus the simulation result repeats itself every 60°. In the plot, the diameter of a bubble is inversely proportional to the area of superlattice A_1 (A_2). A small

ΔA or a small area of superlattice (large bubble) means a high probability of observing a superlattice at the corresponding ϕ_R . The favorable ϕ_R values occur at $0^\circ, 10.9^\circ, 19.1^\circ, 40.9^\circ, 49.1^\circ$, and 60° . The atomic ball model of MoS₂ overlay on c-sapphire at (b) $\phi_R = 0^\circ$ and $\phi_R = 60^\circ$, (c) $\phi_R = 10.9^\circ$ and $\phi_R = 49.1^\circ$ and (d) $\phi_R = 19.1^\circ$ and $\phi_R = 40.9^\circ$. The MoS₂ domains aligned along these two ϕ_R are twin to each other. The yellow dashed parallelograms represent the superlattices formed under such conditions. 58

Figure 3.9: (a) A slice of the measured HWHMs of the (00) spot vs. azimuthal angle at a fixed $k_\perp = 3.97 \text{ \AA}^{-1}$ from the ML MoS₂/sapphire. The red and blue curves are before and after deconvolution with instrument response and the mosaic tilt induced broadening, respectively. The in-plane directions of MoS₂ were indicated by the two arrows in (a). The average HWHM before and after deconvolution are $0.46 \pm 0.05 \text{ \AA}^{-1}$ and $0.43 \pm 0.05 \text{ \AA}^{-1}$, respectively. (b) The intensity profile along the k_x direction for a series of γ values ranging from 0 to 0.25 calculated from the 1D incommensurate domain model. (c) The HWHM of the (10) spot as a function of the diameter of the incommensurate domain calculated from the 1D model (the blue squares) and the 2D model (the red squares). (d) The simulated 2D reciprocal space map from MoS₂/sapphire using the 2D model with nucleation density $\rho = 0.1$ or domain diameter $D = 2.0 \pm 0.5 \text{ nm}$. The (00) and (10) spots are labeled on the figure..... 60

Figure 3.10: RHEED patterns taken from (a) epitaxial graphene/Cu(111) and (c) MoS₂/sapphire samples using 20 keV electrons. (b)(d) The square of half-width-at-half-maximum (h^2) plotted as a function of k_\perp^2 for the central diffraction streaks from (a) and (c), respectively. The instrument response is determined to be $h_{inst} = \sqrt{0.011 \pm 0.002} \text{ \AA}^{-1} = 0.10 \pm 0.01 \text{ \AA}^{-1}$ from graphene/Cu(111) and the mosaic tilt induced broadening for MoS₂/sapphire is $|k_\perp| \tan(\theta/2) = 0.17 \text{ \AA}^{-1}$ 59

Figure 3.11: (a) Photoluminescence (PL) and (b) Raman spectrum from the MoS₂/sapphire sample. The strong PL peak at $\sim 1.9 \text{ eV}$ and the absence of LA(M) peak in Raman spectrum indicate that few point defects exist in the MoS₂. 61

Figure 3.12: Simulated (00) spots using Spadacini's theory for the atomic scattering intensities from stepped surfaces with different step atom densities (σ): (a1) $\sigma = 0.1\%$, (a2) $\sigma = 0.2\%$, (a3) $\sigma = 0.5\%$, (a4) $\sigma = 1.0\%$, (a5) $\sigma = 1.5\%$ and (a6) $\sigma = 2.0\%$, respectively. The scale bar in each figure is 0.05 \AA^{-1} . (b) The relationship between the peak's HWHM and the step atom density summarized from (a1-a6). 63

Figure 3.13: (a) A RHEED pattern of MoS₂ on sapphire substrate taken at azimuthal angle $\varphi = 118.8^\circ$. (b) The integrated intensity $I(k_\parallel)$ along the red dashed line in (a) plotted in parallel momentum transfer k_\parallel direction. Peaks are labeled by Miller indices $(2\bar{2}), (1\bar{1}), (00), (\bar{1}1), (\bar{2}2)$, The average reciprocal separation Δk_\parallel of adjacent peaks is $2.27 \pm 0.06 \text{ \AA}^{-1}$. For hexagonal lattice: $|\vec{G}(hk)| = 4\pi/\sqrt{3}a \times \sqrt{h^2 + hk + k^2}$, where a is bulk in-plane lattice constant of MoS₂ = 3.1500 \AA . Theoretically, $|\vec{G}(\bar{1}1)| = 2.3 \text{ \AA}^{-1}$, which is in good agreement with our measurements of $2.27 \pm 0.06 \text{ \AA}^{-1}$. From the experimental value, the in-plane lattice constant of MoS₂ is determined to be $a = 3.19 \pm 0.06 \text{ \AA}$. (c) The integrated intensity $I(k_\perp)$ along the blue dashed line in (a) plotted in perpendicular momentum transfer k_\perp direction. Peak at $k_\perp = 0$ is from straight through beam (S.T.). Two peaks (labeled 1 and 2) are result of constructive interference between MoS₂ monolayer and

the substrate. The reciprocal space separation Δk_{\perp} of the two adjacent peaks is $2.36 \pm 0.04 \text{ \AA}^{-1}$ and the vertical distance between MoS₂ monolayer and the sapphire is determined to be $d = 2\pi/\Delta k_{\perp} = 2.66 \pm 0.06 \text{ \AA}$. (d) Experimentally constructed RHEED 2D reciprocal space map of MoS₂ monolayer plotted as the intensity $I(k_{||}, \varphi)$ contour map in polar coordinate system. RHEED 2D reciprocal space structure exhibits a 6-fold symmetry and agrees with (e) the theoretical simulation viewed along the [0001] direction of MoS₂, suggesting that the monolayer of MoS₂ is single crystal. (f) Experimentally measured half-width-at-half-maxima (HWHM) of the MoS₂ (00) in-phase diffraction spot in polar coordinate system. The radial and angular axes represent HWHM and the azimuthal angle φ , respectively. The (00) spot exhibits slightly broadening along $<11\bar{2}0>$ direction with a value of $\sim 0.6 \text{ \AA}^{-1}$ and the minimum broadening is $\sim 0.4 \text{ \AA}^{-1}$ 65

Figure 3.14: (a) A RHEED pattern of WS₂ on sapphire taken at azimuthal angle defined as $\varphi = 64.8^\circ$. (b) The integrated intensity $I(k_{||})$ along the red dashed line in (a) plotted in parallel momentum transfer $k_{||}$ direction. Peaks are labeled by Miller indices $(\bar{0}1)$, (00) and (01) . The average reciprocal separation $\Delta k_{||}$ of adjacent peaks is $2.17 \pm 0.07 \text{ \AA}^{-1}$. The bulk in-plane lattice constant of WS₂ is $a = 3.1532 \text{ \AA}$. Theoretically, $\Delta k_{||} = |\vec{G}(01)| = 2.21 \text{ \AA}^{-1}$, which is in good agreement with our measurements of $2.17 \pm 0.07 \text{ \AA}^{-1}$. From the experimental value, the in-plane lattice constant of WS₂ is determined to be $a = 3.34 \pm 0.07 \text{ \AA}$. (c) The integrated intensity $I(k_{\perp})$ along the blue dashed line in (a) plotted in perpendicular momentum transfer k_{\perp} direction. Peak at $k_{\perp} = 0$ is from straight through beam. Two peaks (labeled 1 and 2) are result of constructive interference between WS₂ monolayer and the substrate. The reciprocal separation Δk_{\perp} of the two adjacent peaks is $2.29 \pm 0.04 \text{ \AA}^{-1}$ and the vertical distance between WS₂ monolayer and the sapphire is determined to be $d = 2\pi/\Delta k_{\perp} = 2.74 \pm 0.05 \text{ \AA}$. (d) Experimentally constructed RHEED 2D reciprocal space map of WS₂ monolayer plotted as the intensity $I(k_{||}, \varphi)$ contour map in polar coordinate system. RHEED 2D reciprocal space structure exhibits a 6-fold symmetry and agrees with (e) the theoretical simulation viewed along the [0001] direction of WS₂, suggesting that the monolayer of WS₂ is single crystal. (f) Experimentally measured HWHMs of the WS₂ (00) in-phase diffraction spot in polar coordinate system. The radial and angular axes represent HWHM and the azimuthal angle φ , respectively. The (00) spot exhibits slight broadening along the $<11\bar{2}0>$ direction with a HWHM value of $\sim 0.5 \text{ \AA}^{-1}$ and the minimum broadening is $\sim 0.4 \text{ \AA}^{-1}$ 66

Figure 3.15: (a1-f1) The generated circular-shape epilayer lattices of diameter $D = 70 \text{ nm}$, (a2-f2) the 5×5 zoom-in views of the corresponding lattices, (a3-f3) the size distributions, (a4-f4) simulated 2D reciprocal space intensities $I(k_x, k_y, k_z = 0)$ and (a5-f5) the simulated 2D intensities around (10) spot (the scattered points) and their Gaussian surface fit (blue at low intensity and red at high intensity) from the numerical simulations using nucleation density $\rho = 0.01, 0.02, 0.05, 0.10, 0.15$ and 0.20 , respectively. The scale bars in (a2-f2) are all of 2 nm . The mean and standard deviation of the sized distributions are labeled on each of the (a3-f3) figures, showing a descending trend as ρ becomes larger. The scale bars in (a4-f4) are all of 1 \AA^{-1} . The HWHMs are determined for the (10) spots by Gaussian fit and labeled on the top each of (a5-f5)..... 68

Figure 4.1: (a) Schematics of the disassembled parts of the sample holder: 1. Stainless steel nuts, 2. Tantalum strips, 3. Sample, 4. Tantalum shield, 5. Stainless steel bolts, 6. Tungsten filament, 7. Ceramic tubes, 8. Ceramic bolts, 9. Ceramic washers, 10. Stainless steel bolt, 11. Stainless steel sample housing, 12. Stainless steel shaft. (b) Schematic of the assembled sample holder. (c) Top-

view and (d) bottom-view of the sample holder. (e) Schematic of the “pancake” tungsten filament with dimensions written. (f) Front view of the sample housing shield and two tantalum strips with dimensions labeled..... 73

Figure 4.2: (a) Room temperature experimental HRLEED pattern of Si(111) (7×7) reconstruction taken at an incident energy of 126.5 eV. (b) HRLEED pattern after the subtraction of background intensity. The red crosses are positions of experimental spots in (a) and the yellow crosses are theoretical peak positions. Deviations between red and yellow crosses in the (c) x and (d) y directions, respectively. (e) A map of the discrete deviation vector field. The units of the k_x (horizontal) and k_y (vertical) axes are in units of pixels. (f) HRLEED pattern after the correction of the experimental spots using the deviation field. The experimental spot positions and theoretical spot positions are coincident. The units of the k_x and k_y axes are in percentages of Brillouin zone (%BZ). 74

Figure 4.3: HRLEED line scan from the Si(111) surface collected at 126.5 eV along the [1010] direction. The black curve shows the profile after the distortion correction and background removal. The blue labels are the primary Miller indices from the Si(111) hexagonal lattice. The colored curves are the fitted pseudo-voigt profile for each peak. The red labels are the FWHMs of each peak in the unit of %BZ..... 76

Figure 4.4: (a) AES spectrum from the graphene/Cu(111)/spinel sample surface before (blue curve) and after (red curve) the annealing at 500 °C for one hour. Auger peaks corresponding to the silicon LMM, sulfur LMM, carbon KLL and oxygen KLL transitions are labeled on the figure. AFM images measured *ex situ* from the graphene/Cu(111)/spinel sample surface (b) before and (c) after the annealing. The scale bars are both 10 μm..... 77

Figure 4.5: (a) Room temperature HRLEED pattern of the graphene/Cu(111)/spinel sample taken at 181 eV incident electron energy after one hour *in situ* annealing at 500 °C. The two arrows in (a) indicate the directions of [1010] and [0110]. (b) HRLEED intensity line profiles in units of pixels scanned along the [1010] direction with electron energies varying from 119 to 210 eV. (c) A portion of the intensity line scans extracted from (b), showing only the intensity line profiles near the (00) and (10) spots for energies ranging from 119 to 135 eV. The corresponding Miller indices are labeled above each peak. The (10) peak splits into two parts: (10)_{Cu} from Cu(111) and (10)_G from graphene. (d) The fitted FWHMs for the (00), (10)_{Cu}, (10)_G peaks and the calculated relative lattice constant difference between Cu(111) and graphene at various incident electron energies. 79

Figure 4.6: (a) Intensity *vs.* electron energy (IV) curves and (b) FWHM *vs.* electron energy curves measured at the (00) peak of the graphene/Cu(111)/spinel sample. The peak intensity or FWHM in those three curves are extracted from the fitting results of the HRLEED intensity line profiles scanned along [1010], [1120] and [0110] directions, respectively. (c) IV and (d) FWHM *vs.* electron energy curves measured at (10), (11), and (01) peaks in a similar way as (a) and (b). .. 80

Figure 4.7: RHEED pattern from an HOPG sample using 20 keV electrons (a) without and (b) with the simulated (00l) spots superposed on it. (c) Simulated LEED IV curves for a series d values ranging from 3.4 Å to 3.6 Å with a step size of 0.005 Å..... 83

Figure 5.1: SEM top-view images of (a) bare commercial polycrystalline graphene on SiO₂/Si(100), (b) bare homemade single crystal graphene on SiO₂/Si(100), (c) after the deposition of SnS film on the polycrystalline graphene, and (d) after the deposition of SnS film on the single crystal graphene. SEM cross-section view images of (e) SnS film on the polycrystalline graphene on SiO₂/Si(100) and (f) SnS film grown on the single crystal graphene on SiO₂/Si(100). AFM top-view images of (g) SnS film on the polycrystalline graphene and (h) SnS film on the single crystal graphene. The insets in (g) and (h) show zoomed-in views from small areas in (g) and (h), respectively..... 88

Figure 5.2 (a) EBSD IPF-Z crystallographic orientation map that shows the out-of-plane orientation in the SnS film on the homemade single crystal graphene. (b) IPF-X map which indicates the in-plane crystallographic orientations and unveils the grain boundaries in the SnS film grown on the single crystal graphene. The scale bars in (a) and (b) are 1 μ m. (c) grain boundary misorientation histograms indicating the grain boundary misorientation distributions in the SnS film grown on the single crystal graphene..... 90

Figure 5.3: (a) XRD θ vs 2θ scan from the SnS film deposited on the commercial polycrystalline graphene/SiO₂/Si(100) substrate and the intensity is plotted in a logarithmic scale. Inset a1: A zoomed-in view of the XRD θ vs 2θ scan of the SnS film within the range of $31.2^\circ < 2\theta < 32.2^\circ$ and the intensity is plotted in a linear scale. The profile contains (111) and (040) peaks. Inset a2: The XRD (040) rocking curve of the SnS film with the intensity plotted in a linear scale and 3-degree ω angular range. (b) The XRD θ vs 2θ scan from the SnS film deposited on the single crystal graphene/SiO₂/Si(100) substrate and the intensity is plotted in a logarithmic scale. Inset b1: A zoomed-in view of XRD θ vs 2θ scan of SnS film within the range of $31.5^\circ < 2\theta < 32.5^\circ$ and the intensity is plotted in a linear scale. Inset b2: The XRD (040) rocking curve of the SnS film with intensity plotted in a linear scale and 3-degree ω angular range. RHEED pattern using a 15 keV electron beam collected from (c) SnS film grown on the polycrystalline graphene/SiO₂/Si(100), and (d) SnS film deposited on the single crystal graphene/SiO₂/Si(100) substrates. In each RHEED pattern, (hkl) indices were labeled below diffraction spots. The out-of-plane directions in (c) and (d) are [111] and [010], respectively. The diamond and square unit mesh are outlined in blue dashed lines in (c) and (d), respectively. Insets in (c) and (d) show radial intensity vs reciprocal distance or perpendicular momentum transfer k_\perp along the direction perpendicular to the substrate. The red dashed rectangular box in the RHEED pattern indicates the area where the intensity is integrated. The (hkl) indices of peaks and rings are labeled..... 92

Figure 5.4: X-ray {160} pole figures with the (010) out-of-plane orientation measured from the SnS films grown on (a) the commercial polycrystalline graphene/SiO₂/Si(100) substrate, and (b) the homemade single crystal graphene/SiO₂/Si(100) substrate. (c) RHEED 2D reciprocal space structure measured from the single crystal graphene on SiO₂/Si(100) substrate. The black dashed circles are the theoretical positions of the reciprocal lattice points of a single crystal graphene. (d) RHEED azimuthal scan (upper curve) from single crystal graphene at $k_\parallel = 2.9 \text{ \AA}^{-1}$ and XRD SnS(160) azimuthal scan (bottom curve) taken at $2\theta = 53.443^\circ$ and $\chi = 23.311^\circ$. The corresponding (hk) indices of single crystal graphene are labeled above each peak in the RHEED azimuthal scan. Top view of the atomic structure at the SnS/graphene interface showing the epitaxial relationship: (e) $<100>_{\text{SnS}} // <\overline{2}\overline{1}10>_{\text{graphene}}$ and (f) $<100>_{\text{SnS}} // <10\overline{1}0>_{\text{graphene}}$. Note that $[10\overline{1}0]_{\text{graphene}}$ is rotated 30° from $[2\overline{1}10]_{\text{graphene}}$. Carbon, tin and sulfur atoms are represented by black, blue and yellow

balls, respectively. Two perpendicular arrows indicate the crystal directions of graphene (black) and SnS (blue) next to each atomic structure.	94
Figure 5.5: RHEED patterns from (a) the CdTe surface and (d) the CdTe interface revealed by the exfoliation. The Miller indices, the straight through (S.T.) spot and the zone axis (ZA) are labeled in both figures. A central dashed line is drawn on (a) to indicate the out-of-plane direction. AFM images from (b), (c) the CdTe surface and (e), (f) the CdTe interface. The unit in the color bars in (b), (c), (e) and (f) is nanometer.....	100
Figure 5.6: Photos of the CdTe interface /epoxy/Si sample mounted on the HRLEED sample holder (a) before and (b) after the <i>in situ</i> annealing at around 200 °C for ~4 hours. The positions of the CdTe film and the epoxy coated Si wafer are indicated in (a). (c) The AES spectrum from the surface of CdTe interface after annealing. The carbon KLL and oxygen KLL peak positions are labeled in (c).	102
Figure A1: Schematics of some different types 1D incommensurate domain boundaries for MoS ₂ forming parallel epitaxy with sapphire substrate with (a) no boundary, (b) boundary gap = 1.51 <i>b</i> , (c) boundary gap = 1.02 <i>b</i> and (d) boundary gap = 1.53 <i>b</i> , where <i>b</i> is the MoS ₂ lattice constant <i>b</i> = 3.15 Å. The vertical dashed lines represent where the epilayer lattice and substrate lattice line up.....	121
Figure B1: A flowchart for the numerical simulation used in the 2D incommensurate domain model.....	125
Figure C1: A schematic showing the RHEED geometry. <i>K</i> and <i>k</i> are the electron wave vectors inside and outside the crystal, respectively. θ_1 is the incident angle and θ_2 is the outgoing angle from the crystal surface. θ'_1 and θ'_2 are the incident angle and outgoing angle, respectively, from the plane by which the electron beam is diffracted inside the crystal.	127
Figure D1: Cross-section view atomic ball models for monolayer CdTe in (a) zincblende, (b) hexagonal and (c) DLHC structures. Top-view atomic ball models for monolayer CdTe in (d) zincblende, (e) hexagonal and (f) DLHC structures. The two arrows on the top-right corner indicate the directions of CdTe base vectors <i>b</i> and <i>c</i> . Simulated HR-LEED patterns for monolayer CdTe in (g) zincblende, (h) hexagonal and (i) DLHC structures.	129
Figure D2: Simulated I-V curves for monolayer CdTe in zincblende, hexagonal and DLHC structures. The center positions of some peak in the simulated curves are labeled on the figure.	129

ACKNOWLEDGEMENT

First, I'd like to express tremendous gratefulness to my advisor Professor Gwo-Ching Wang for not only sharing her experiences and knowledge with me but also instilling in me the spirits and altitudes as a scientist. I feel very honored and fortunate to be one of her students. I'd also like to thank Professors Toh-Ming Lu, Humberto Terrones and Jian Shi for providing valuable advices as well as serving as my thesis committee members.

Sincere thanks go to my lab mates and collaborators, past and present: Lukas Valdman, Poomirat Nawarat, Dr. Aaron Littlejohn, Dr. Yaobiao Xia, Dr. Zhaodong Li, Dr. Hichem Hattab, Dr. Yunbo Yang, Dr. Jatis Dash, Dr. Liang Chen, Dr. Xin Sun, Dr. Zonghuan Lu, Dr. Xixing Wen, Dr. Fawen Guo, Dr. Weiyu Xie, and Professor Morris Washington at RPI's Department of Physics, Applied Physics and Astronomy; Dr. Lu Li, Dr. Jian Gao, and Professor Nikhil Koratkar at RPI's Department of Mechanical, Aerospace and Nuclear Engineering; Dr. Dibyajyoti Mohanty and Professor Ishwara Bhat at RPI's Department of Electrical, Computer and Systems Engineering; Dr. Yiping Wang, Zhizhong Chen, Dr. Jie Jiang, and Lifu Zhang at RPI's Department of Materials Science and Engineering; Tianmeng Wang, Yanwen Chen and Professor Sufei Shi at RPI's Department of Chemical and Biological Engineering; Dr. Xiaotian Zhang, Dr. Tanushree Choudhury, Dr. Mikhail Chubarov, Dr. Fu Zhang, and Professors Joan Redwing, Joshua Robinson and Mauricio Terrones at The Pennsylvania State University; Yuan Ma and Professor Lei Gao at Beijing Advanced Innovation Center for Materials Genome Engineering; Ben Schoenek at Park Systems.

In addition, I'd like to thank the undergraduate students who have helped me with experiments and data analyses: Faye Lyons, Jiazhao Lin, Jiayu Liu, Tengteng Tao, Ray Xie and Joel Meese. I thank the staff at RPI's Center for Materials, Devices and Integrated Systems (Mr.

Bryant Colwill and Mr. David Frey), Center for Biotechnology and Interdisciplinary Studies (Dr. Joel Morgan) and Department of Materials Science and Engineering (Mr. Rob Planty) for helping me use the facilities. I thank the RPI Presidential Graduate Research Fellowship, the National Science Foundation (DMR-1305293) and the New York State Foundation of Science, Technology and Innovation through Focus Center (C150117) for providing the financial support.

I owe deep thanks to my lovely girlfriend Meiling Wang. I must be the luckiest person to have her in my life. I will be forever indebted to my parents for their guidance, discipline, support and love.

ABSTRACT

There has been an explosive growth in the study of two dimensional (2D) materials governed by van der Waals interaction in the last decade due to their novel electronic, electrical, optical, and magnetic properties that were not known or discovered in the past. Those properties are strongly affected by their structure and long-range order perfection. A thorough structural characterization of 2D materials is the central issue but it has been challenging due to the inherent limited amounts of atoms in 2D materials under study. Fortunately, electron interacts strongly with matters and allows structure and perfection of 2D materials to be studied. In this thesis the near surface sensitive azimuthal reflection high-energy electron diffraction (ARHEED) developed at Rensselaer Physics was applied for the first time to map out (1) 2D reciprocal space structures of single crystal graphene on amorphous SiO₂ and epitaxial Cu(111) substrates and (2) 3D reciprocal space structures of monolayer (ML) MoS₂ and ML WS₂ on sapphire(0001) substrates. The surface sensitive high-resolution low-energy electron diffraction (HRLEED) was used to compliment ARHEED to study single crystal graphene on Cu(111). Two application studies using RHEED and van der Waals substrates are also presented: (1) Single crystal graphene as a buffer layer to guide the growth of van der Waals epitaxial SnS film on amorphous SiO₂ substrate and (2) 3D CdTe epitaxial thin film on mica substrate.

Through quantitative analysis of the 2D reciprocal space map, one can extract real space properties of the 2D material including the symmetry, orientation domain distribution, lattice constants, interlayer spacing and average domain size. The 2D reciprocal space maps of graphene on Cu(111), homemade single crystal graphene transferred on SiO₂/Si substrate, and commercial polycrystalline graphene on SiO₂/Si substrate clearly show differences in their corresponding 2D maps that reveal their orientation domains and wafer scale quality. For MoS₂ the corresponding

3D map from ARHEED reveals (1) The in-plane and out-of-plane epitaxial relationships with sapphire. This is consistent with the prediction of geometrical superlattice area mismatching. (2) Monolayer MoS₂ and sapphire spacing of ~3 Å. This turns out to be the spacing between MoS₂ and the sulfur passivation layer formed on top of sapphire. This is supported by experimental TEM and AFM results as well as first principles density functional theory (DFT) calculations. (3) Despite the continuous monolayer coverage of MoS₂ on sapphire, the electron diffraction spots are unusually broader (~four times) than the instrument response width (~0.1 Å⁻¹). This is supported by numerical simulation of incommensurate finite size domains. This may be a generic result for transition metal dichalcogenide (TMDC) monolayer on mismatched substrate.

The HRLEED study of single crystal graphene on Cu(111) reveals that diffraction peaks have very similar full-width-at-half-maximums but the average broadening is significantly (~three times) larger than the instrument response (~0.03 Å⁻¹). This suggests a noticeable number of defects exist within both graphene and copper surface. From the LEED IV curve after an inner potential correction, the graphene to Cu(111) surface distance is estimated to be $d = 3.49 \pm 0.01$ Å. This value is close to that ($d = 3.27 \pm 0.07$ Å) determined by RHEED from multilayer graphene and the interlayer spacing of 3.36 Å in graphite. This suggests that the coupling between graphene and Cu metal is similar to a pure van der Waals interaction.

For graphene buffered van der Waals epitaxial tin mono-sulfide (SnS) thin film, the RHEED patterns show the (010) orientation near the surface of the SnS film grown on the single crystal graphene and a dominant (111) orientation near the surface of the SnS film grown on the polycrystalline graphene. Additional minor orientations near the surface were observed by RHEED that X-ray diffraction (XRD) is not able to detect.

1. INTRODUCTION

This thesis is divided into five chapters. In Chapter 1, I introduce the overall motivation, diffraction basics, brief experimental (growth methods and characterization techniques) and brief theoretical simulations (geometrical superlattice area mismatching and first principles density function theory) used for the study of 2D materials. The main experimental results of 2D materials are covered in Chapters 2, 3 and 4. The Chapter 5 has results of a layered thin film and a 3D thin film. Each Chapter starts with its own introduction, followed by sample preparation, specific diffraction methodology, experimental conditions, data collection, analysis, discussion, and conclusion. The last chapter lists future works worthy of pursuing.

Chapters 2 presents the results of the 2D reciprocal space maps obtained from ARHEED characterization of various graphene samples that include the commercially available polycrystalline graphene on SiO₂/Si substrate (graphene-supermarket.com)¹ and the epitaxial single crystalline graphene grown on Cu(111) substrate using chemical vapor deposition (CVD) as well as transferred single crystalline graphene onto the SiO₂/Si substrate². Chapter 3 presents 3D maps of TMDCs MoS₂ and WS₂ grown on sapphire using metal organic chemical vapor deposition (MOCVD) as well as their finite size domains extracted from a comparison of simulated diffraction spot broadening and experimentally measured diffraction spot broadening. Chapter 4 presents the HRLEED characterization of graphene on Cu(111).

1.1 Motivation

Two dimensional (2D) materials have been extensively studied in recent years because of their many novel and unusual electronic and optoelectronic properties^{3, 4}. Common 2D materials include graphene, hexagonal boron nitride, and layered metal chalcogenides (LMCs). When a 2D material is grown on a surface, it may form many different 2D textures including single crystal,

random polycrystalline, or a texture with a preferred in-plane orientation. The structure of a 2D material not only strongly affects the electronic, electrical, and optical properties of the material itself but also influences the epitaxial growth of other 2D materials when it is used as a template. Therefore, it is of foremost importance to know the structure of 2D materials before their applications. However, the structure of a layer or a few-layer thick material is challenging to study due to the followings: (1) The number of atoms in the 2D materials is significantly smaller than bulk materials. Conventionally researchers have been using X-ray diffraction (XRD) to measure the lattice constant and crystal structure of a bulk material. Application of XRD to 2D materials, however, suffers from low signal-to-noise ratio because of the weak interaction between X-ray and matters. (2) 2D materials themselves can hardly be free-standing. Usually they are grown on a substrate or transferred from the growth substrate onto another bulk substrate. This means that the effects from the substrate need to be excluded or clearly differentiated during the measurements. For example, 2D materials must be transferred onto metal grids before atomic resolution imaging by transmission electron microscopy (TEM), which might be a hassle if they've already formed a heterostructure in an integrated device. (3) 2D materials, synthesized through either bottom-up⁵⁻⁹ or top-down¹⁰⁻¹² methods, usually produce small grain sizes. As a consequence, the local (nanometer scale) properties may be different from the global (wafer scale) ones. Therefore, the wafer scale uniformity of the 2D materials must be examined in order to study other properties and scale up in industrial productions.

The current push for comprehensive and quantitative characterization of 2D materials as grown or transferred onto arbitrary substrates has triggered us to apply electron diffraction in such systems. This thesis mainly focuses on the use of reflection high-energy electron diffraction (RHEED) and high-resolution low-energy electron diffraction (HRLEED). With the high

resolving power in both RHEED and HRLEED, the issues mentioned above can be properly addressed. First, the Coulomb interaction between electrons and ion cores in electron diffraction is much stronger than the photon-electron interaction in XRD that results in four orders of magnitude stronger electron scattering intensity than that of photons, so the signal-to-noise ratio can be enhanced by orders of magnitudes. Second, since both RHEED and HRLEED are surface sensitive and non-destructive, the substrate effects are attenuated and there's no need to transfer 2D materials before its characterization. Finally, the spot size of RHEED electron beam is about 1 mm. Under a glancing incidence ($\sim 1^\circ$), the electron beam can span across the entire wafer of more than 1 cm. The rich quantitative information contained in the RHEED patterns from a wafer-scale 2D material sample is equivalent to more than 1 million real space scanning probe microscopy images such as atomic force microscopy (AFM) or scanning tunneling microscopy (STM). Therefore, RHEED provides the statistical quantitative information of unit cell and long-range order.

1.2 Diffraction Basics

Diffraction from a 2D lattice is similar to that from a bulk material except there exists no Laue condition in the direction perpendicular to the surface. Figure 1.1 shows a schematic of the diffraction from a 2D surface lattice with unit vectors \mathbf{a} and \mathbf{b} . The \mathbf{k}_{in} and \mathbf{k}_{out} are the incoming wavevector and outgoing wave vector, respectively. The momentum transfer $\mathbf{S} = \mathbf{k}_{out} - \mathbf{k}_{in}$ and the reciprocal space vector $\mathbf{G}(hk) = h\mathbf{a}_1^* + k\mathbf{a}_2^*$, where \mathbf{a}_1^* and \mathbf{a}_2^* are reciprocal space unit vectors. The two Laue conditions are:

$$\mathbf{S} \cdot \mathbf{a}_1 = 2\pi h, \quad \mathbf{S} \cdot \mathbf{a}_2 = 2\pi k. \quad (1.1)$$

For a 2D lattice with $N \times M$ number of scatters, the position vector \mathbf{R} of an atom is:

$$\mathbf{R} = n\mathbf{a}_1 + m\mathbf{a}_2. \quad (1.2)$$

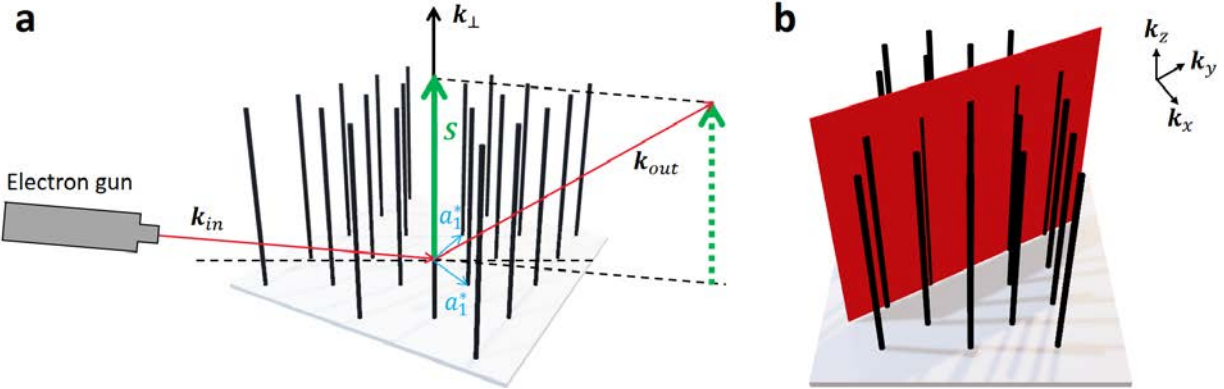


Figure 1.1: (a) Wave scattering parameters and conditions from a 2D lattice. (b) The plane-like Ewald sphere (red plane) cut of the reciprocal rods

The scattering amplitude is given by:

$$A(\mathbf{S}) = F(\mathbf{S}) \cdot \sum_{j=1}^{NM} \exp(i\mathbf{S} \cdot \mathbf{R}_j). \quad (1.3)$$

The structure factor $F(\mathbf{S})$ is:

$$F(\mathbf{S}) = \sum_m f_m e^{-i(\mathbf{S} \cdot \mathbf{r}_m)}, \quad (1.4)$$

where f_m is the atomic form factor of the m^{th} atom in the basis of a unit cell and \mathbf{r}_m is the position vector of the m^{th} atom in the basis of a unit cell.

The kinematic (single scattering) diffraction intensity is:

$$I(\mathbf{S}) = |A(\mathbf{S})|^2 = |F(\mathbf{S})|^2 \frac{\sin^2(N\mathbf{S} \cdot \mathbf{a}_1/2)\sin^2(M\mathbf{S} \cdot \mathbf{a}_2/2)}{\sin^2(\mathbf{S} \cdot \mathbf{a}_1/2)\sin^2(\mathbf{S} \cdot \mathbf{a}_2/2)}. \quad (1.5)$$

The center peak intensity is proportional to the square of the number of atoms:

$$I(\mathbf{S} = 0) \propto (NM)^2. \quad (1.6)$$

Therefore, it is much more difficult to observe diffraction from 2D materials in which fewer atoms are available to scatter the waves than from 3D materials.

In addition to the peak intensity one can estimate the full-width-at-half-maximum (FWHM) of a diffraction spot. Consider a one-dimensional profile in the x direction. For a sufficiently large number of scatters N , the intensity rises sharply when $\mathbf{S} \cdot \mathbf{a}$ approaches $2\pi h$. The FWHM of the peak can be estimated by varying the value of $\mathbf{S} \cdot \mathbf{a}$ away from its maximum by an ε ¹³,

$$\mathbf{S} \cdot \mathbf{a} = 2\pi h + \varepsilon, \quad (1.7)$$

where ε is the smallest non-zero number, which gives $\sin\left(\frac{N\varepsilon}{2}\right) = 0$. Then one obtains:

$$\varepsilon = 2\pi/N. \quad (1.8)$$

This means the width ε is inversely proportional to the number of scatters, N , which plays an important role in the interpretation of the broadening in RHEED and HRLEED spot analysis.

1.3 Experimental Methods

1.3.1 Synthesis

1.3.1.1 Chemical Vapor Deposition (CVD) Growth of Epitaxial Graphene

The thermal annealing of the as-deposited Cu(111) films on both sapphire and spinel by DC sputtering and the graphene growth were conducted at low-pressure CVD furnace (MTI Corporation OTF-1200x). The furnace was designed with a 6" × 56" quartz tube and three temperature zones. The Cu film substrates were placed in a ceramic boat and covered with a sheet of 25 μm polycrystalline Cu foil (99.98% in purity, Sigma Aldrich) with small openings, in order to reduce the Cu sublimation at high temperature and control the gas diffusion rate on the sample surface^{14, 15}. The CVD system was pumped down to ~50 mTorr and purged with high purity Ar gas. This flushing procedure was repeated three times. Then the system pressure was slowly increased to 50 ± 5 Torr by adjusting the pressure valve during temperature ramping up. In the meantime, 200 sccm Ar and 35 sccm H₂ were kept feeding through the tube. After ~40 min, the temperature ramped up to the anneal temperature of 1020 °C. The annealing time was 15 min.

After thermal annealing, the graphene growth was activated at 1020 °C by introducing methane (CH₄, 10 sccm) into the furnace. In a typical run, the graphene growth time was 30 min. After the growth, the CH₄ gas feed was immediately turned off. The furnace lid was opened to allow a rapid cooling. Meanwhile the Ar and H₂ gases kept flowing till the furnace reached room temperature.

1.3.1.2 Graphene Transfer

The graphene transfer followed the standard polymethyl methacrylate (PMMA, MicroChem 950 A4)-mediated method ^{16, 17}. In brief, the graphene surface was spin-coated five times with PMMA (spun at 1500 rpm for 60 s and baked at 120 °C for 10 min in between each spin coating), then immersed in the ammonium persulfate solution (3.0 g in 50 mL deionized water) for 24 - 48 hours to dissolve the Cu. Note the Cu film was sandwiched in between sapphire/spinel and PMMA. As a result, the etching was diffusion-limited and took longer than those using Cu foils as substrates. Once released from Cu, the PMMA-graphene stack was rinsed several times in deionized water, and then scooped out using a pre-cleaned silicon wafer with 50 nm thermal oxide. The PMMA-graphene-substrate stack was dried in air and baked at 150 °C for 15 min, followed by dissolving the PMMA protection film in acetone. Finally, the graphene film was rinsed with isopropanol and dried with nitrogen gas.

1.3.1.3 Metal Organic Vapor Deposition (MOCVD) Growth of MoS₂

Monolayer MoS₂ was deposited on epi-ready 2-inch c-sapphire substrate by gas source chemical vapor. Uniform monolayer deposition was achieved in a cold wall horizontal reactor equipped with wafer rotation. The sapphire substrate was heated on an inductively heated graphite susceptor. Molybdenum hexacarbonyl (Mo(CO)₆) and hydrogen sulfide (H₂S) were used for the growth. Mo(CO)₆ was maintained in a stainless steel bubbler at 10 °C and 950 Torr to achieve the required vapor pressure. H₂ carrier gas was passed through the bubbler at a flow rate of 10 sccm

which was used to deliver a Mo(CO)₆ flow rate of 3.6×10^{-2} sccm into the reaction chamber. 400 sccm of H₂S was used for the process. MoS₂ deposition was carried out at 1000 °C and 50 Torr in H₂ ambient. The substrate was first heated to 1000 °C in H₂ and maintained for 10 min before introducing the precursors for 18 min to achieve monolayer growth. The reactor was then cooled down in H₂S till 300 °C to inhibit decomposition of the MoS₂ films. At 150 °C the system was pumped down and purged with N₂ to remove any toxic gases before unloading the wafer.

1.3.1.4 Thermal Evaporation Deposition of SnS

According to the vapor phase diagram, the SnS evaporates congruently during deposition by thermal evaporation ¹⁸. This makes thermal evaporation a desirable method to grow SnS thin film. The advantage of using thermal evaporation of SnS is that thermal evaporation introduces negligible disorder in the single layer graphene as compared with other deposition techniques such as sputtering, e-beam, and pulsed laser depositions as shown by Raman spectra ¹⁹. The SnS film was grown on graphene/SiO₂/Si(100) substrate by evaporating SnS powder (Sigma Aldrich, purity $\geq 99.99\%$) placed in an alumina coated tungsten basket with the top opening diameter of about 1 cm (R.D. Mathis). The substrate was mounted about 15 cm above the SnS source. The base pressure of the vacuum chamber was $5 - 7 \times 10^{-7}$ Torr. Before a deposition, the substrate was heated to 280 °C from the backside with a ramping rate of 20 °C/min using a double ended halogen lamp (Ushio, FCL, J120V-500W) with a rectangular reflector (8 cm × 12 cm) installed inside the vacuum chamber. A schematic of the experimental setup of the thermal evaporator is shown in Fig. 1.2(a). During the deposition, the temperature of the substrate surface was maintained at 283 – 286 °C, which was monitored using a type K thermocouple (Nickel-Chromium/Nickel-Alumel) attached to the substrate surface. The deposition rate was about 0.6 – 0.8 Å/sec according to a quartz crystal monitor (QCM) with a gold coated quartz monitor crystal (Inficon, 008-010-G10).

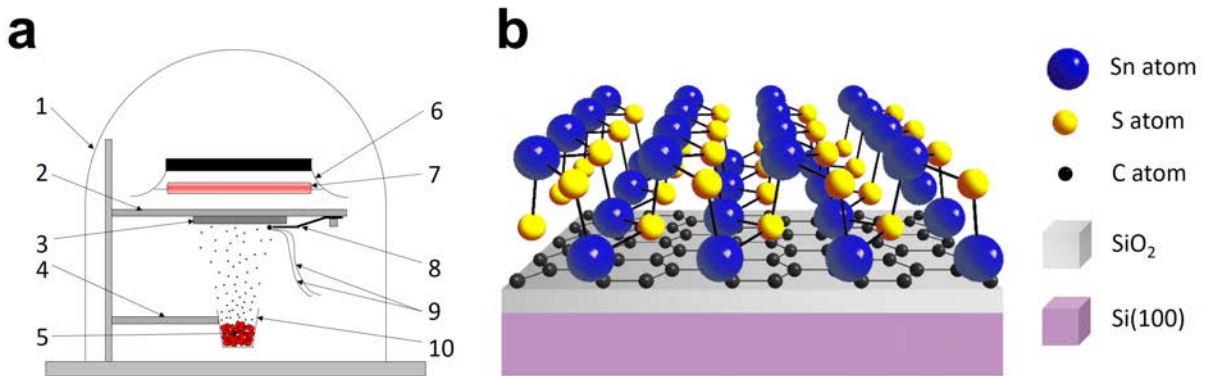


Figure 1.2: (a) A schematic of the thermal evaporator setup. Major components are labeled by numbers. 1. Glass chamber wall, 2. Substrate holder, 3. Substrate, 4. Source boat holder, 5. SnS powder source, 6. Light reflector, 7. Halogen lamp, 8. Substrate clamp, 9. Thermocouple wires, 10. Alumina coated tungsten basket. (b) A schematic of SnS layer on graphene/SiO₂/Si(100) substrate.

After the deposition, the lamp was turned off immediately. The substrate and the deposited SnS film were cooled down naturally. Both SnS films of about 500 nm thickness were deposited simultaneously on the polycrystalline and single crystal graphene substrates using this system. Fig. 1.2(b) shows a schematic of the layered structure of the SnS on graphene/SiO₂/Si(100) sample.

1.3.1.5 Vapor Transport Deposition (VTD) Growth of CdTe

CdTe thin films were deposited on mica substrates (SPI Grade V-4) by vapor transport deposition (VTD) method in a horizontal vacuum quartz tube furnace (Lindberg 59744-A) with three heating zones. The 2nd heating zone was located at the middle of the furnace. CdTe powders (Sigma Aldrich, purity $\geq 99.98\%$) of 0.2 g was weighed and separated into two halves. Each half of powders was spread evenly in an alumina boat ($0.5'' \times 3.5''$) before positioned at the center of the 2nd heating zone. Mica substrate was placed on a customized graphite ingot support shaped with a $\sim 35^\circ$ inclination angle, which is part 9 in the schematic drawing in Fig. 1.3. The purpose of designing this $\sim 35^\circ$ inclination is to achieve the best temperature uniformity since there's both vertical and horizontal temperature gradient inside the quartz tube. This graphite support was positioned at ~ 15.5 cm downstream away from the center of the 2nd heating zone. The quartz tube

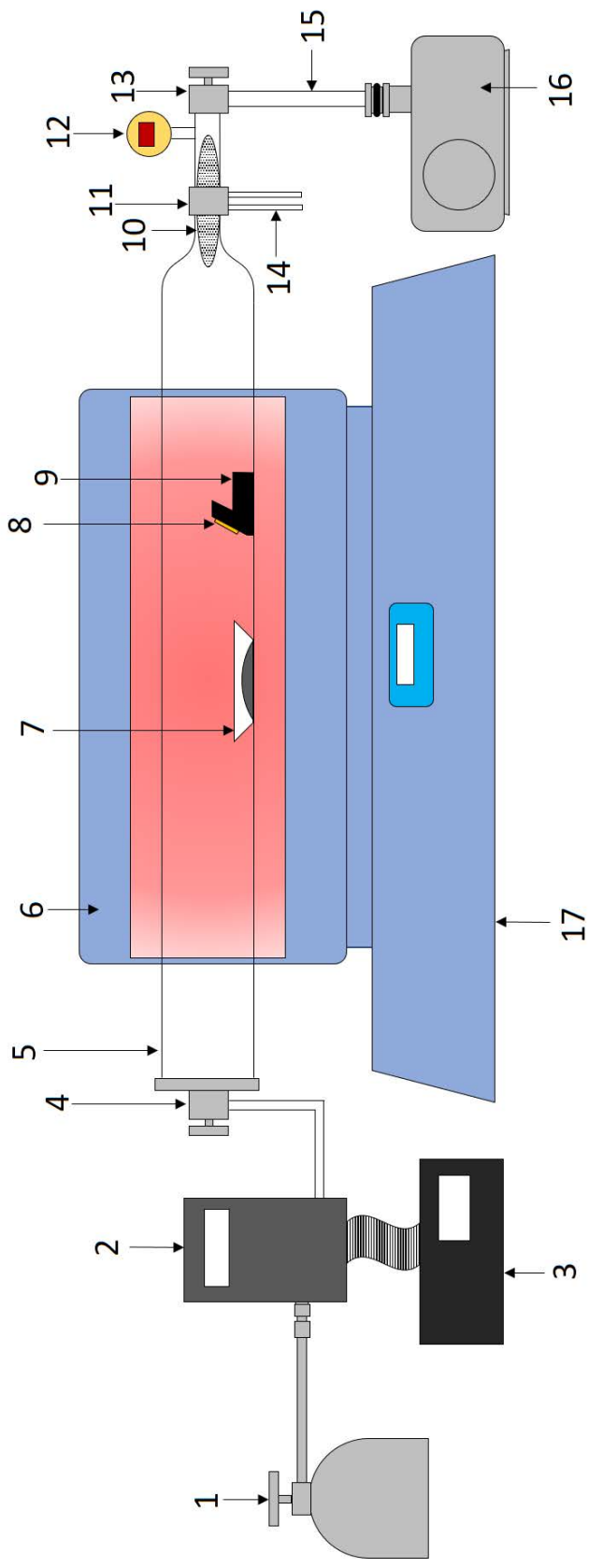


Figure 1.3: A schematic of the VTD setup: 1. Ar gas cylinder, 2. Mass flow controller, 3. Multi-channel controller, 4. Valve, 5. Quartz tube (OD = 5.5 cm), 6. Three-zone furnace, 7. Alumina boat containing the CdTe source powders, 8. Mica substrate, 9. Graphite support, 10. Lint free cleanroom wipe, 11. Cooling water case, 12. Digital pressure gauge, 13. Valve, 14. Cooling water tube, 15. Flex tube, 16. Mechanical pump, 17. Furnace temperature and ramping rate controller. The thermocouples are embedded inside the furnace.

was then sealed and evacuated to \sim 5 mTorr during the growth. The temperature at the CdTe source powders is 600 ± 10 °C, while the temperature at the mica substrate was 370 ± 10 °C. The temperature at the CdTe source powder was read from a thermocouple that is integrated in the furnace. The temperature at downstream had been calibrated as a function of the distance away from the center with an external thermocouple. The ramp-up time from room temperature was 40 minutes and the growth lasted 10 minutes. After the furnace naturally cooled down to \sim 160 °C, the substrate with CdTe deposition was then taken out. A schematic of the VTD setup is shown in Fig. 1.3.

1.3.1.6 Exfoliation of CdTe Film From Mica

One of the merits of a 2D material is the 2D material can be easily exfoliated from its bulk form or the growth substrate due to the weak van der Waals bonding at the interface^{20, 21}. The CdTe thin film has been successfully exfoliated from the mica substrate using a combination of the capillary force from water and the adhesive force exerted by the epoxy. A typical vapor transport deposited CdTe film on mica substrate has a rough surface that is not suitable for RHEED or HRLEED studies. However, due to the very smooth surface of mica, if the CdTe film grown on it can be exfoliated off, the exposed CdTe surface at the interface would stay smooth, making it more suitable to be characterized by RHEED or HRLEED. In addition, the CdTe film must be supported by a rigid substrate like a piece of silicon wafer, with the smooth CdTe-mica interface facing up for electron diffraction after the exfoliation. In addition, a conductive epoxy was used to avoid charging during the RHEED or HRLEED measurements.

A schematic showing the process of CdTe exfoliation from a mica substrate and supported on a Si substrate is in Fig. 1.4. The exfoliation process starts with the as-grown CdTe film on a mica sample. Two parts of conductive epoxy (H-22 EPO-TEK, Ted Pella with low outgassing rate)

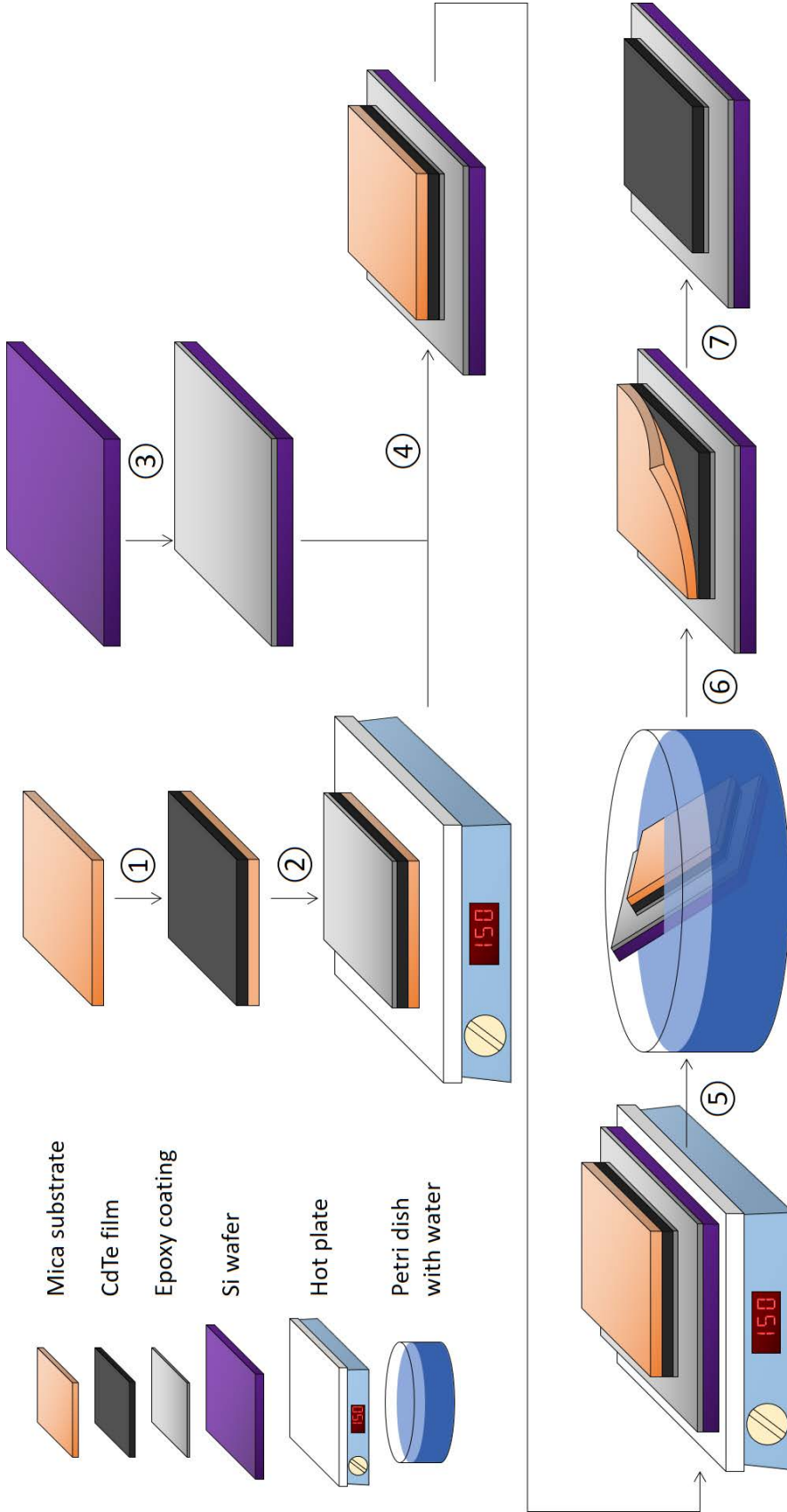


Figure 1.4: A schematic showing the process of CdTe exfoliation from a mica substrate: 1. Vapor transport deposition growth of CdTe film on a mica substrate, 2. Spin coating a thin layer of epoxy on the CdTe film with 5000 RPM for 1 minute, then cure the epoxy on a hot plate at 150 °C for 8 minutes, 3. Spin coating a thin layer of epoxy on the Si wafer with 5000 RPM for 1 minute, 4. Flip the spin coated CdTe/mica sample and attach it to the spin coated Si wafer. Apply a gentle force to make sure they make a good contact, 5. Cure the layer of epoxy on Si on a hot plate at 150 °C for 8 minutes, then cut away the edge parts of the mica substrate, 6. Slowly put the whole sample with an inclined angle into a Petri dish filled with water. Try it several times until mica starts to detach from the CdTe film at the edge, 7. Peel off the mica substrate to reveal the flat CdTe surface.

were mixed with a 100:4.5 mass ratio and then spin coated onto the CdTe surface with 5000 revolutions per minute (RPM) for 1 minute. The epoxy took ~8 minutes to cure at 150 °C on a hotplate. Before that, a thin layer of epoxy was coated on a silicon wafer. After the epoxy was cured, the epoxy coated CdTe/mica sample was flipped 180° and attached to the epoxy coated silicon wafer, letting the cured epoxy on CdTe make a seamless contact with the uncured epoxy on the silicon wafer. The whole sample was then put on the hotplate for ~8 minutes again at 150 °C to cure the second layer of epoxy on the silicon. Then the next step was to cut away the edge parts of the mica substrate to make the interface between epoxy and the CdTe film accessible to the water. After that, the sample was held with a tweezer and slowly put into the water with an inclination angle of about 45°. During this process, the CdTe layer was separated from the substrate by the capillary force from water and could be easily peeled off.

1.3.2 Characterization

1.3.2.1 Atomic Force Microscopy (AFM)

AFM is an excellent tool for microscopic topography studies of various surfaces. It uses a cantilever with a sharp tip. As the tip is brought close to the surface, it experiences an attractive or repulsive interaction, depending on the distance between the tip and the surface. This force causes the cantilever to deflect towards or away from the surface, which is detected by recording the position of a laser beam reflected off the cantilever on a position-sensitive photo diode. When the repulsive force dominates, the AFM works in the so-called contact mode, while in the non-contact mode the attractive force dominates. Figure 1.5(a) depicts the relationship between the interatomic force and the tip to surface distance in a typical AFM.

In the contact mode AFM, the force between the tip and the sample is held constant. This is realized by moving the Z-scanner up and down through a feedback control circuit which takes

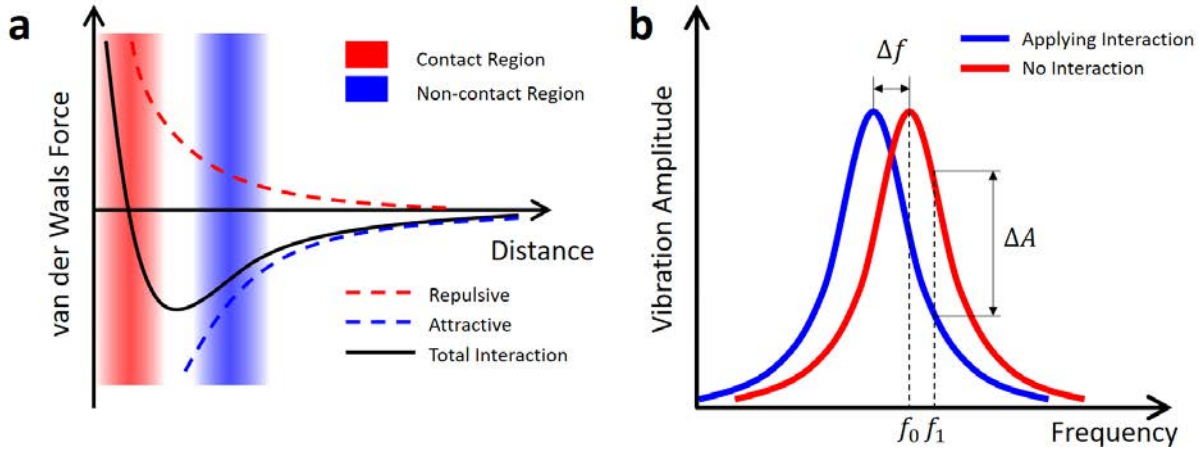


Figure 1.5: (a) van der Waals interaction force vs. tip-surface distance for a typical AFM. (b) Vibration amplitude vs. drive frequency with and without a tip-surface interaction.

the deflection of the cantilever as an input. Therefore, the surface topography is generated from the Z-scanner's motion. In the non-contact mode, the cantilever is mechanically vibrated by a bimorph. The cantilever's intrinsic resonant frequency f_0 can be measured by the bimorph's drive frequency that corresponds to the maximum vibration amplitude of the cantilever. During AFM measurements, however, the resonant frequency will shift to a lower value f_{eff} because of the attractive force between the cantilever and the sample surface. The vibration amplitude measured at a drive frequency (f_1) slightly larger than f_0 will therefore be reduced by ΔA (change of amplitude), which reflects the distance (d) between the cantilever and the sample surface. The surface topography is then generated from the Z-scanner's motion that keeps d constant using a feedback mechanism taking ΔA as an input. Figure 1.5(b) shows the vibration amplitude vs. drive frequency with and without a tip-surface interaction.

The AFM used in this thesis is a Park Systems XE100 model. The AFM tip (μ mash, HQ: CSC17/AlBS) used for contact mode had a tip radius of 8 nm, a force constant of 0.18 N/m, and a resonant frequency of 13 kHz. The tip (μ mash, NSC16/F/Al BS) for non-contact mode had a tip radius less than 10 nm, a force constant of 41.5 N/m, and a resonant frequency of 170 kHz.

1.3.2.2 Reflection High-Energy Electron Diffraction (RHEED) and Azimuthal RHEED

RHEED is a technique that characterizes the surface of crystalline materials using diffraction of high-energy electrons. It was first performed by Nishikawa and Kikuchi in 1928²². Typically, the electrons are accelerated to 10 to 30 keV and then hit the surface of the sample with a glancing incident angle. The mean-free-path of such electrons is ~10 to 20 nm. With a 1~2 degrees incident angle, the penetration depth is less than 1 nm. This makes RHEED an very surface-sensitive technique. Figure 1.6(a) shows the setup of the RHEED system used in this thesis work. RHEED is usually a standard component in molecular beam epitaxy (MBE) systems to monitor the growth rate by measuring the intensity oscillation^{23, 24}. Apart from that, RHEED is also a very powerful tool to study surface structures^{25, 26}. From an individual RHEED pattern we can obtain not only the lattice constants but also its crystal symmetry. A complete surface texture characterization can be done using RHEED pole figure²⁷⁻²⁹ for bulk materials and azimuthal RHEED (ARHEED)^{1, 2} for 2D materials. ARHEED enables sample rotation during measurement using a stepping motor. A schematic of the sample holder is shown in Fig. 1.6 (b). In order to probe the entire upper half of the reciprocal space during the construction of pole figure or 2D reciprocal space map, the sample was rotated azimuthally with a 1.8° step size from 0° to 180° in 100 steps and the corresponding RHEED pattern was recorded at each incremental step by the digital camera facing the phosphor screen outside the RHEED chamber.

1.3.2.3 High-Resolution Low-Energy Electron Diffraction (HRLEED)

Low-energy electron diffraction (LEED) was discovered by Davisson and Germer in 1927³⁰ and further developed by others in 1930s³¹ and has become a popular technique in Surface Science. Electrons with energies in the range of 50 to 300 eV are used in LEED, which makes it extremely surface-sensitive. It has been used to determine many surface properties including

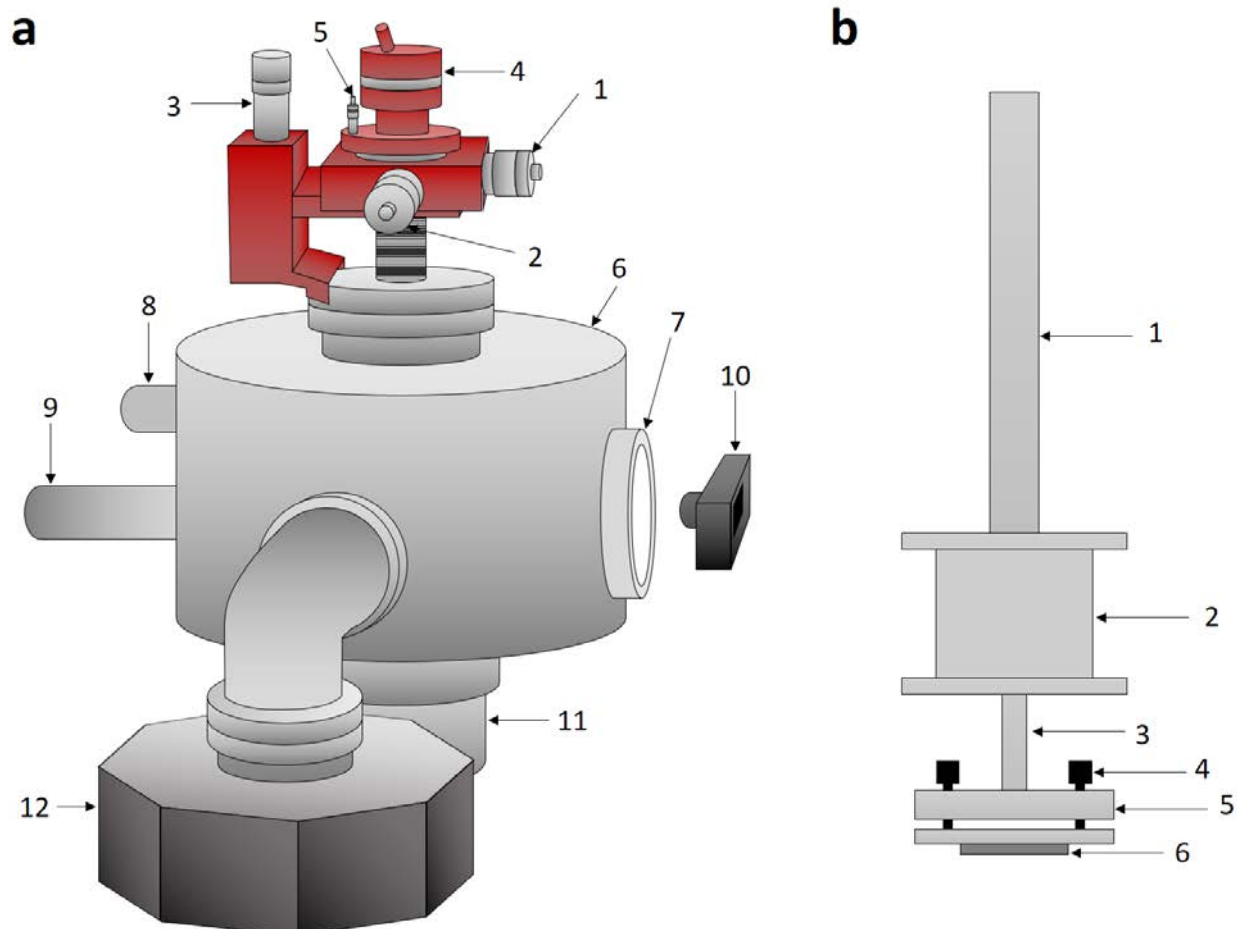


Figure 1.6: (a) Schematic of the RHEED system: 1. X-axis micrometer, 2. Y-axis micrometer, 3. Z-axis micrometer, 4. Azimuthal rotation manipulator, 5. Tilt micrometer, 6. Vacuum chamber, 7. Phosphor scree, 8. Stainless steel vacuum hose to the turbo pump, 9. Electron gun, 10. Digital camera, 11. X-ray photoelectron spectroscopy (XPS) cylindrical mirror analyzer, 12. Ion pump. (b) Schematic of the sample holder for the RHEED system: 1. Central shaft, 2. Stepping motor, 3. Stepping motor shaft, 4. Sample tilt-adjust screws, 5. Sample tilt-adjust stage, 6. Sample.

crystalline quality, size of unit cells, and type of reconstruction^{32,33} and has achieved great success.

Figure 1.7(a) shows the electron optics of a typical LEED system. High-resolution LEED (HRLEED) developed by Professor Henzler's group in Germany is a variation of the conventional LEED technique. The HRLEED has 10 times higher resolution than a conventional LEED diffractometer. The HRLEED consists of a single crystal tungsten tip, a fine focus electron gun, an electrostatic deflection unit (octupoles) and a high gain channeltron electron detector³⁴. HRLEED allows analysis of the surface morphology through the intensity profile of the diffraction

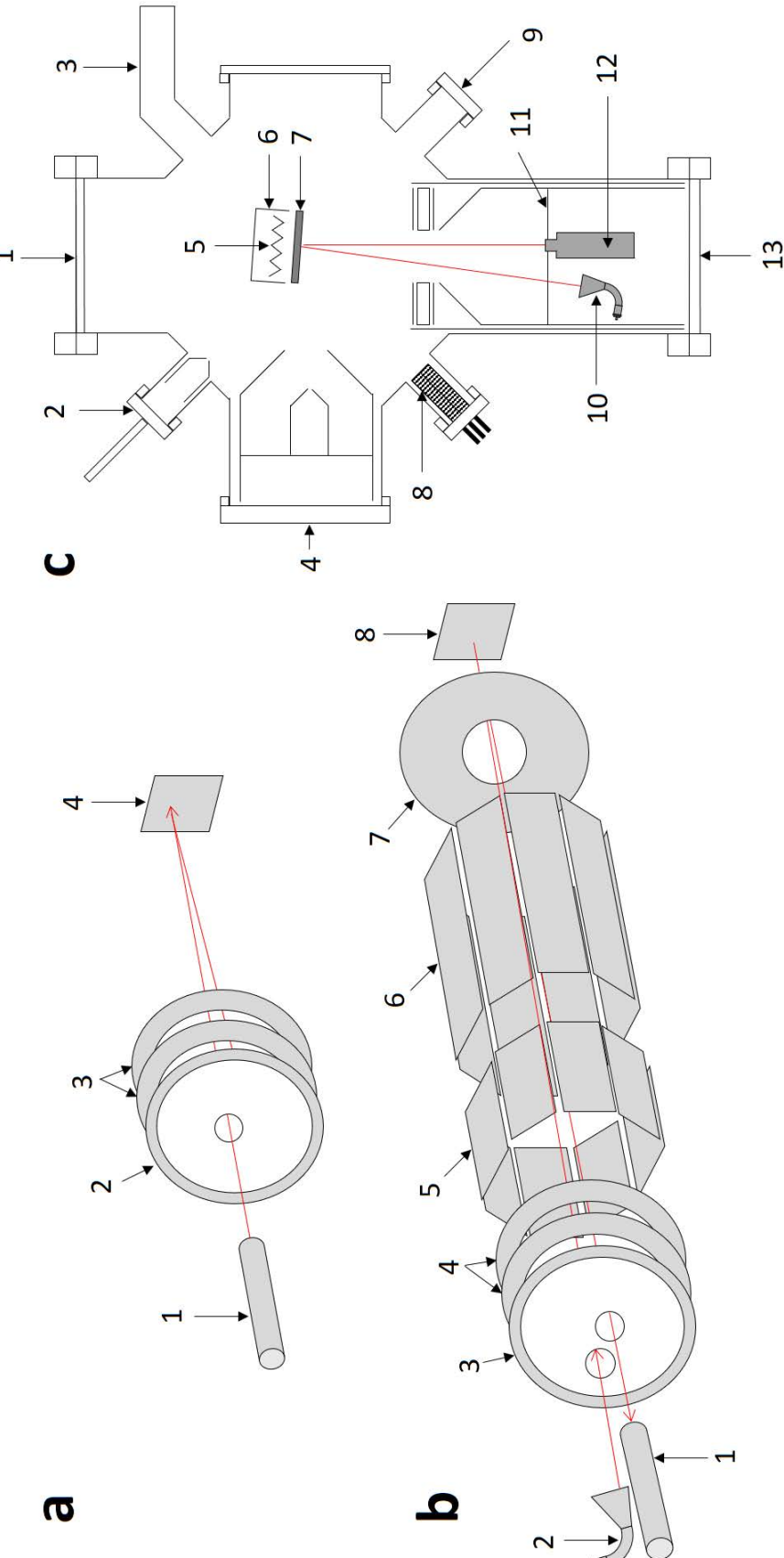


Figure 1.7: (a) A schematic of a conventional LEED optics: 1. Electron gun, 2. Sample. (b) A schematic of the HRLEED optics: 1. Ion gun, 2. Sample, 3. Tungsten filament, 4. Screen grids, 5. Screen octupole, 6. Crystal octupole, 7. Crystal lens, 8. Phosphor screen. (c) A schematic of the HRLLEED vacuum chamber layout: 1. View port, 2. Ion gun, 3. Screen grids, 4. Phosphor screen, 5. Screen octupole, 6. Sample, 7. Crystal lens, 8. Phosphor screen, 9. View port, 10. Cylindrical mirror analyzer (CMA) for Auger electron spectroscopy (AES), 11. Sample holder housing, 12. Phosphor screen, 13. View port.

spots. Lattice parameters or size of unit cell can be determined with an accuracy of up to 0.02 Å. Due to the high coherence of the electron beam, morphological features up to 2000 Å in size (transfer width) could be detected³⁵. Figure 1.7(b) shows a schematic of the HRLEED electron optics and Fig. 1.7(c) shows the layout of the HRLEED vacuum chamber that was used in this thesis work.

1.3.2.4 *X-ray Diffraction (XRD)*

XRD has been a renowned technique to determine the crystal structures since its invention by Max von Laue in 1912³⁶. Researchers typically use $\theta/2\theta$ (θ is the incident angle) scans to determine the structure and lattice constant, azimuthal φ scans to determine the crystal in-plane orientation dispersion, rocking curves to characterize the out-of-plane orientation dispersion, and pole figures to determine the texture of the sample. All XRD in this thesis were carried out using a Bruker D8 Discover diffractometer at the Center for Biotechnology and Interdisciplinary Studies at RPI. The Cu K α X-ray source used had a wavelength of 1.5405 Å. A point detector with a 0.01° scanning step size and a 0.1 sec counting time at each step was used to collect the X-ray diffraction theta-2theta ($\theta-2\theta$) scans. The scanning step size for the rocking curve was 0.002°. The incident beam, detector, and anti-scatter slits used all had a 0.6 mm width. XRD pole figure measurements were carried out using the same X-ray diffractometer with a 1° step size in both azimuthal angle (φ) and sample tilt angle (χ).

1.3.2.5 *Transmission Electron Microscopy (TEM)*

TEM has been utilized to study the interface between the monolayer MoS₂ and the sapphire substrate. The TEM samples were prepared by collaborator at Penn State University using a focused ion beam (FIB) technique in FEI SEM Helios Nanolab 660. The HRTEM imaging condition for the cross section of MoS₂/sapphire interfaces was tuned to a negative Cs to provide white atom contrast at a slightly over focusing. Aberration-corrected scanning TEM (STEM)

imaging and electron dispersive spectroscopy EDS (using a SuperX EDS detector) were performed by FEI Titan G2 60-300 microscope, operating at 80 kV with a double spherical aberration correction, offering a sub-angstrom imaging resolution. A high-angle annular dark field (HAADF) detector was used for the ADF-STEM imaging with a collection angle of 51-300 mrad, a beam current of 45 pA, and a beam convergence angle of 30 mrad (C2 aperture of 70 μ m) for STEM image acquisition.

1.3.2.6 Other Characterization Techniques

Additional *ex situ* techniques used for surface morphology, crystal texture structure, chemical composition and vibrational modes characterization are briefly described below.

The scanning electron microscopy (SEM) images were obtained using the ZEISS SUPRA 55 model. The electron backscatter diffraction (EBSD) characterizations for near surface texture were carried out with a Karl Zeiss Ultra 1540 EsB SEM-FIB system integrated with a NordlysNano EBSD Detector (Oxford Instruments). A 15 kV electron beam was used to scan the sample surface with an area of 5.0 μ m \times 5.0 μ m, a working distance of 18 mm, and a sample tilting angle of 70°. The scanning step size was set at 125 nm. The crystallographic orientation data was collected using the Aztec 2.1 EBSD data acquisition software and post-analyzed using the HKL Channel 5 Mambo software (Oxford Instruments) for the crystallographic orientation mapping, the grain boundary misorientation estimation, and the pole figure plotting. An Auger electron spectroscopy (AES) for surface chemical composition has been integrated in the HRLEED chamber. A cylindrical mirror analyzer (CMA) was used to detect the Auger electrons. Incident electrons were accelerated to 2 kV with 2 mA emission current. The energy step size was 0.5 eV and the time per step was 100 ms. Raman spectra for vibrational modes were collected using a Renishaw 2000A Raman microscope system. The laser wavelength and power used were 785 nm and 2 mW, respectively.

The integration time was 10 s and the laser spot size was $5 \mu\text{m} \times 20 \mu\text{m}$. The step size used in the Raman scattering data collection was 1 cm^{-1} .

1.4 Calculation and Simulation

Some experimental data were analyzed by geometrical superlattice area mismatching modeling and first principles density functional calculations are briefed below.

1.4.1 Geometrical Superlattice Area Mismatching (GSAM)

The GSAM simulation^{37, 38} has been used to investigate all possible orientational alignments between LMC and c-sapphire. In the simulation, generally, one defines u_1 and v_1 (u_2 and v_2) as the LMC overlayer (c-sapphire substrate) superlattice vectors separated by angle, α_1 (α_2). All superlattices possibly formed between LMC and c-sapphire are calculated by adjusting the rotation angle (ϕ_R) from 0° to 360° , where ϕ_R is defined as the angle between LMC [11̄20] and c-sapphire [11̄20] directions. Two criteria are used in the calculation to determine the relative likelihood of observing a superlattice at a given ϕ_R : (1) the superlattice area of LMC, A_1 (the superlattice area of c-sapphire, A_2) should be small to increase the density of coincident lattice sites; (2) the mismatch between two superlattices areas A_1 and A_2 , denoted as ΔA , should be small to minimize the heteroepitaxial system's interfacial strain energy. The ΔA is defined as $\Delta A = A(\Delta u/u + \Delta v/v + \Delta \alpha/\tan \alpha)$, where $\Delta u = |u_1 - u_2|$, $\Delta v = |v_1 - v_2|$ and $\Delta \alpha = |\alpha_1 - \alpha_2|$ are the differences in superlattice parameters between the LMC and c-sapphire, and $A \approx A_1$ (or A_2), $u \approx u_1$ (or u_2), $v \approx v_1$ (or v_2), $\alpha \approx \alpha_1$ (or α_2). Following limits are set to exclude those improbable rotation angles for forming superlattices: $\Delta u/u < 5\%$, $\Delta v/v < 5\%$, and $\Delta \alpha/\alpha < 5\%$, and A_1 (A_2) $< 200 \text{ \AA}^2$. Based on these criteria mentioned above, the rotation angle ϕ_R associated with the smallest values of A_1 (A_2) and ΔA represents the most favorable condition for a superlattice to form at the interface.

1.4.2 Density Functional Theory (DFT) Calculations

The DFT calculations were carried out with the Vienna *ab initio* Simulation Package (VASP)³⁹. The core electrons were described by the projector-augmented-wave (PAW) method⁴⁰ and the electron exchange and correlation were modeled within the generalized gradient approximation (GGA) using the Perdew-Burke-Ernzerhof (PBE) form⁴¹. The non-local optB86b-vdW exchange-correlation functional was used to describe the dispersion interaction (vdW forces)^{42, 43}. The plane wave basis kinetic energy cut off was set to 400 eV. For the construction of a supercell in DFT calculations, the experimental and GSAM simulated results were used as references.

2. ARHEED CHARACTERIZATION OF GRAPHENE

2.1 Introduction

2.1.1 Motivation

Owing to its remarkable physical properties, such as high carrier mobility, high thermal conductivity and electrical conductivity, and high optical transparency, graphene has attracted worldwide attentions since Geim and Novoselov made the big splashing discovery in 2004²⁰. Since then, great efforts have been devoted to fabricate high quality graphene which has characteristics of single crystallinity, monolayer, and scalability⁴⁴⁻⁵¹. Among these qualities, single crystallinity is of foremost importance. Bilayer and few-layer graphene, if grown in a controlled manner, might have special interests as some researchers have purposely pursued them⁵²⁻⁵⁵. Polycrystalline graphene has often been considered undesirable for electronics because the grain boundaries would undermine those expected extraordinary properties obtained from single crystal graphene.

Reflection high-energy diffraction (RHEED)⁵⁶ has been chosen to study the symmetry and perfection of graphene in this thesis, because the charging issue is more forgivable in RHEED compared to low-energy electron diffraction (LEED). In RHEED, energy ranging from several keV to tens of keV is used. Depending on the substrate used, the charging effect on the integrity of the diffraction pattern can be reduced substantially. A good common example is graphene on

Portions of this chapter previously appeared as: Xiang, Y.; Guo, F.-W.; Lu, T.-M.; Wang, G.-C., Reflection high-energy electron diffraction measurements of reciprocal space structure of 2D materials. *Nanotechnology* **2016**, *27* (48), 485703.

Portions of this chapter previously appeared as: Lu, Z.; Sun, X.; Xiang, Y.; Washington, M. A.; Wang, G.-C.; Lu, T.-M., Revealing the Crystalline Integrity of Wafer-Scale Graphene on SiO₂/Si: An Azimuthal RHEED Approach. *ACS Appl. Mater. & Interfaces* **2017**, *9* (27), 23081-23091.

an oxide layer on a Si substrate. If the oxide layer thickness is on the order of tens of nm to hundreds of nm, RHEED can give an excellent diffraction pattern while LEED may not. However, in a conventional RHEED configuration, the electrons are incident at a glancing angle with respect to the surface and the diffraction pattern only provides limited information on the reciprocal lattice structure. RHEED pole figure technique²⁷⁻²⁹ was a newly developed method for near surface texture characterization of 3D thin films or nanostructures using the transmission mode. This technique is used to measure the 3D crystal orientation distribution near the surface but not applicable to 2D materials. For 2D materials, RHEED patterns are collected using reflection mode from the monolayer. It is possible to obtain the entire reciprocal space structure of graphene by rotating the sample around the surface normal and measuring the RHEED patterns as a function of the azimuthal angle. Azimuthal RHEED have been employed to map the reciprocal space structure of a sample⁵⁷⁻⁵⁹ to study surfaces and thin film in the past. In this chapter, I will present the results of using this method to construct the reciprocal space structure of a graphene on SiO₂/Si. All 2D structures with limited long-range order produce “streaks” in a RHEED pattern. A 2D reciprocal space structure is constructed by measuring the characteristics of streaks as a function of momentum transfer parallel to the surface while varying the azimuthal angle.

2.1.2 Background of RHEED 2D Texture Analysis

First, we consider a single crystal 2D material. The 3D reciprocal space structure of a single crystal 2D material consists of vertical “rods”⁵⁶. Figure 2.1(a) shows a schematic of the 3D reciprocal space structure of a 2D hexagonal lattice. We label the momentum transfer $\mathbf{k} = \mathbf{k}_o - \mathbf{k}_i$, where \mathbf{k}_i and \mathbf{k}_o are the incident and outgoing wave vectors, respectively. The \mathbf{k} in the x , y , and z directions are denoted as k_x , k_y , and k_z , respectively. The diffraction intensity along the k_z direction is uniform and featureless. In RHEED, the wave vector of electrons is large for an incident beam

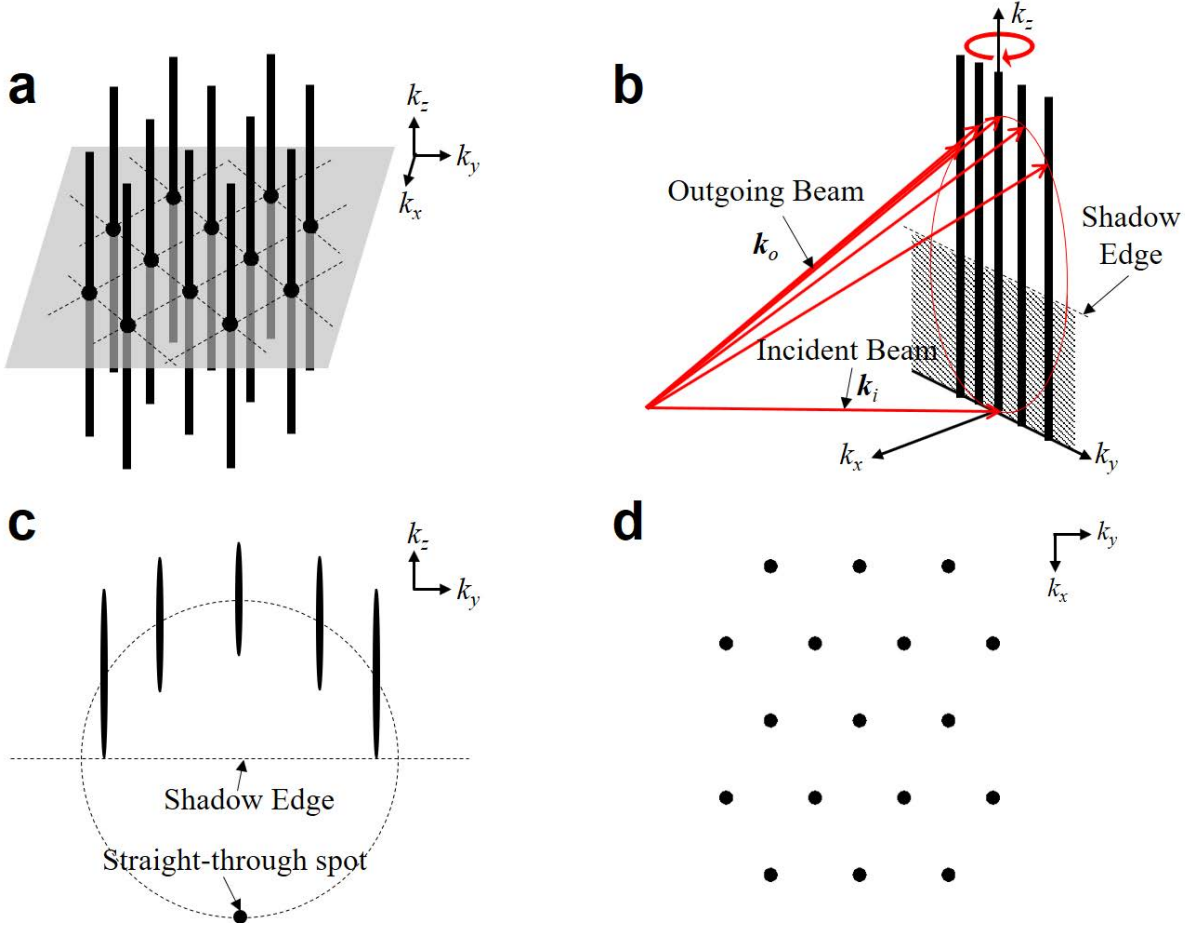


Figure 2.1: (a) A schematic of the reciprocal space structure of a 2D hexagonal lattice, (b) a schematic showing how the Ewald sphere cuts through the reciprocal rods. The curly red arrow represents the rotation around the sample normal direction at various azimuthal angle φ , (c) a simulated RHEED pattern, and (d) a schematic of the 2D reciprocal space structure of a 2D hexagonal lattice looking into the negative k_z direction.

energy ranging from several keV to tens of keV and the Ewald sphere cuts through the rods as shown in Fig. 2.1(b). Streaks would form in the RHEED diffraction pattern as shown in Fig. 2.1(c), when looking into the $-k_x$ direction. The 2D reciprocal space structure can be obtained by looking into the $-k_z$ direction as shown in Fig. 2.1(d). Experimentally, this can be constructed by plotting the RHEED streak intensity as a function of the momentum transfer parallel to the surface while varying the in-plane azimuthal angle.

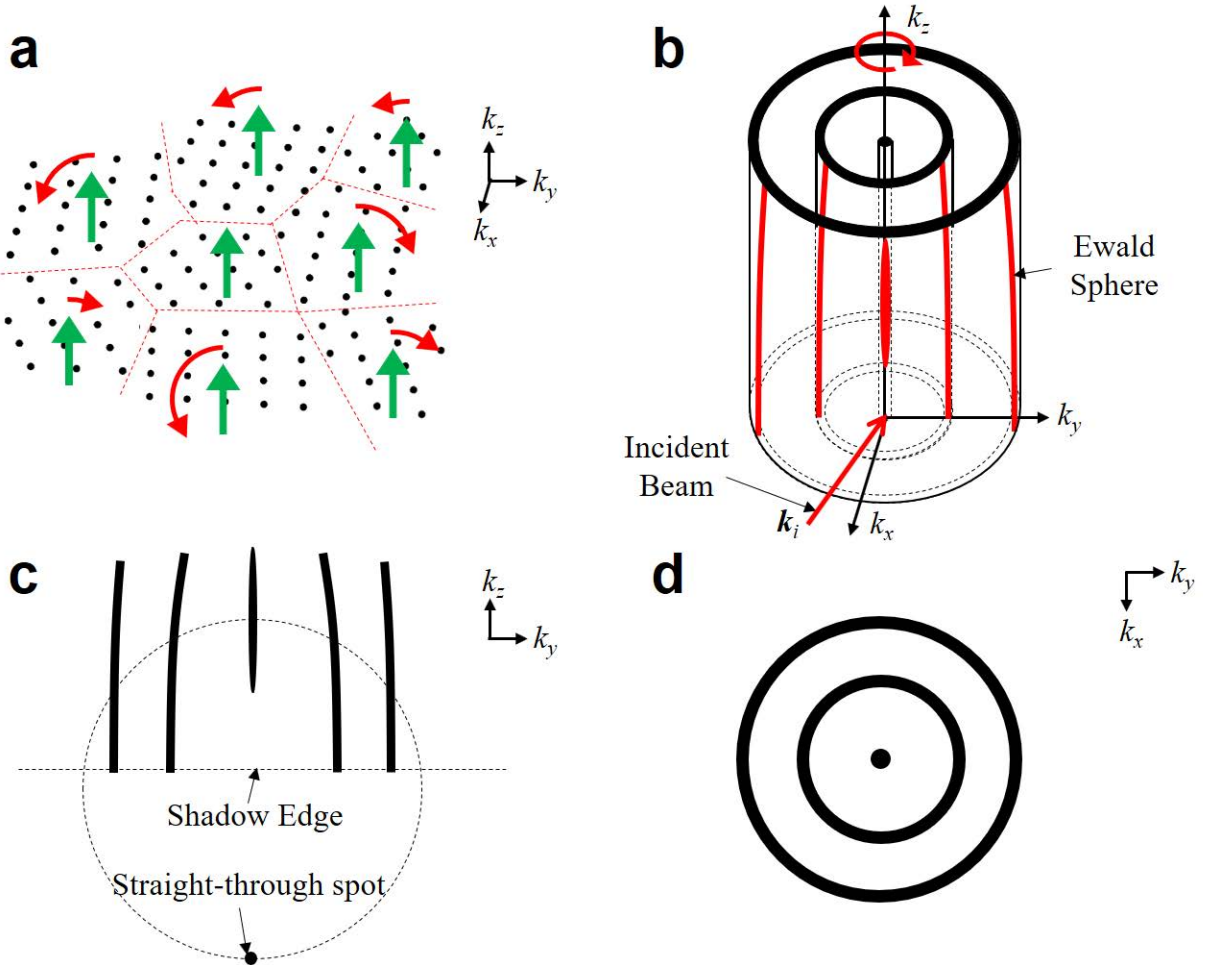


Figure 2.2: (a) A schematic of the real space structure of a 2D material consisted of randomly oriented grains. The curved red arrows represent random rotated grains and the straight up pointing green arrows represent the direction perpendicular to the substrate. (b) A schematic showing the 3D reciprocal space structure of the 2D material and how it cuts through the Ewald sphere, the curly red arrow represents the rotation around the sample normal direction at various azimuthal angle ϕ . (c) A simulated RHEED pattern, and (d) a schematic of the 2D reciprocal space structure of the 2D material with randomly oriented grains.

If a 2D material consists of grains with random in-plane orientations as shown in Fig. 2.2(a), then the 3D reciprocal space structure will be a set of concentric cylinders around k_z axis with different radii as shown in Fig. 2.2(b). The RHEED diffraction pattern will show streak-like intensity distribution that resembles Fig. 2.2(c). By looking into the $-k_z$ direction, the 2D reciprocal structure consists of a set of rings with different radii as shown in Fig. 2.2(d).

The two types of 2D materials presented above, a single crystal and a polycrystalline film, are extreme cases. Perhaps the more interesting case is a 2D film that is neither single crystal nor random polycrystalline. In this case, the 2D reciprocal structure of this 2D material contains broken rings and has a preferred in-plane orientation.

2.2 Experimental

2.2.1 Graphene Growth and Transfer

Graphene is perhaps the most well-known 2D layered material. It has been actively researched and possesses many remarkable electronic and optoelectronic properties⁶⁰. Graphene on SiO₂/Si (or other substrates) is commercially available. Typically, it is grown by chemical vapor deposition (CVD) technique on a Cu foil⁶¹ and then transferred to a SiO₂/Si substrate^{16, 17}. Since the Cu foil is not a single crystal, the nucleation of graphene at different regions on the Cu foil would possess different orientations. The net result is that the graphene grown on the Cu foil is polycrystalline in nature. However, it was shown that the orientation of the graphene grains is not completely random. In fact, the grains often show two dominant orientations with a 30° rotation with respect to each other and each orientation exhibits an angular spread⁶². The structures we analyzed are a commercially available graphene film (graphene-supermarket.com) and a homemade epitaxial graphene grown on Cu(111) substrate.

The commercial graphene film was grown by CVD on a Cu foil and then transferred to a SiO₂(~88 nm)/Si substrate. The homemade epitaxial graphene was grown by low pressure CVD on the Cu(111) films that were epitaxially grown on sapphire(0001) and spinel(111) substrates using DC sputtering² (see details of graphene growth in Chapter 1.3.1.1). The dimensions of both graphene samples are 1 cm × 1 cm. RHEED from four different kinds of homemade graphene samples will be presented in this chapter in order to compare the effect of substrates and the

number of graphene layers on RHEED patterns: a monolayer graphene as-grown on a twin-free Cu(111) film, a monolayer graphene as-grown on a twinned Cu(111) film, a monolayer graphene transferred onto a SiO₂/Si substrate, and a multilayer graphene transferred onto a SiO₂/Si substrate.

2.2.2 RHEED Data Collection

For RHEED characterization, the graphene samples were loaded into the RHEED vacuum chamber without any prior treatment. See Fig. 1.6 for the experimental setup. The RHEED system consists of an electron gun (model RDA-003G) which generates a 20 keV electron beam incident at a glancing angle of $\sim 1^\circ$ on the sample surface. The emission current used was 45 μ A. The RHEED pattern was projected on a phosphor screen mounted on a 6-in flange which was about 20 cm away from the sample in a vacuum chamber with a base pressure of 10^{-8} Torr. The RHEED pattern was captured by a digital camera positioned outside the chamber facing the phosphor screen. The sample was mounted on a holder with the sample's azimuthal rotation controlled by a stepper motor. In order to probe the entire upper half of the reciprocal space, the sample was rotated azimuthally with a 1.8° step size from 0° to 180° in 100 steps and the corresponding RHEED pattern was recorded at each incremental step^{27, 28}.

2.3 Results and Discussion

2.3.1 Commercial Graphene

2.3.1.1 SEM and AFM

Figures 2.3(a) and (b) show the SEM and AFM images, respectively. The images have the same scale bar of 2 μ m, but were taken from different places of the graphene. Both SEM and AFM images show a dominant single layer graphene with a small number of bi-layer graphene islands on top of a continuous layer of graphene. The bi-layer islands are indicated by the arrows in both figures. The thickness of the bi-layer island is about 8.4 \AA from an AFM line scan along the white

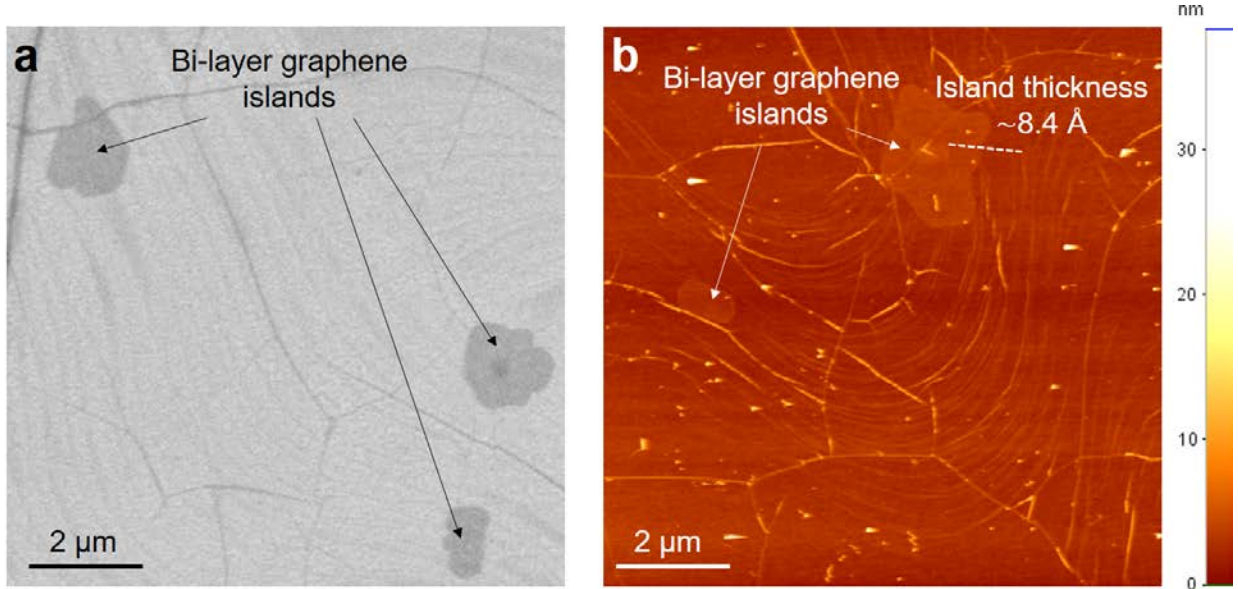


Figure 2.3: (a) An SEM image and (b) an AFM image showing different areas of the graphene surface. The arrows in both figures indicate bi-layer graphene islands. The z-scale bar indicating the surface height in the AFM image is shown on the right side of AFM image. The AFM line scan is represented by a white dashed line in (b). The darker wavy lines in (a) and brighter wavy lines in (b) are grain boundaries. The faint wavy lines in (a) and (b) are wrinkles in graphene.

dashed line indicated in Fig. 2.3(b). Grain boundaries (the dark, straight lines) and wrinkles (the light, wavy lines) of graphene are obvious in both images. The wrinkles are intrinsic of graphene due to the thermodynamic instability^{63, 64}.

2.3.1.2 RHEED

Figure 2.4(a) shows a typical RHEED pattern from the commercial graphene sample taken at a certain azimuthal angle (φ), which we defined as $\varphi = 0.0^\circ$. The scale bar was calibrated using the RHEED pattern of an epitaxial CdTe(100) film on a single crystal GaAs(100) substrate with a known lattice constant under the same experimental conditions⁶⁵. The pattern shows a strong broad streak at the center and two weak streaks at the left side and right side of the center streak. The two axes in the yellow coordinate system shown in Fig. 2.4(a) indicate the directions of k_\perp and k_\parallel , where $k_\perp \equiv k_z$ and $k_\parallel \equiv (k_x^2 + k_y^2)^{1/2}$, $k_x = k_\parallel \sin \varphi$ and $k_y = k_\parallel \cos \varphi$. The origin is chosen to be the straight through (S.T.) spot. The inset in Fig. 2.4(a) is the intensity line scan along

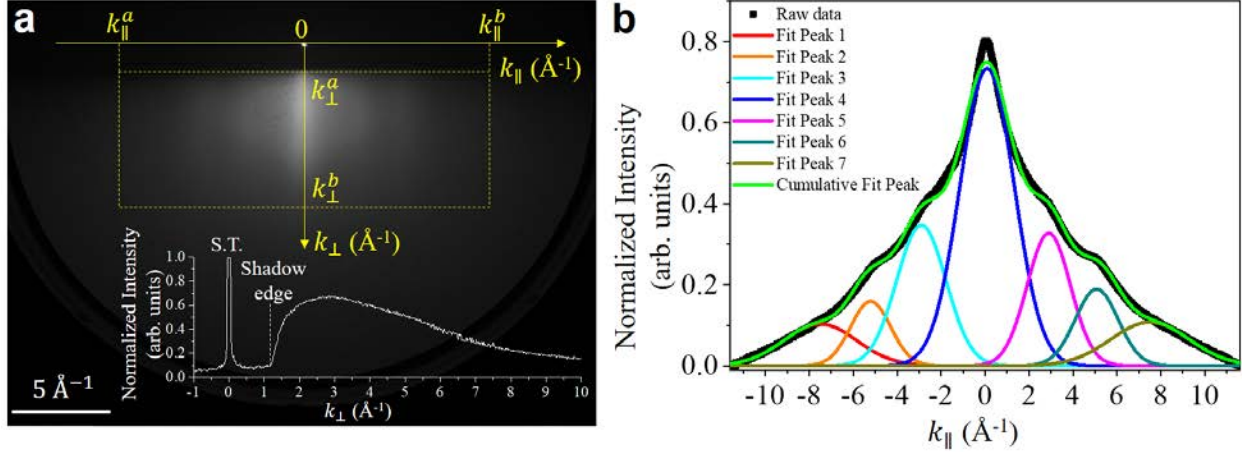


Figure 2.4: (a) A RHEED pattern collected from a commercial graphene sample with the 20 keV electron beam incident at $\varphi = 0.0^\circ$. The yellow coordinate system is centered at the straight through (S.T.) spot. The k_{\parallel} axis and k_{\perp} axes are parallel and perpendicular to the shadow edge, respectively. The inset in (a) shows an intensity line scan along the k_{\perp} axis. The black squares in (b) show the experimentally measured intensity along the k_{\parallel} axis, $I(k_{\parallel})$. The seven fit peaks and the cumulative fit peak are plotted in different colors. The peak number and the corresponding color are shown in the legend.

the k_{\perp} axis, showing that the intensity along the k_{\perp} axis is continuous beyond the shadow edge. For our graphene sample, the vertical distance between two graphene layers determined by an AFM line scan at the edge of a bi-layer graphene island is 8.4 Å. This means that the intensity would oscillate with a period of 0.75 \AA^{-1} ($= \frac{2\pi}{8.4 \text{ \AA}}$) and be suppressed at $k_{\perp} = i \times 0.37 \text{ \AA}^{-1}$ (where i is an odd number) if there is a substantial contribution of electron diffraction from the bilayer graphene islands⁶⁶. However, we did not observe such oscillation. This indicates that the diffraction intensity is dominated by the single layer graphene.

In order to analyze quantitatively the peak position and width of each streak shown in Fig. 2.4(a), we imported the RHEED patterns into the software ImageJ to extract the intensity profile. We assume the diffraction intensity distribution function in Fig. 2.4(a) is $f(k_{\parallel}, k_{\perp})$. Running a marco program written in ImageJ Marco Language, we obtained the normalized intensity $I'(k_{\parallel})$ as a function of k_{\parallel} through the following relation:

$$I'(k_{\parallel}) = \frac{\int_{k_{\perp}^a}^{k_{\perp}^b} f(k_{\parallel}, k_{\perp}) dk_{\perp}}{\int_{k_{\perp}^a}^{k_{\perp}^b} f(k_{\parallel}^{max}, k_{\perp}) dk_{\perp}}, (k_{\parallel}^a \leq k_{\parallel} \leq k_{\parallel}^b), \quad (2.1)$$

where k_{\parallel}^{max} is the k_{\parallel} position that maximizes the integral $\int_{k_{\perp}^a}^{k_{\perp}^b} f(k_{\parallel}, k_{\perp}) dk_{\perp}$. Specifically, the labeled positions $k_{\perp}^a, k_{\perp}^b, k_{\parallel}^a$ and k_{\parallel}^b in Fig. 2.4(a) are chosen to be 1.8 \AA^{-1} , 9.1 \AA^{-1} , -13.0 \AA^{-1} and 13.0 \AA^{-1} , respectively. The intensity is integrated along the k_{\perp} axis in order to improve the signal-to-noise ratio. The reason that we can use the integral is that the diffraction intensity mainly comes from a single layer graphene and the reciprocal rods of a single layer graphene are continuous and featureless along the k_{\perp} axis. Since the intensity profile in principle should be symmetric about the k_{\perp} axis, a linear background intensity is subtracted from $I'(k_{\parallel})$ (normalized to 1) to correct the experimental uncertainty. Then we obtain $I(k_{\parallel})$:

$$I(k_{\parallel}) = I'(k_{\parallel}) - \left[\frac{I'(k_{\parallel}^b) - I'(k_{\parallel}^a)}{k_{\parallel}^b - k_{\parallel}^a} k_{\parallel} + \frac{I'(k_{\parallel}^b)k_{\parallel}^a - I'(k_{\parallel}^a)k_{\parallel}^b}{k_{\parallel}^b - k_{\parallel}^a} \right], (k_{\parallel}^a \leq k_{\parallel} \leq k_{\parallel}^b). \quad (2.2)$$

The raw data points (black squares) in Fig. 2.4(b) show the intensity profile $I(k_{\parallel})$ obtained experimentally. The raw data points can be fitted using seven Gaussians. The seven fit peaks and the cumulative fit peak are also plotted in different colors in Fig. 2.4(b). The RHEED diffraction pattern shown in Fig. 2.4(a) is actually made up of seven broad streaks. Theoretical prediction and experimental result of the peak positions are listed in Table 2.1. Graphene has a hexagonal lattice with a lattice constant $a_0 = 2.464 \text{ \AA}$. $\vec{G}(hk)$ is the reciprocal space lattice vector associated with the Miller index (hk) and its magnitude $|\vec{G}(hk)| = \frac{4\pi}{\sqrt{3}a_0} \sqrt{h^2 + hk + k^2}$. The peak positions and full-width-at-half-maximum (FWHM)s are obtained from the Gaussian fits of the peaks. The peak broadening is a result of a combined effect of the orientational angular spreads and the wrinkles (roughness) of the graphene layer⁶⁶. The $(\bar{2}0)$ is missing since the reciprocal distance ($\sim 0.8 \text{ \AA}^{-1}$)

Table 2.1: Theoretical prediction of peak positions and experimentally measured peak positions and FWHMs of peaks

$(\mathbf{h}\mathbf{k})$	Theoretical $ \vec{G}(\mathbf{h}\mathbf{k}) $ (\AA^{-1})	Experimental peak position (\AA^{-1})	Experimental FWHM (\AA^{-1})
($\bar{2}\bar{1}$)	7.790	- 7.5 ± 0.2	3.9 ± 0.3
($\bar{2}0$)	5.889	-	-
($\bar{1}\bar{1}$)	5.100	- 5.2 ± 0.1	2.1 ± 0.1
($\bar{1}0$)	2.944	- 2.9 ± 0.1	2.7 ± 0.2
(00)	0	0.1 ± 0.1	2.9 ± 0.1
(10)	2.944	2.9 ± 0.1	2.3 ± 0.1
(11)	5.100	5.1 ± 0.1	2.3 ± 0.2
(20)	5.889	-	-
(21)	7.790	7.5 ± 0.2	4.2 ± 0.3

between ($\bar{2}0$) and ($\bar{1}\bar{1}$) is much smaller than the average FWHM ($> 2 \text{ \AA}^{-1}$) of these streaks. According to the Rayleigh criterion for the resolution limit ⁶⁷, we would not be able to resolve them. The same argument applies to the absence of the (20) peak.

For a single crystal graphene, however, (00), (10) and (11) are not collinear points in the reciprocal space. The planar-like Ewald sphere would not cut through them simultaneously at any azimuthal angle. The fact that they show up at the same time in a single RHEED pattern leads us to conclude that the graphene sample is not a single crystal. To study the in-plane orientation distribution of the graphene grains, we constructed the experimental 2D reciprocal structure for this sample. The 2D reciprocal structure is the cross-section view of the reciprocal space by looking into the $-k_{\perp}$ direction. It is constructed by plotting the intensity as a function of k_{\parallel} at different φ . At each φ , an intensity profile $I_{\varphi}(k_{\parallel})$ similar to that shown in Fig. 2.4(b) is extracted from the corresponding RHEED pattern. Plotting the azimuthal-dependent intensity profile $I_{\varphi}(k_{\parallel})$ in a polar coordinate system with the radius being k_{\parallel} and the polar angle being φ , and representing the

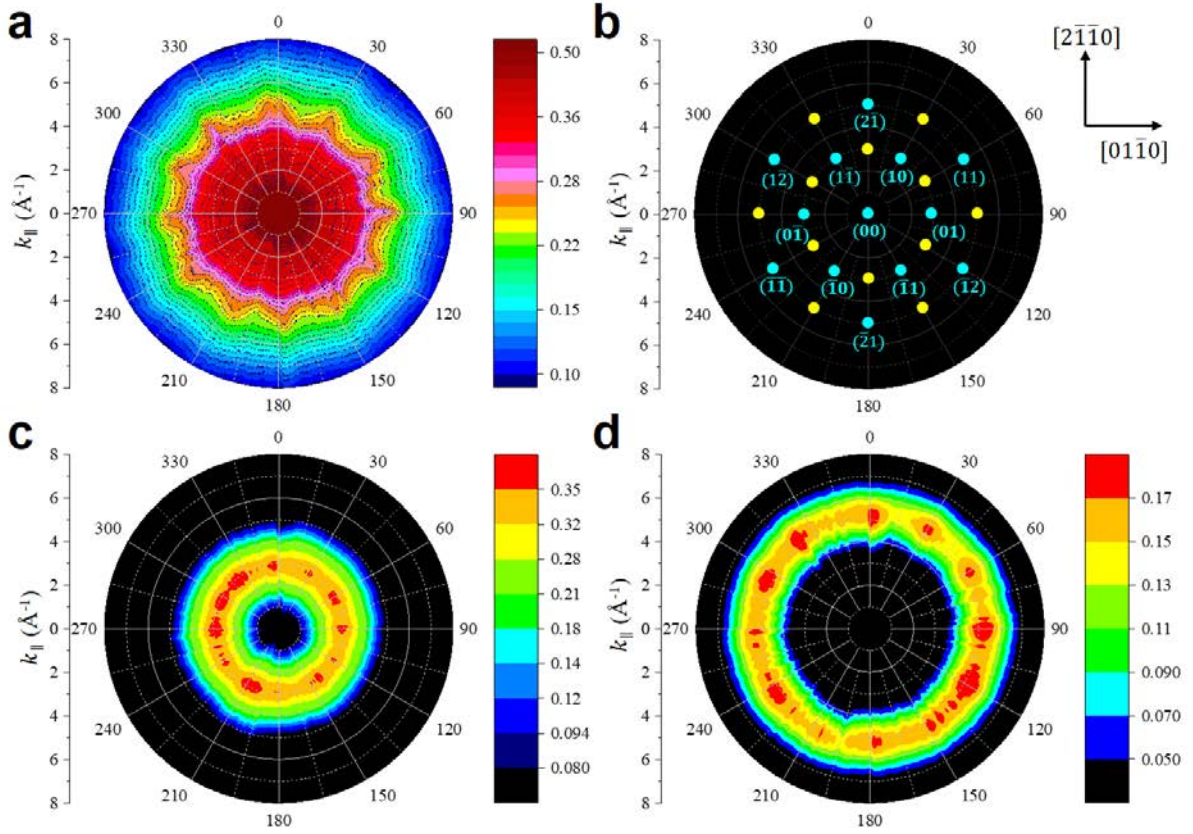


Figure 2.5: (a) The RHEED 2D reciprocal space structure measured from the commercial graphene sample. (b) The theoretical 2D reciprocal space structure of the graphene layer. The cyan spots are 2D reciprocal lattice points of a single crystal graphene with the corresponding (hk) indices labeled. The yellow spots are rotated 30° from the cyan spots with the k_{\perp} direction as the rotation axis. $k_x = k_{\parallel} \sin \varphi$ and $k_y = k_{\parallel} \cos \varphi$. The arrows on the right side indicate the in-plane directions for graphene, $[2\bar{1}\bar{1}0]$ and $[01\bar{1}0]$ along $\varphi = 0^\circ$ and 90° , respectively. (c) and (d) show the $I(k_{\parallel}, \text{inner})$ and $I(k_{\parallel}, \text{outer})$ plotted in the polar coordinate system. These intensity distributions of the inner peaks and outer peaks are extracted from the RHEED 2D reciprocal space structure in (a).

intensity by different colors, we get the 2D reciprocal space structure of this graphene sample as shown in Fig. 2.5(a).

The most striking feature of Fig. 2.5(a) is the circularly wavy contours at $k_{\parallel} \approx 5 \text{ \AA}^{-1}$ that exhibit twelve approximately evenly spaced peaks. For a single crystal graphene, theoretically there should be only six peaks, whose (hk) indices are (11) , $(\bar{1}2)$, (21) , $(\bar{1}\bar{1})$, $(1\bar{2})$, $(2\bar{1})$, at $k_{\parallel} = 5.1 \text{ \AA}^{-1}$. The existence of twelve peaks confirms that the graphene is not a single crystal. The twelve

peaks can be explained if we assume that the graphene has two dominant orientations with a 30° rotation with respect to each other. To illustrate this point, a theoretical model of the 2D reciprocal space structure is presented in Fig. 2.5(b). The cyan spots are the 2D reciprocal lattice points of single crystal graphene and the yellow spots are rotated 30° from the cyan spots around the k_{\perp} axis. This theoretical model consists of a (00) spot at the center, the inner 12 spots at $k_{\parallel} = 2.9 \text{ \AA}^{-1}$ and the outer 12 spots at $k_{\parallel} = 5.1 \text{ \AA}^{-1}$. The twelve peaks of the contour lines in Fig. 2.5(a) match well with the outer 12 spots in Fig. 2.5(b). However, the inner spots in Fig. 2.5(b) are not obviously seen in Fig. 2.5(a) due to overlapping with the high intensity of the center peak.

At every azimuthal angle φ , the intensity profile $I_{\varphi}(k_{\parallel})$ can be decomposed into seven Gaussian profiles by doing multiple peak fit similar to that in Fig. 2.4(b). That is:

$$I_{\varphi}(k_{\parallel}) = \sum_{i=1}^7 I_i(k_{\parallel}). \quad (2.3)$$

The center positions of the Gaussian profiles $I_1(k_{\parallel})$ to $I_7(k_{\parallel})$ range from about -7.5 \AA^{-1} to about 7.5 \AA^{-1} . $I_2(k_{\parallel})$ and $I_6(k_{\parallel})$ constitute the outer peaks in Fig. 2.5(a) while $I_3(k_{\parallel})$ and $I_5(k_{\parallel})$ constitute the inner peaks which are not obvious in Fig. 2.5(a). That is:

$$I_{\varphi}(k_{\parallel}, \text{outer}) = I_2(k_{\parallel}) + I_6(k_{\parallel}), \quad (2.4a)$$

$$I_{\varphi}(k_{\parallel}, \text{inner}) = I_3(k_{\parallel}) + I_5(k_{\parallel}). \quad (2.4b)$$

Plotting $I(k_{\parallel}, \text{inner})$ and $I(k_{\parallel}, \text{outer})$ in a similar way as in Fig. 2.5(a), we obtain Fig. 2.5(c) and Fig. 2.5(d), respectively. In this way, we can present the intensity contributions from the inner and the outer peaks separately from the combined intensity shown in Fig. 2.5(a).

In both Fig. 2.5(c) and Fig. 2.5(d), we observed some localized intensities on a continuous ring. The positions of those localized intensities in Fig. 2.5(c) and Fig. 2.5(d) match the theoretical inner 12 spots and the theoretical outer 12 spots shown in Fig. 2.5(b), respectively. This leads to a

qualitative picture on the grain orientation of the commercial graphene sample. That is, some of the graphene grains are randomly oriented while others prefer to orient with a 30° rotation with respect to each other. This is consistent with the results from transmission electron microscopy (TEM) analyses of a CVD grown graphene suspended on TEM grid by Huang *et al.*⁶².

2.3.2 Homemade Epitaxial Graphene

2.3.2.1 SEM, AFM and EBSD

Figure 2.6(a) shows the SEM image of a Cu film, without twin domains, on sapphire(0001), after the thermal annealing and the graphene growth. Clearly different from its original form, the Cu surface is smooth and free of pits. The inset in Fig. 2.6(a) shows a Raman spectrum collected from this surface with a 514 nm laser line. Characteristic 2D (2712 cm^{-1}) and G (1591 cm^{-1}) peaks of graphene can be identified, confirming the occurrence of graphene growth on this surface. Given the high intensity ratio of 2D/G, along with the fact that no noticeable defect D peak can be detected, it is inferred that the graphene is monolayer and is of high quality. The central bump-up of the spectral profile is believed to be caused by the surface plasmon emission of Cu⁶⁸. Given that the energy gap between Fermi level and *d* state of Cu is around 2.1 eV or 590 nm⁶⁹, theoretically there would be a broad emission peak centered at 2506 cm^{-1} under an excitation of 514 nm. In this work, the emission is experimentally observed around 2200 cm^{-1} , implying that the actual Cu emission peak is at around 580 nm for this particular Cu film. We believe this deviation is very reasonable, considering that the FWHM of Cu emission peak in ref 47 is about 100 nm wide.

Figure 2.6(b) shows the EBSD crystallographic orientation map of this Cu film using the IPF-Z component. The super homogeneity of color in this map indicates that the twin boundaries have been completely removed after the thermal annealing and the graphene growth. The Cu{111}

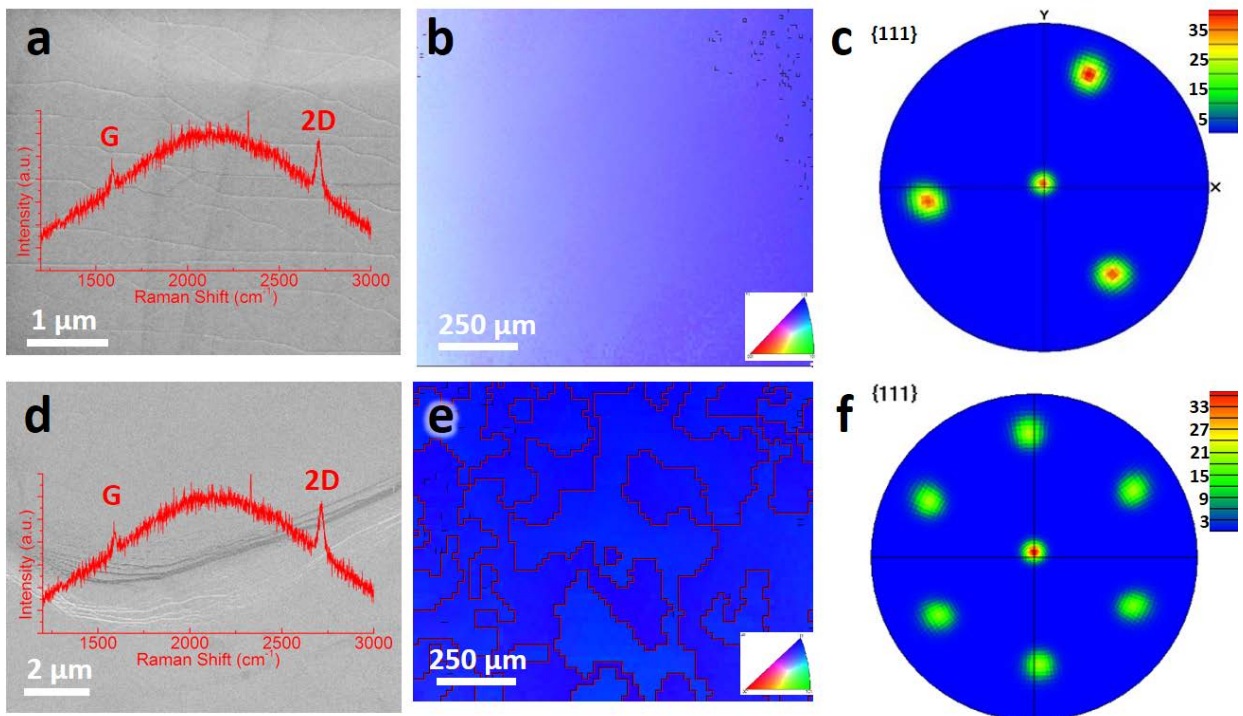


Figure 2.6: (a) SEM image of the Cu film without twin domains on a sapphire(0001) substrate after thermal annealing and graphene growth; overlay shows a Raman spectrum acquired from this sample. G and 2D peaks are labeled in the spectrum. (b) EBSD crystallographic orientation map of the Cu film without twin domains on a sapphire(0001) after thermal annealing and graphene growth using IPF-Z mapping component. (c) EBSD Cu{111} pole figure of the Cu film without twin domains on a sapphire(0001) after thermal annealing and graphene growth. (d) SEM image of the Cu film with twin domains on a sapphire(0001) substrate after thermal annealing and graphene growth; overlay shows a Raman spectrum acquired from this sample. (e) EBSD crystallographic orientation map of the Cu film with twin domains on a sapphire(0001) substrate after thermal annealing and graphene growth using IPF-Z mapping component. (f) EBSD Cu {111} pole figure of the Cu film with twin domains on a sapphire(0001) after thermal annealing and graphene growth.

EBSD pole figure in Fig. 2.6(c) presents a clean 3- fold symmetry, also confirming that the film is free of twin domains.

On the other hand, it has been found that the twin domains sometimes are tough to remove for the Cu film on sapphire(0001). Figure 2.6(d) shows the SEM image of a Cu film, still with twin domains, on sapphire(0001) after the thermal annealing and the graphene growth. Despite the film is smooth and free of pits as in the case of Fig. 2.6(a), a boundary groove can be clearly seen

in the middle of this image. Nonetheless, these grooves do not seem to affect the graphene growth, since high-quality and monolayer graphene can still be found on this surface as evident by the Raman spectrum inset of Fig. 2.6(d). The G and 2D peak are located at 1588 and 2719 cm⁻¹, respectively. The EBSD IPF-Z crystallographic orientation map in Fig. 2.6(e) confirms that these boundaries are the same twin boundaries as prior to the thermal annealing and the graphene growth. However, note that the size of twin domains increases approximately by 2 orders of magnitude. The Cu{111} EBSD pole figure in Fig. 2.6(f) confirms that these twin domains remain to be in-plane rotated by 60°, and the fraction of these twin domains is still about half of the Cu film, similar to that in the as-sputtered Cu film. Overall, it is found that the status of Cu films, twin-free or twinned, after the thermal annealing and graphene growth is very sensitive to the sapphire substrate's surface pretreatment, the Cu sputtering parameters, and the thermal annealing conditions^{70, 71}. Any small parameter fluctuations will cause the failure of the single crystal Cu formation. In our work, more than 50% Cu films on sapphire remain to be twinned while we try our best to minimize the variation of processing conditions. The situation may become worse if the sapphires are recycled for sputter deposition of Cu. In contrast, for the Cu film sputtered on spinel(111), it is consistently found to be twin-free after the thermal annealing and graphene growth.

Figure 2.7(a) shows the optical image of a continuous graphene (10 mm × 10 mm) layer transferred to a SiO₂(50 nm)/Si substrate. The edge area of graphene (bottom portion of Fig. 2.7(a)) is intentionally covered in this image for contrast. Five Raman spectra were randomly collected on this graphene sheet. Figure 2.7(b) shows that all spectra indicate the graphene to be monolayer in light of the peak area intensity ratio of 2D/G (4.10 ± 0.36). Different from the pre-transferred counterparts, these post-transferred spectra have the so-called defect D peak present in each of

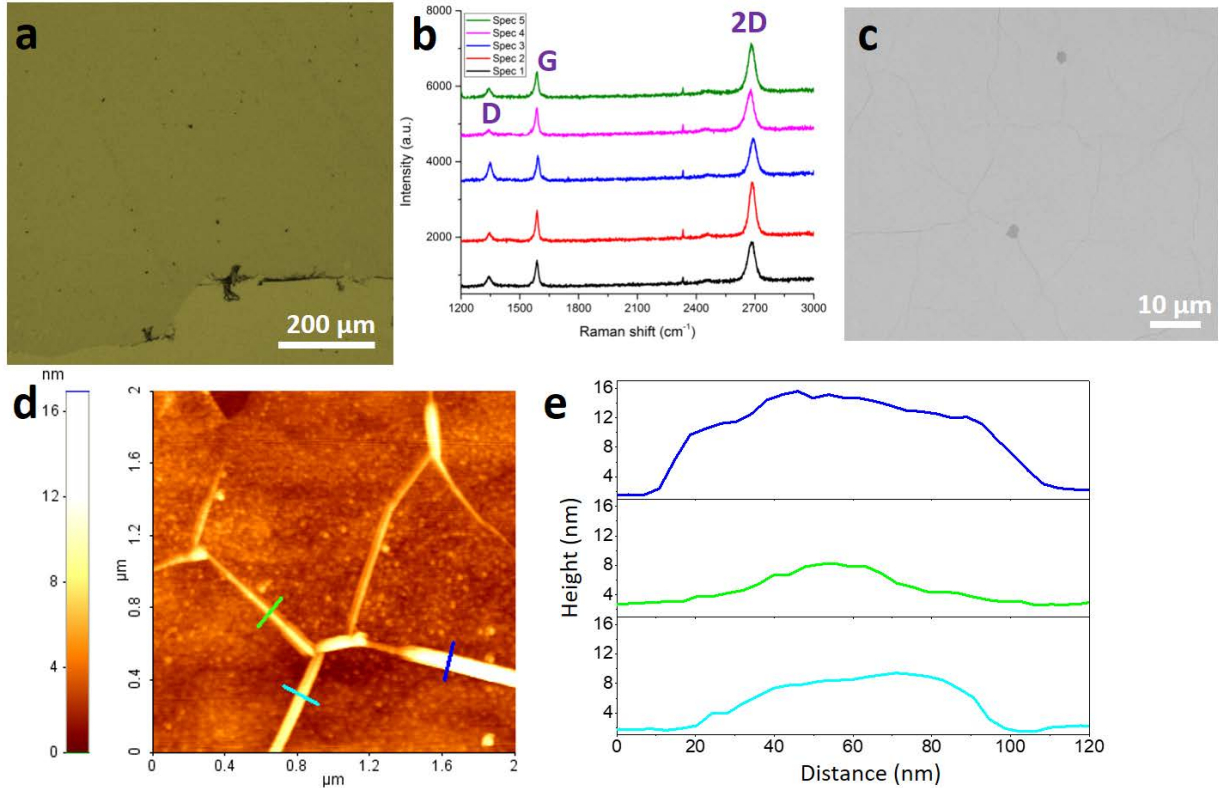


Figure 2.7: (a) Optical image of the continuous monolayer graphene sheet transferred to a SiO₂/Si substrate. (b) Collected Raman spectra from random areas on the continuous monolayer graphene sheet transferred to a SiO₂/Si substrate. (c) SEM image of the monolayer graphene sheet transferred to a SiO₂/Si substrate. (d) AFM image and (e) three line scan profiles across the wrinkles in the monolayer graphene transferred to a SiO₂/Si substrate.

them^{72, 73}, probably resulting from the transfer process. The D, G, and 2D peak positions for this transferred graphene are 1344 ± 3 , 1588 ± 2 , and 2683 ± 6 cm⁻¹, respectively. Another difference between the pre- and post-transferred Raman spectra is the substantial redshift of the 2D peak, from the pre-transferred to post-transferred. This may be related to the strain during graphene growth on Cu(111) surface. The SEM image of the transferred graphene is shown in Fig. 2.7(c). It can be seen that the image is dominated by the light gray color which represents the monolayer graphene. Under the view, there are indeed a few dark gray flakes corresponding to multilayer graphene, but the fraction of these features is too small to be significant. Also, the size of these flakes is small (1–2 μm) and undetectable by the Raman spectroscopy. In addition, line features

can be clearly observed in Fig. 2.7(c). Two reasons lead us to believe these lines are the wrinkles formed during graphene's relaxation on the SiO₂/Si substrates, rather than grain boundaries or boundaries of other kinds. The first reason will be elaborated with the aid of RHEED results in the next section, where it is shown that the transferred graphene is single-crystalline and should be free of large-angle grain boundary. The second reason is from the AFM scanning on these lines. The AFM image in Fig. 2.7(d) reveals the details of these lines, which seem to be an outcome of graphene buckling. Further evidence comes from Fig. 2.7(e). The zoom-in line profiles across these features are quite smooth with small slopes of ~ 0.13 ($\sim 7.45^\circ$), indicating the features are more likely to be wrinkles that are intrinsic to graphene^{63, 64}.

2.3.2.2 RHEED

Firstly, we show in Figs. 2.8(a) and (b) a pair of RHEED patterns acquired from a monolayer graphene on a twin-free Cu(111) film at two representative φ of 0 and 30.6°, respectively. The central streak represents the (00) lattice of the reciprocal space of graphene, while additional streaks come from the non-zero k_{\parallel} vectors $\vec{G}(hk)$ in the reciprocal space. The corresponding indexing of streaks can be found in Figs. 2.8(a) and (b). The directions of the line intensity profile scans, blue in Fig. 2.8(a) and red in Fig. 2.8(b), are illustrated in Fig. 2.8(c), where \vec{b}_1 and \vec{b}_2 are the primitive vectors in the reciprocal space of graphene. Figure 2.8(d) shows the intensity profiles of these line scans as a function of k_{\parallel} (the distances from (hk) to (00)) at a fixed perpendicular momentum transfer k_{\perp} . With these measurements, we can experimentally determine $|\vec{b}_1| = |\vec{b}_2| = 2.95 \pm 0.05 \text{ \AA}^{-1}$, which agrees very well with that of graphene reported in the literature⁷⁴.

Next, to investigate the in-plane crystallography of this graphene, we construct its 2D reciprocal space structure by collecting 100 RHEED patterns from 100 azimuthal angles (from 0

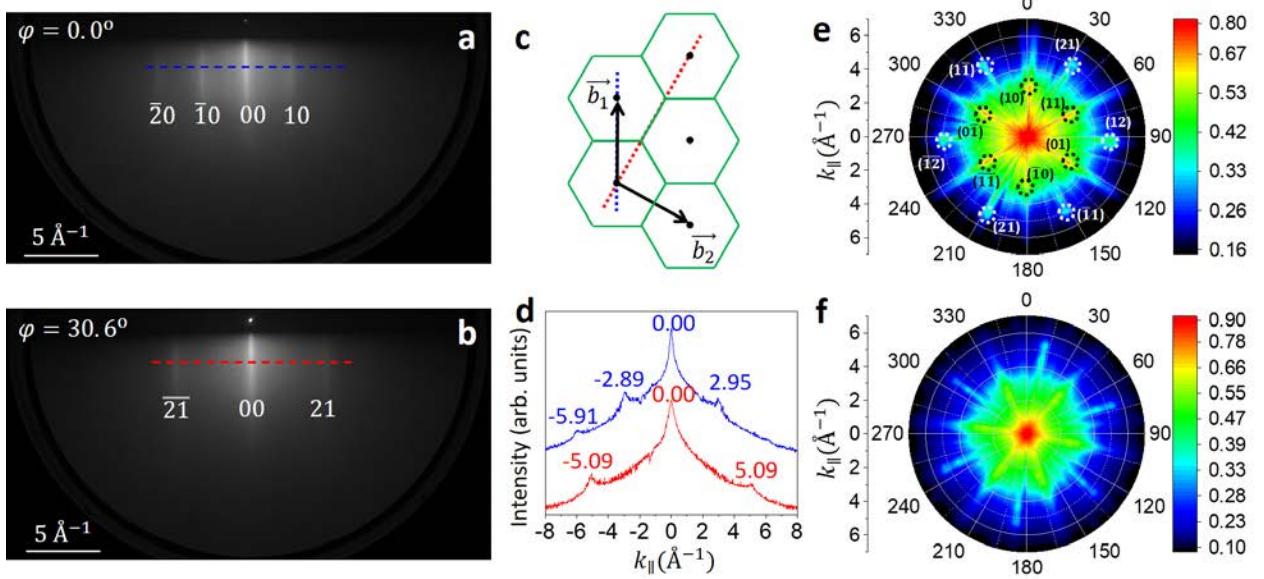


Figure 2.8: (a, b) RHEED patterns of the monolayer graphene on a twin-free Cu(111) film when the electron beam incident at azimuthal angles $\varphi=0$ and 30.6° , respectively. The two-dimensional Miller index (hk) is labeled in (a) and (b). The \vec{b}_1 and \vec{b}_2 are unit vectors in the reciprocal space. The scale bar is 5 \AA^{-1} . (c) Schematics showing the directions of blue and red dashed lines in the reciprocal space (RHEED patterns) of a monolayer graphene shown in (a) and (b), respectively. (d) Intensity profiles along the blue and red dashed lines in (a) and (b), respectively. (e) Experimentally acquired reciprocal space structure of the monolayer graphene on a twin-free Cu(111) film. The (hk) pole locations are labeled and circled by dashed circles. (f) Experimentally acquired reciprocal space structure of the monolayer graphene on a twinned Cu(111) film.

to 180° , step size 1.8°). We first measure the intensity profile at each angle, and then plot the azimuthal angle-dependent intensity profile in a polar coordinate system. In this 2D reciprocal space structure, the radius represents the reciprocal distance from the (00) spot and the polar angle represents the azimuthal angle. Figure 2.8(e) shows the reciprocal space structure of the monolayer graphene on a twin-free Cu(111) film. In this figure, there are clearly six symmetrical spots, namely, (21) , (12) , $(\bar{1}1)$, $(\bar{2}1)$, $(\bar{1}\bar{2})$, and $(1\bar{1})$, at a reciprocal distance of 5.1 \AA^{-1} from the center. In addition, at a shorter reciprocal distance of 2.9 \AA^{-1} , there are six more symmetrical spots, namely, (10) , (11) , (01) , $(\bar{1}0)$, $(\bar{1}\bar{1})$, and $(0\bar{1})$, each rotated 30° in the azimuthal angle with respect to the previous set. The symmetry and the position of these spots agree with the theoretical

calculation on a single-crystalline graphene. Thus, the graphene under investigation is indeed in single-crystalline form. Furthermore, we construct the reciprocal space structure of the monolayer graphene on a twinned Cu(111) film, shown in Fig. 2.8(f). A previous study⁷⁵ reported that the graphene growth direction is rotated 30° when crossing the 60° in-plane twin boundaries. In this study, however, no additional rotational spots can be found in Fig. 2.8(f) besides those can be indexed similarly as in Fig. 2.8(e). In other words, the graphene grown on twinned Cu(111) films is in single-crystalline form without additional 30° rotation domains caused by the twin boundaries. It is possible that in our present experiment, the graphene growth direction is rotated 60° in-plane at the Cu twin boundaries in response to their interruption. Since graphene is six-fold symmetric, this 60° rotation is equivalent to no rotation in terms of in-plane orientation.

While harmless to in-plane crystal orientation, the twin boundaries do affect the graphene growth in some other ways. Figures 2.9(a) and (b) show the optical images of post-transferred bilayer and multilayer graphene grown on twinned Cu(111) films. Overall, the bilayer and multilayer graphene flakes are scattered everywhere on the monolayer graphene base, but they appear to have a preference in selecting locations. The blue dashed lines in Fig. 2.9(a) and (b) are guides of graphene morphology to the eyes. It is seen that graphene tends to grow into bilayer or multilayer along these dashed lines. After checking the size and shape of these lines, it can be recognized that the lines reflect the twin boundaries in the Cu films. The EBSD crystallographic orientation map of the Cu film with twin domains on a sapphire(0001) substrate after thermal annealing and graphene growth using IPF-Z mapping component in Figure 2.6(e) can be used as a reference. Thus, we believe the twin boundaries tend to serve as nucleation sites for graphene to grow into multilayer. This is not unexpected, given the feature of twin boundaries. From the SEM image in Fig. 2.6(d), one can see that the twin boundaries are essentially grooves with multiple

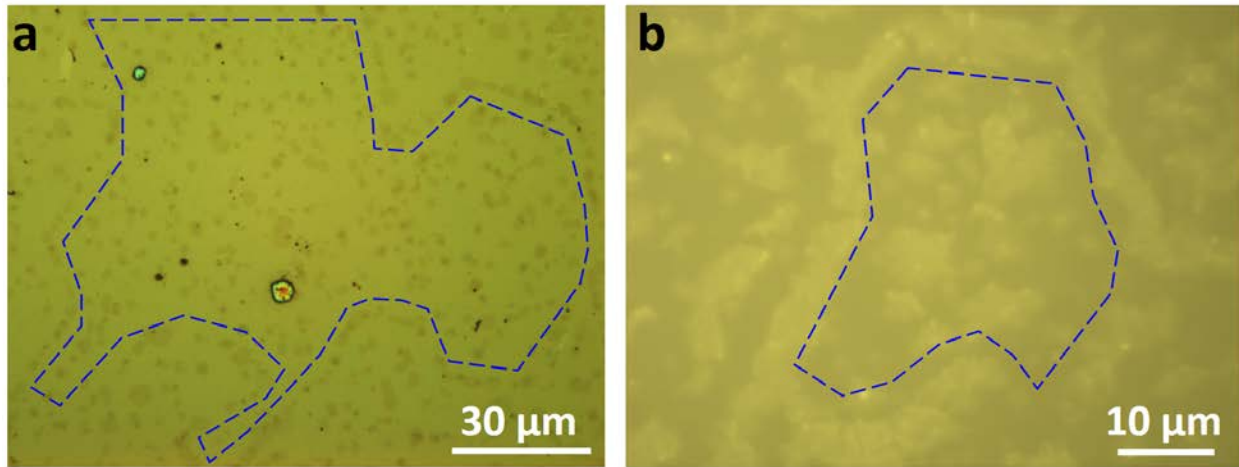


Figure 2.9: (a) Optical image of the bilayer graphene sheet transferred from a twinned Cu(111) film to a SiO₂/Si substrate. (b) Optical image of the multilayer graphene sheet transferred from a twinned Cu(111) film to a SiO₂/Si substrate. The dashed outlines are speculated to reflect the twin boundaries in Cu films.

steps. From the thermodynamics perspective of materials, the features such as steps are particularly favorable for materials to nucleate. It is no exception for graphene when it comes to nucleation on Cu(111)⁷⁶.

What makes this azimuthal RHEED technique more appealing is that it can be used to determine the symmetry of graphene even after the graphene is transferred to SiO₂/Si substrates, which carries a special significance from the perspective of making graphene-based electronic devices. Figures 2.10(a) and (b) show a representative RHEED pattern and the reciprocal space structure of a monolayer graphene transferred to a SiO₂/Si substrate, respectively. There appears to be a spread in the streaks in Fig. 2.10(a) and, in turn, in the spots in Fig. 2.10(b). To better view, we decompose the mapping of Fig. 2.10(b) into two separate regimes representing the inner and outer spots as shown in Figs. 2.10(c) and (d), respectively. In each mapping, especially the latter, the six-fold symmetry of single-crystalline graphene can be visualized again, suggesting the crystallographic property of post-transfer graphene can be preserved. The spread of the spots for

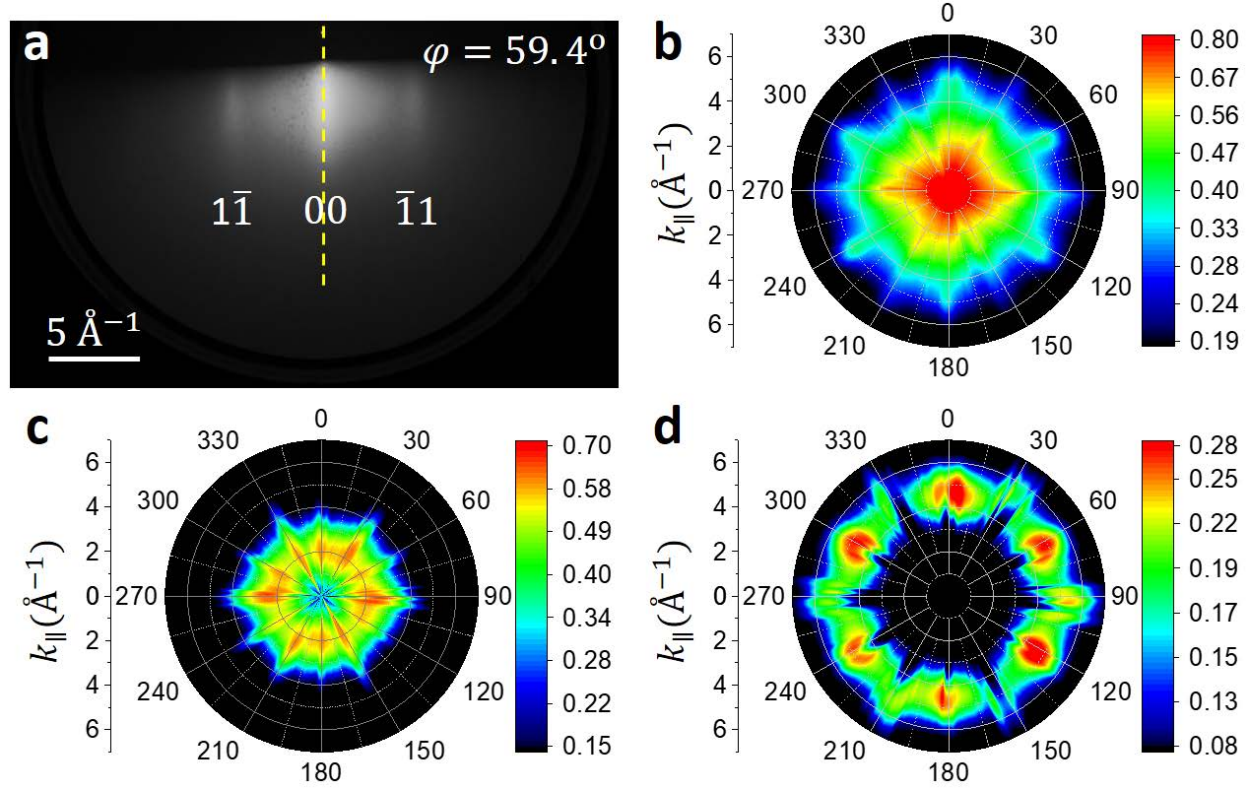


Figure 2.10: (a) RHEED pattern of the monolayer graphene transferred to a SiO_2/Si substrate collected at the azimuthal angle $\varphi = 59.4^\circ$. (b) Experimentally acquired reciprocal space structure of the monolayer graphene transferred to a SiO_2/Si substrate. (c, d) Decomposition of (b) to show (c) inner six spots and (d) outer six spots.

this sample is probably due to the electron scattering from the ripples, similar to that observed on the broadening of the TEM diffraction beams from a graphene layer⁶⁶.

We also use azimuthal RHEED to study the structure of a multilayer graphene transferred to a SiO_2/Si substrate. The representative RHEED pattern and reciprocal space structure of this sample are shown in Figs. 2.11(a) and (b), respectively. Compared to Fig. 2.11(b), Fig. 2.11(b) displays much sharper spots. This is due to the decreasing of ripple density in multilayer graphene. Unlike single layer graphene, multilayer graphene can stabilize itself without creating too many ripples. Also note that the multilayer graphene is still in single-crystalline form per Fig. 2.11(b). In fact, Fig. 2.11(b) may represent what a single-crystalline graphite would produce. According to a reference⁷⁷ and graphite's $\{10\bar{1}1\}$ theoretical pole figure projected onto the (0001) plane, a

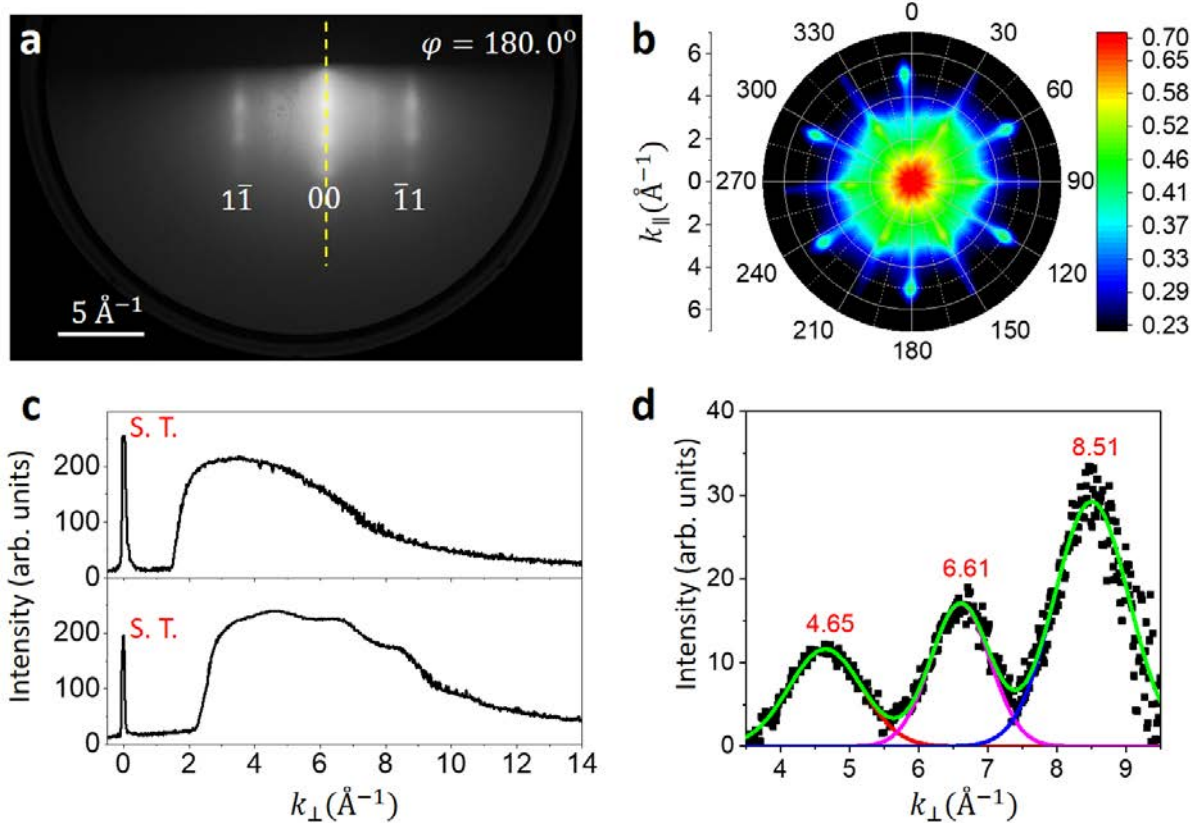


Figure 2.11: (a) RHEED pattern of the multilayer graphene transferred to a SiO_2/Si substrate collected at the azimuthal angle $\varphi = 180^\circ$. (b) Experimentally acquired reciprocal space structure of the multilayer graphene transferred to a SiO_2/Si substrate. (c) Intensity profiles vs momentum transfer perpendicular to the substrate (k_{\perp}) along the yellow dashed lines in RHEED patterns shown in Figure 2.10(a) and Fig. 2.11(a). S.T. stands for the straight through incident electron beam landed on the phosphorus screen. (d) Peak fitting of the intensity profile in the lower part of (c) after background subtraction.

single-crystalline graphite indeed has a six-fold symmetry. In summary, we believe the graphite-like multilayer graphene gives rise to the sharp RHEED patterns and thus a sharp reciprocal space structure, but monolayer graphene has difficulty to do so because it contains lots of wrinkles.

In the representative RHEED patterns of the monolayer graphene (Fig. 2.10(a)) and the multilayer graphene (Fig. 2.11(a)), one can see that each streak for the monolayer graphene is continuous along vertical direction, while beading can be observed on the streaks for the multilayer graphene. This is caused by the change in reciprocal space structure from monolayer to multilayer

graphene⁵⁶. Here we plot the intensity profiles along the central streaks as indicated by the yellow dashed lines. Shown in Fig. 2.11(c), the intensity profile is smooth for the monolayer graphene (upper panel), but oscillates for the multilayer graphene (bottom panel). After using the profile of monolayer graphene as the background for subtraction, we resolve the oscillation curve with a period of $\Delta = 1.93 \pm 0.04 \text{ \AA}^{-1}$ for the multilayer, shown in Fig. 2.11(d). The oscillation implies that this graphene contains multiple layers whose interlayer spacing (d) can be estimated to be $d = 2\pi/\Delta = 3.27 \pm 0.07 \text{ \AA}$. Note that the interplanar distance between graphite's layers is 3.35 \AA . Therefore, the RHEED technique is also able to probe the crystallographic properties of multilayer graphene along the out-of-plane direction.

Last, we make some remarks on the azimuthal RHEED method. Regarding the comparison between LEED and our azimuthal RHEED for graphene studies, there are pros and cons in each. When graphene is on conductive substrates, LEED is certainly more powerful. LEED is simpler in that the electron beam incidents on the area of interest and gets the diffraction pattern of graphene directly. In azimuthal RHEED, a large number of patterns between $\varphi = 0^\circ$ and 360° have to be collected to construct the reciprocal space mapping of graphene and then reveal the crystallinity. Also, LEED can directly tell the epitaxial alignment of graphene on the substrate. In azimuthal RHEED, this is also doable, but has to be done in a more complex manner by keeping track of the geometry of graphene sheet since the graphene is already transferred out of the original substrate. However, for graphene on some insulating substrates, it is a completely different story. The proposed azimuthal RHEED method in this work becomes more powerful in this scenario as LEED is not suitable for insulating materials.

2.4 Conclusion

We present a method to construct the reciprocal space structure of 2D materials using RHEED. The diffraction patterns were obtained at different in-plane azimuthal angle φ of the sample by rotating the sample with respect to the surface normal. At each in-plane angle, the intensity is expressed as a function of momentum transfer parallel to the substrate k_{\parallel} . The reciprocal space structure is therefore represented by the intensity distribution $I(k_{\parallel})$ as a function of the momentum transfer parallel to the substrate for all in-plane azimuthal angles. This method does not require extensive 2D sample preparation and can be applied to other 2D materials. We have verified the feasibility of this method to determine the symmetry of post- transferred and large area graphene, both commercial and homemade, on SiO₂/Si substrates, which represents an important step toward better understanding the structure of graphene before using it to make large area devices.

3. ARHEED CHARACTERIZATION OF TRANSITION METAL DICHALCOGENIDES

3.1 Introduction

The layered metal chalcogenide (LMC) materials have rich fundamental physical and chemical properties and potential applications in electronics and optoelectronics, which has stimulated intense research activities world-wide in recent years⁷⁸. An LMC material consists of a stacking of two-dimensional MX_n layers where M is a metal and X is a chalcogen atom from S, Se or Te⁷⁹. A unique characteristic of this class of materials is that the chalcogenide atoms are chemically saturated and, as a result, the weak inter-layer interactions are dominated by the van der Waals force⁸⁰.

One of the pioneering and most studied LMCs is monolayer (ML) MoS₂^{6, 21, 81, 82}, which belongs to a subcategory called transition metal dichalcogenides (TMDC). A number of previous studies on bottom-up synthesized ML MoS₂ show similar morphologies: triangular or hexagonal shape flakes with lateral size tens of microns scattered on a substrate^{5, 7, 8}. The discontinuous character of such ML MoS₂ discourages many industrial applications. Continuous ML can be exfoliated from bulk MoS₂ crystal both mechanically¹¹ and electrochemically¹², but they usually have limited sizes. In contrast, wafer-scale continuous ML MoS₂ can now be grown by chemical vapor deposition (CVD)⁸³ or metalorganic CVD (MOCVD). A continuous ML TMDC grown on a single crystal substrate is formed through the coalescence of individual domains with certain orientations. However, such CVD growth process may introduce a variety of defects in ML TMDCs⁸⁴⁻⁸⁶ compared with the bulk TMDCs⁸⁷. A good understanding of the behavior of TMDCs at the interface is vital for improving the quality of CVD grown ML TMDCs.

In this chapter, I'll present some new findings from MOCVD grown continuous ML TMDCs, including MoS₂ and WS₂, on c-sapphire substrates. We used the novel technique, azimuthal reflection high-energy electron diffraction (ARHEED)^{1, 2, 9, 58}, which is good at detecting the long-range order in a ML compared to local probing techniques like TEM or STM, to map out the 3D reciprocal space structure of the MLs. Repeated experiments from better quality MoS₂ and WS₂ are also presented here.

Our findings include: (1) The gap between the MoS₂ and the sapphire surface, which is defined as the distance from bottom S atom in the ML MoS₂ to the top surface atomic layer of sapphire surface, is measured to be ~3 Å by RHEED. We found the sapphire surface was actually passivated with a layer of S atoms. This is supported by atomic force microscopy (AFM) line scan measurements, cross sectional TEM measurement and first principle density functional theory (DFT) calculations. The formation of this passivation layer has been understood from the DFT point of view and is believed to be a general case for TMDCs grown on sapphire substrate. (2) We constructed the 3D reciprocal space map of ML MoS₂/sapphire using ARHEED. Quantitative analysis of the 3D data shows that the half-width-at-half-maximum (HWHM) of the (00) diffraction is significantly broader than the instrument response along the direction parallel to the surface. Among the many factors contributing to the diffraction peak broadening such as point disorder⁸⁸, step atom density⁸⁹ and mosaic structure⁹⁰, we believe the incommensurate domains play the most important role, in particular, due to the characteristic coalescence process of randomly nucleated MoS₂ domains on the sapphire surface during MOCVD growth^{9, 83}. We studied the peak broadening using incommensurate domain model with both 1D analytical solution⁹¹ and 2D numerical simulation.

3.2 Results and Discussion

3.2.1 MoS₂-Sapphire Interface

Figures 3.1(a) and (b) show RHEED patterns of ML MoS₂ on sapphire captured at two azimuthal angles 30° apart with the zone axis (ZA) along the [2̄1̄10] direction and the [10̄10] direction, respectively. The straight through beam (S.T.) and shadowing edge (dashed line) are indicated on the RHEED patterns. The Miller indices (hk) of the diffraction stripes perpendicular to the shadowing edge are labeled. The scale bar has been calibrated previously by using a CdTe crystal with known lattice parameters⁶⁵. The axes of the coordinate system in the reciprocal space are denoted by two perpendicular arrows on the bottom-right corner of each RHEED pattern, where k_{\parallel} and k_{\perp} represent the momentum transfer parallel and perpendicular to the surface, respectively. Figures 3.1(c) and (d) are intensity profiles from RHEED patterns presented in Figs. 3.1(a) and (b) respectively. The scans are along k_{\parallel} at a fixed k_{\perp} of 5.1 Å⁻¹. A schematic is drawn on the top-right corner of each figure to illustrate the orientation of the line scan direction (the dashed line) relative to the reciprocal lattice (the red dots). The reciprocal space base vectors and zone axis are also labeled in the insets. The nine peaks in Fig. 3.1(c) can be fitted by nine Gaussian functions after a smooth Gaussian background subtraction. From the fitted peak positions one can calculate the average peak-to-peak spacing $\Delta k_{\parallel} = 2.30 \pm 0.07$ Å⁻¹. This is related to the real space lattice constant a of MoS₂ through the relation $\Delta k_{\parallel} = G(10) = 2\pi/(\sqrt{3}a/2)$. Therefore, the lattice constant can be determined to be $a = 4\pi/(\sqrt{3}\Delta k_{\parallel}) = 3.15 \pm 0.05$ Å, which is consistent with the bulk lattice constant of MoS₂ ($a = b = 3.1500$ Å, $c = 12.3000$ Å, ICDD reference code: 00-002-1133) within the experimental uncertainty. A similar analysis was performed for the intensity profile in Fig. 3.1(d) and the lattice constant is measured to be $a = 3.14 \pm 0.09$ Å. Upper curves of

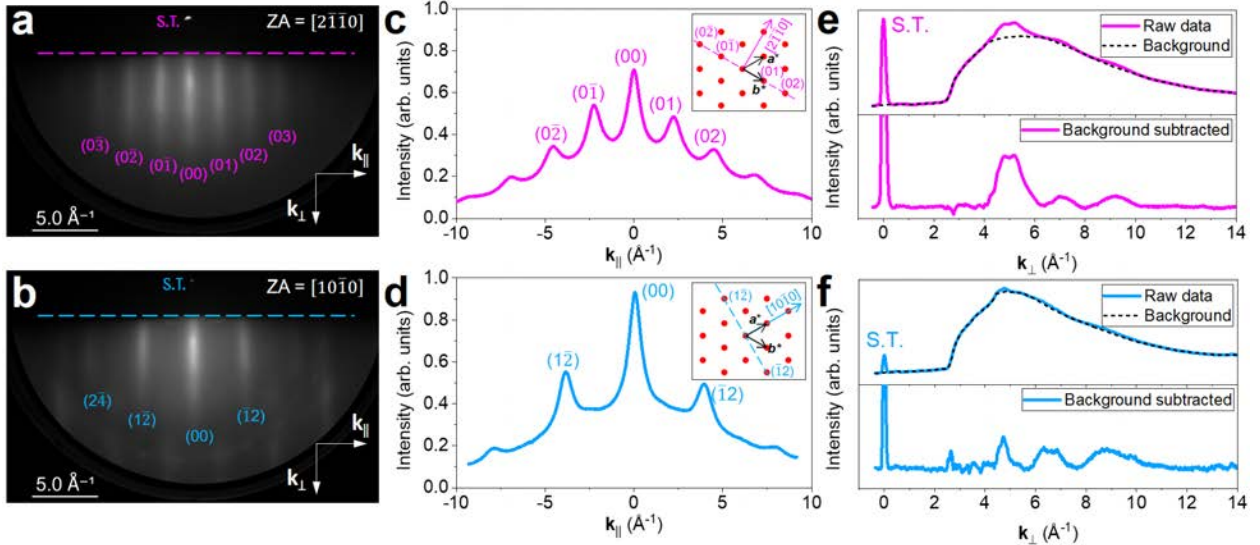


Figure 3.1: RHEED patterns along (a) $ZA = [2\bar{1}\bar{1}0]$ and (b) $ZA = [10\bar{1}0]$. The Miller index for each visible diffraction streak is labeled. The horizontal dashed line indicates the shadowing edge. The two arrows perpendicular to each other represents the k_{\parallel} and k_{\perp} directions. (c) and (d) Line profiles scanned along k_{\parallel} direction in the corresponding RHEED patterns shown in (a) and (b), respectively. The inset illustrates the scan direction (the dashed line) in the reciprocal lattice (the red dots) with base vectors a^* and b^* . The ZA direction is indicated with a long arrow with Miller index labeled. (e) and (f) Line profiles scanned along the k_{\perp} direction in the corresponding RHEED patterns shown in (a) and (b). The upper part of each figure shows the raw data (solid curve) and the smooth background (dashed curve) while the lower part shows the curve after the background subtraction.

the Figures 3.1(e) and (f) show the intensity profiles scanned along k_{\perp} direction from the central (00) stripe of the RHEED patterns shown in Figs. 3.1(a) and (b), respectively. In both cases, the intensities are not smoothly decaying as a function of k_{\perp} . The intensity modulation is caused by the vertical structure of the MoS₂/sapphire system. Similar like the above procedures to determine in-plane lattice constants, one can estimate the interlayer spacing d in the out-of-plane direction. The mild intensity bumps became obvious peaks in the bottom curves after the subtraction of the smooth backgrounds (the black dashed curves) in Figs. 3.1(e) and (f). This background is defined by connecting the diffraction intensity slightly to the outside of each “bump” ⁹², with a smoothly decaying trend. The average reciprocal space spacing between two adjacent peaks is $\Delta k_{\perp} = 2.08 \pm$

0.04 \AA^{-1} . Therefore, the interlayer spacing between ML MoS₂ and sapphire surface $d = 2\pi/\Delta k_{\perp} = 3.02 \pm 0.06 \text{ \AA}$.

The interpretation of this d value of $\sim 3 \text{ \AA}$ requires the knowledge about the details of the MoS₂-sapphire interface structure. For this reason, an aberration-corrected scanning transmission electron microscopy (STEM) at Penn State University has been utilized to image the cross section of this MoS₂-sapphire sample, which was prepared by focused ion beam (FIB) milling. Both high-angle annular dark field (HAADF) images with Z-contrast and conventional high-resolution transmission electron microscopy (HRTEM) bright field images with phase contrast were collected from this sample. Figures 3.2(a) and (c) show the cross-section views of HAADF-STEM and HRTEM images along the [1̄100] zone axis of sapphire from the MoS₂/sapphire interface, respectively, without any image processing. From Fig. 3.2(a) we found that there exists a buffer layer (indicated by the yellow arrow in Fig. 3.2(a)) between the top bright layer (indicated by the blue arrow in Fig. 3.2(a)) and the substrate at the bottom. Figures 3.2(b) and (d) shows the zoomed-in image from the region indicated by the yellow squares in Fig. 3.2(a) and (c), respectively, after applying a band-pass filter. They both clearly shows the existence of a buffer layer. From Figs. 3.2(b) and (d) we measured the gap between the MoS₂ and this buffer layer to be about 3 \AA . Later in this section we'll show that it was this gap that gave rise to the measured d from RHEED vertical line profile.

One immediate question one might ask is, what is the chemical composition and structure of this buffer layer? To figure out the chemical composition, we have measured energy-dispersive X-ray (EDX) mapping at the MoS₂-sapphire interface, as shown in Figs. 3.3(a-f). The EDX mapping is qualitatively consistent with our expectation: a MoS₂ layer on the top and the sapphire (Al₂O₃) substrate at the bottom. Due to the limited resolution, it is hard to make a definite

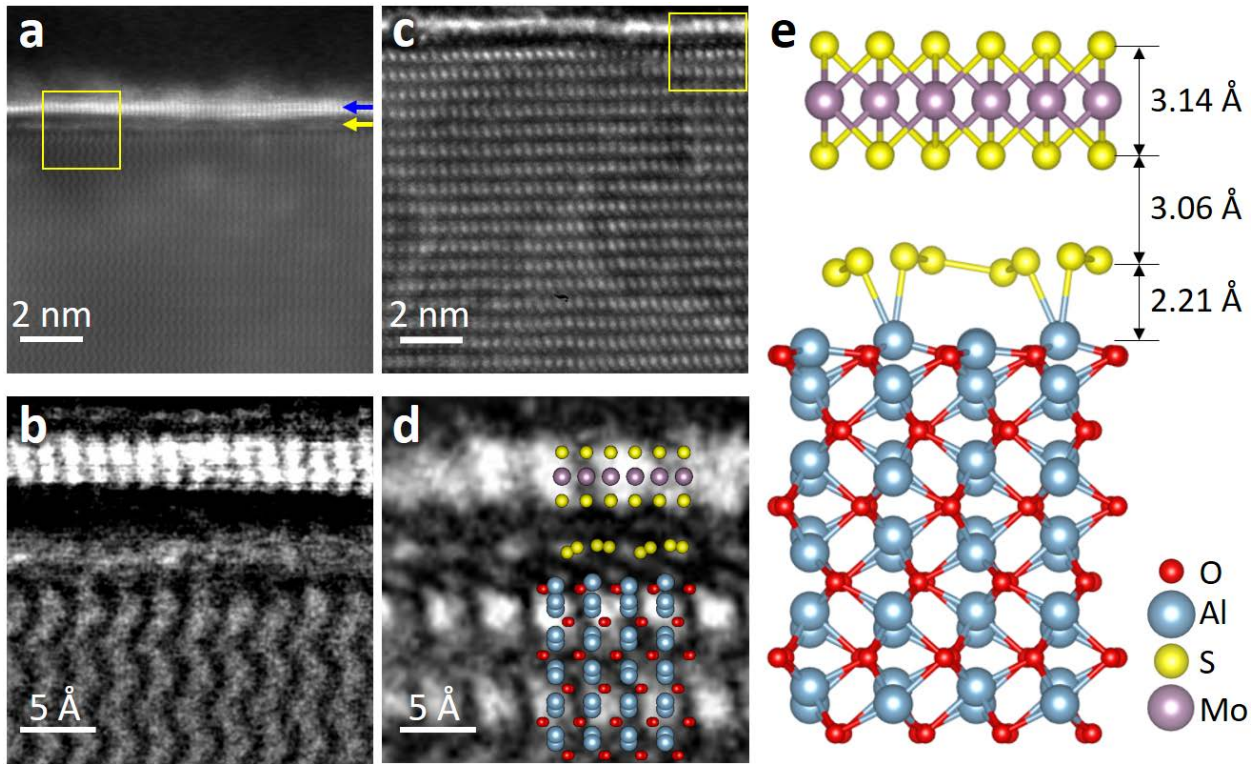


Figure 3.2: The cross-section views of (a) HAADF-STEM and (c) HRTEM images along the $[1\bar{1}00]$ zone axis of sapphire from the MoS₂/sapphire interface without any image processing. Zoomed-in view (b) HAADF-STEM and (d) HRTEM images from the yellow square denoted in (a) and (c), respectively. (e) The DFT calculated atomic structure of a ML MoS₂ on a S passivated sapphire. The vertical distances are labeled on this schematic. An atomic ball model of the structure in (e) has been superposed on (d) to demonstrate the close match between theory and experiment.

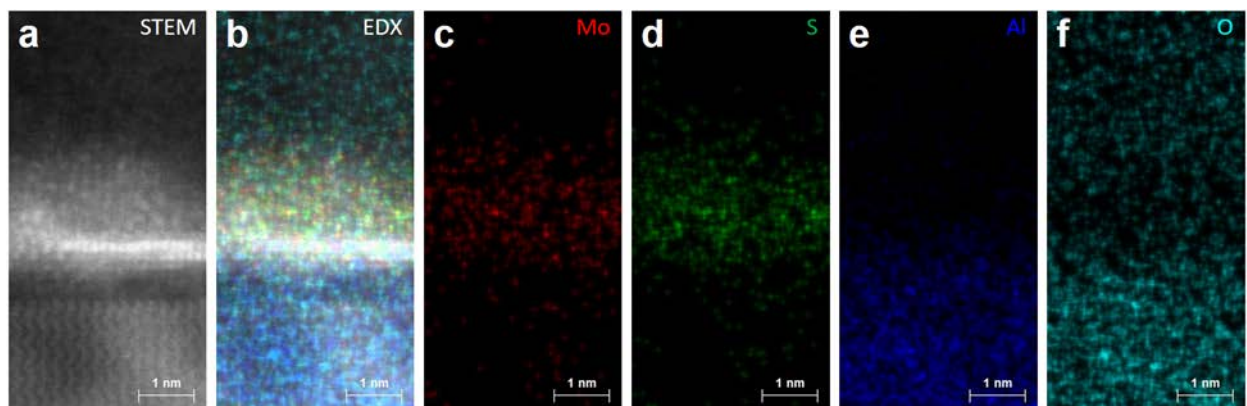


Figure 3.3: (a) HAADF-STEM image and (b) a combined EDX mapping from the MoS₂/sapphire interface. Individual EDX mapping from (c) Mo, (d) S, (e) Al and (f) O elements.

conclusion about the chemical composition of this buffer layer based on the EDX mapping. In literature, a similar interface structure for epitaxial WSe₂ grown on sapphire has been reported ⁸⁵. They claim that a Se passivation layer was formed at the interface to achieve stronger WSe₂-sapphire bonding. Since WSe₂ and MoS₂ have similar properties and they are both grown on sapphire substrate using MOCVD method, we hypothesize the buffer layer we observed in Fig. 3.2(a) is formed in a similar way as in their WSe₂/sapphire system consisting of the chalcogen atoms, or S atoms, in our case.

Next, in order to figure out the atomic structure of this buffer layer, my collaborator Dr. Gao has performed first-principles DFT calculations for a ML MoS₂ on Al-terminated sapphire with a S passivated layer. The MoS₂ layer was allowed to relax until the forces on all the relaxed atoms were less than 0.02 eV/Å. Figure 3.2(e) displays the calculated atomic structure for MoS₂ on S passivated sapphire surface viewed along the [1̄100] zone axis of c-sapphire. According to this calculated structure, the distance from the bottom of the MoS₂ ML to the S passivation layer is 3.06 Å, which strikes a close match with the value measured from the TEM images shown in Figs. 3.2(b) and (d). An atomic ball model of this structure is superposed on the HRTEM image in Fig. 3.2(d) to display the good match between theory and experiment.

This calculated interface structure by DFT is consistent with the measured *d* value of ~3 Å by RHEED. To check the consistency, I applied single scattering model and simulated the RHEED intensity profiles of the specular diffraction spot along the vertical momentum transfer direction using the DFT calculated structure shown in Fig. 3.2(e). Figure. 3.4(a) shows a series of simulated RHEED intensity of a specular spot along the k_{\perp} direction with various electron penetration depths ranging from 0 to 20 Å. The corresponding Fourier transforms of the profiles in Fig. 3.4(a) are shown in Fig. 3.4(b). Note that the horizontal axis of those Fourier spectrum is r_{\perp} , which is

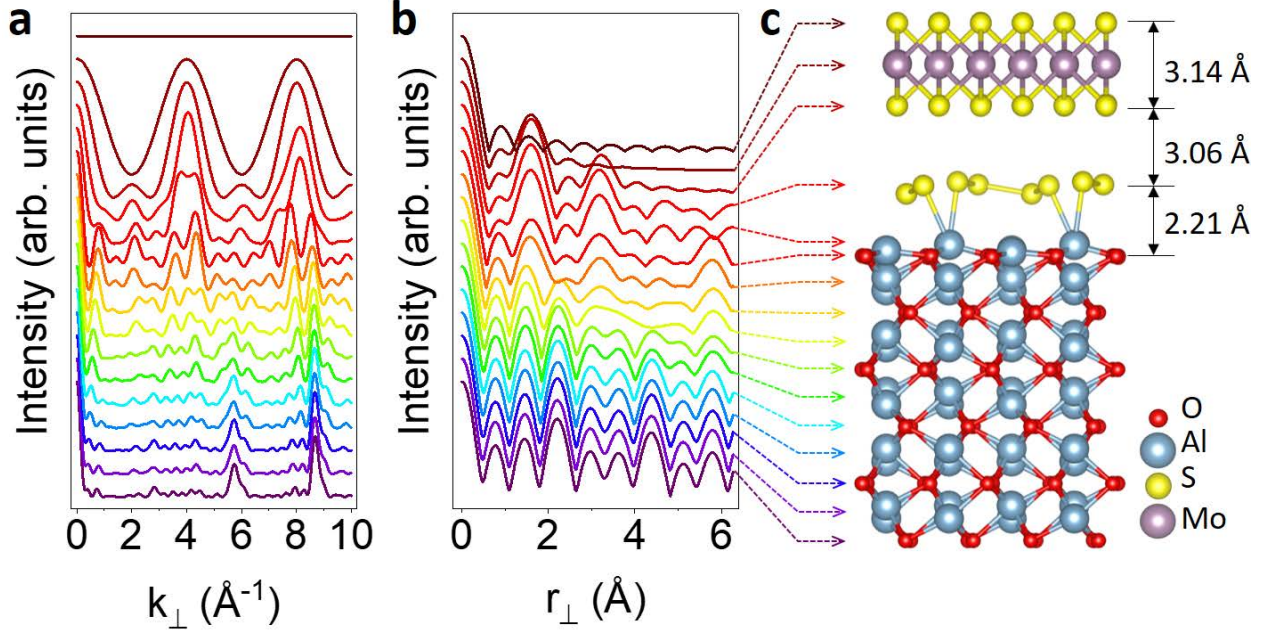


Figure 3.4: A series of simulated RHEED (a) intensity of specular diffraction spot and (b) the corresponding Fourier transform along k_{\perp} direction with various electron penetration depth.

(c) The DFT calculated atomic structure of a ML MoS₂ on a S passivated sapphire. The penetration depths are color coded and indicated by the dashed arrows connecting (b) and (c).

translated as the real-space periodicity that exists in the vertical direction of the DFT calculated structure shown in Fig. 3.4(c). The profiles in Figs. 3.4(a) and (b) are color coded with dark red color being the shallowest penetration and purple color being the deepest one. Their penetration positions are indicated by the dashed arrows connecting Fig. 3.4(b) and (c). From Fig 3.4(b) we see that the peak around $r_{\perp} = 3 \text{ \AA}$ starts to show up when the electrons reach the bottom S atoms of the ML MoS₂. It gets enhanced at the MoS₂-sapphire interface and gradually is washed out when the electrons penetrate deeper into the sapphire substrate. This result indicates that indeed the DFT calculated structure shown in Fig. 3.2(e) can cause a periodicity of $\sim 3 \text{ \AA}$ measured by a RHEED intensity oscillation in the vertical momentum transfer direction.

We have further verified the MoS₂-sapphire interface structure proposed above through AFM measurements. Figure 3.5(a) shows an AFM image from the same MoS₂ on sapphire sample that has been previously characterized by RHEED. An area with incomplete ML coverage has

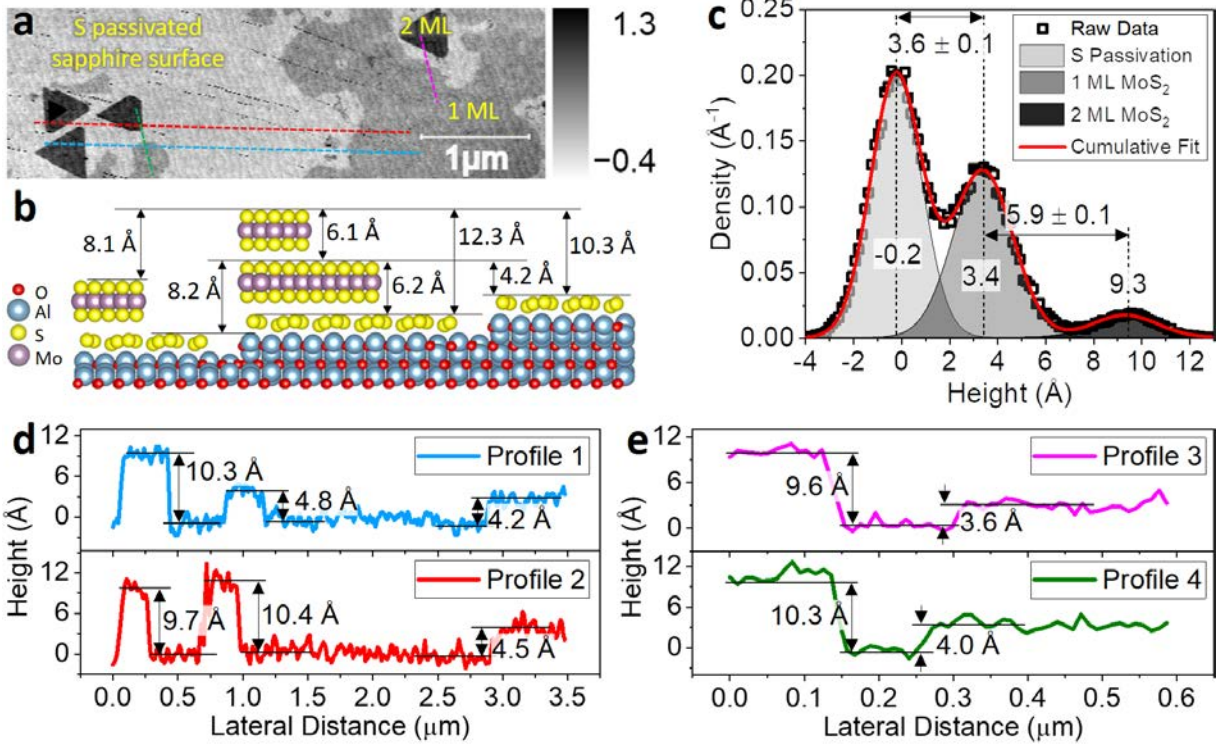


Figure 3.5: (a) The AFM image from the MoS₂/sapphire surface showing three distinct regions corresponding to the S passivated sapphire surface, 1 ML and 2 ML MoS₂. The four colored dashed lines indicate where the line profiles are extracted from. (b) An atomic ball model showing 1 ML MoS₂ and 2 ML MoS₂ on a stepped sapphire surface with a S passivation layer at the interface. Some typical vertical distances are labeled on the figure. (c) The height distribution of the AFM image shown in (a). (d) and (e) AFM line profiles scanned across MoS₂ islands and the sapphire terraces. The curves are plotted in four different colors in accordance with the colors used in (a).

been chosen for the height measurement in order to reveal the interface structure. This AFM image exhibits three distinct regions according to the gray scale tones: highlight, midtone and shadow. The highlight region shows terrace-step features similar to what's observed on a bare sapphire surface by others ⁹³⁻⁹⁵. The terrace-step feature can also be found in the midtone region, which implies that the island grows conformally on the low contrast area ⁹⁶. A few triangular shape islands composite the shadow region on the surface. Based on our learning of this sample from RHEED, TEM and DFT, we attribute the highlight, midtone and shadow regions to be the S passivated sapphire surface, 1 ML MoS₂ and 2 ML MoS₂, respectively, as denoted in Fig. 3.5(a).

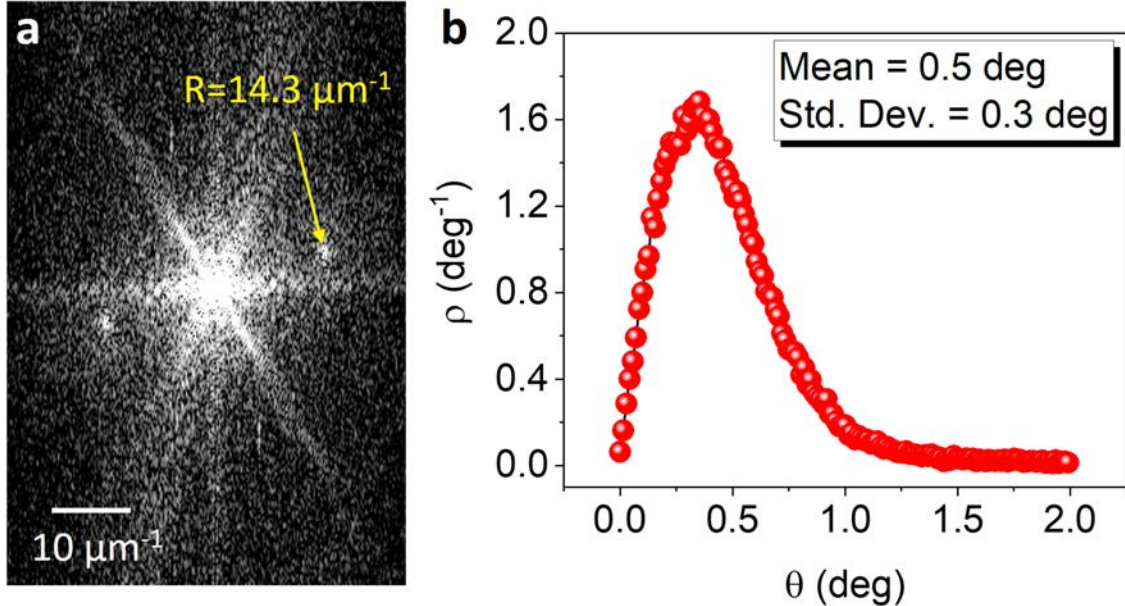


Figure 3.6: (a) The fast Fourier transform image of the AFM image shown in Fig. 3.5(a). Two bright spots show up at $R = 14.3 \mu\text{m}^{-1}$ from the center. Therefore, the corresponding real space periodicity is $L = 1/R \approx 70 \text{ nm}$, which corresponds to the average sapphire terrace width. (b) The slope distribution of the AFM image shown in Fig. 3.5(a), plotted as the probability density distribution ρ of the inclination angle from the horizontal plane.

In addition, we observed that the sapphire step edges are not monotonic but show step meandering, which is a result of the sapphire step roughening at the high annealing temperature $\sim 1000^\circ\text{C}$ during MOCVD growth, similar to the terrace-step morphology of sapphire reported previously⁹³⁻⁹⁵. Figure 3.6(a) shows the fast Fourier transform (FFT) of the AFM image shown in Fig. 3.5(a). The average terrace width of the sapphire was calculated from the peak position $14.3 \mu\text{m}^{-1}$ in Fig. 3.6(a) to be about 70 nm ($= 1/14.3 \mu\text{m}^{-1}$). By analyzing the slope distribution, as shown in Fig. 3.6(b), of the entire AFM image, we found that the average inclination angle from the horizontal plane is about 0.5° . Fig. 3.5(b) shows the atomic ball model representing 1 ML and 2 ML MoS₂ islands sitting on the S passivated sapphire surface with terraces. In this model, the distance from the bottom S atom in the ML MoS₂ to the S passivation layer is assumed to be 3 \AA based on the previous discussion. The sapphire lattice constants are $a = b = 4.7580 \text{ \AA}$, $c = 12.9910 \text{ \AA}$ (ICDD reference code: 00-010-0173). One step height of sapphire is $\sim 2 \text{ \AA}$ because one sapphire unit cell

has 6 such steps. According to this S passivation layer model, the smallest height difference one can measure is around 4 Å, which is from the 1 ML MoS₂ to the adjacent S passivated sapphire surface that is one sapphire terrace-step higher (~2 Å) than the terrace where the 1 ML MoS₂ island is located on. Other possible height differences include 6 Å, 8 Å, 10 Å, 12 Å, etc., are denoted in Fig. 3.5(b). Therefore, we can verify this model by measuring all possible height differences from AFM. Plotting the height distribution as the black square dots in Fig. 3.5(c), we observed three peaks, corresponding to the S passivation layer, the 1 ML and 2 ML MoS₂, respectively. The height distribution from a random rough surface is most generally described by a Gaussian function ⁹⁷:

$$p(h) = \frac{1}{\sqrt{2\pi}\omega} e^{\left(-\frac{(h-h_c)^2}{2\omega^2}\right)}, \quad (3.1)$$

where h_c is the peak center and ω is the root-mean-square (RMS) roughness. Therefore, we decomposed the height distribution into three parts by Gaussian peak fitting, which are shown in Fig. 3.5(c). The RMS roughness ω determined from Eq. (3.1) corresponding to the three regions are 1.6 ± 0.1 Å, 1.8 ± 0.1 Å and 1.9 ± 0.1 Å, respectively. The major contributions to this roughness are the sapphire terraces, whose step height is about 2 Å or 1/6 of the sapphire lattice constant c ^{93-95, 98}. The center position of these three peaks are -0.2 ± 0.1 Å, 3.4 ± 0.1 Å and 9.3 ± 0.1 Å, from which one can determine the average distance between the S passivation layer and 1 ML MoS₂ to be 3.6 ± 0.1 Å, and that between 1 ML MoS₂ and 2 ML MoS₂ to be 5.9 ± 0.1 Å. Combining them together, one gets the average distance between the S passivation layer and 2 ML MoS₂ to be 9.5 ± 0.1 Å. Figures. 3.5(d) and (e) show four individual AFM line profiles across and along the sapphire terraces, corresponding to the four colored dashed lines in Fig. 3.5(a). The measured height differences from the line profiles are labeled on Figs. 3.5(d) and (e). All those measured height differences indeed agree with the predictions of our model. We've also compared our results with the literature. The reported “thicknesses” of CVD grown ML MoS₂ on c-sapphire substrate

Table 3.1: Literature reported CVD grown ML MoS₂ to sapphire distances

Interface distance (Å)	6	6	6.4	6.5	6.8	7	7	8	8.4
Reference	99	8	100	101	83	8	102	103	104

measured by AFM were summarized in Table 3.1. The “thickness” ranges from 6 to 8.4 Å. In fact, the interface structure of MoS₂ on sapphire is rather complicated due to the formation of S passivation layer and the existence of sapphire terraces, just like what has been demonstrated schematically in Fig. 3.5(b). Therefore, the definition of “thickness” is open to interpretation. That’s probably one of the reasons why the literature reported values vary.

3.2.2 3D Reciprocal Space Map

Figure 3.7(a) shows a snapshot of the three-dimensional (3D) reciprocal space of the ML MoS₂/sapphire sample measured by ARHEED. The axes of the coordinate system are momentum transfers in x , y , z directions, or namely, k_x , k_y , k_z . It was constructed by stacking 2D reciprocal space maps¹ along the k_z direction. Figure 3.7(b) shows one such 2D reciprocal space map of ML MoS₂ at a fixed $k_z = 3.97 \text{ \AA}^{-1}$ plotted as the intensity contour map in the polar coordinate system. The radial axis represents the momentum transfer parallel to the surface ($k_{||}$) and the azimuthal angle φ ranges from 0 to 360°. Fig. 3.7(d) is the simulated 2D reciprocal space map viewed along the [0001] direction of MoS₂. The symmetry and spots locations in the simulation are consistent with the experimental 2D map shown in Fig. 3.7(b). Since the c-sapphire has (0001) out-of-plane orientation, obviously, the out-of-plane epitaxial relationship is $[0001]_{\text{MoS}_2} \parallel [0001]_{\text{sapphire}}$. For the in-plane epitaxial relationship, azimuthal scans from {11̄20} of MoS₂ and {11̄20} of sapphire were measured by glancing incident X-ray diffraction (GIXRD)¹⁰⁵, as shown in Fig. 3.7(c). The three peaks from each material match each other. This suggests a parallel in-plane

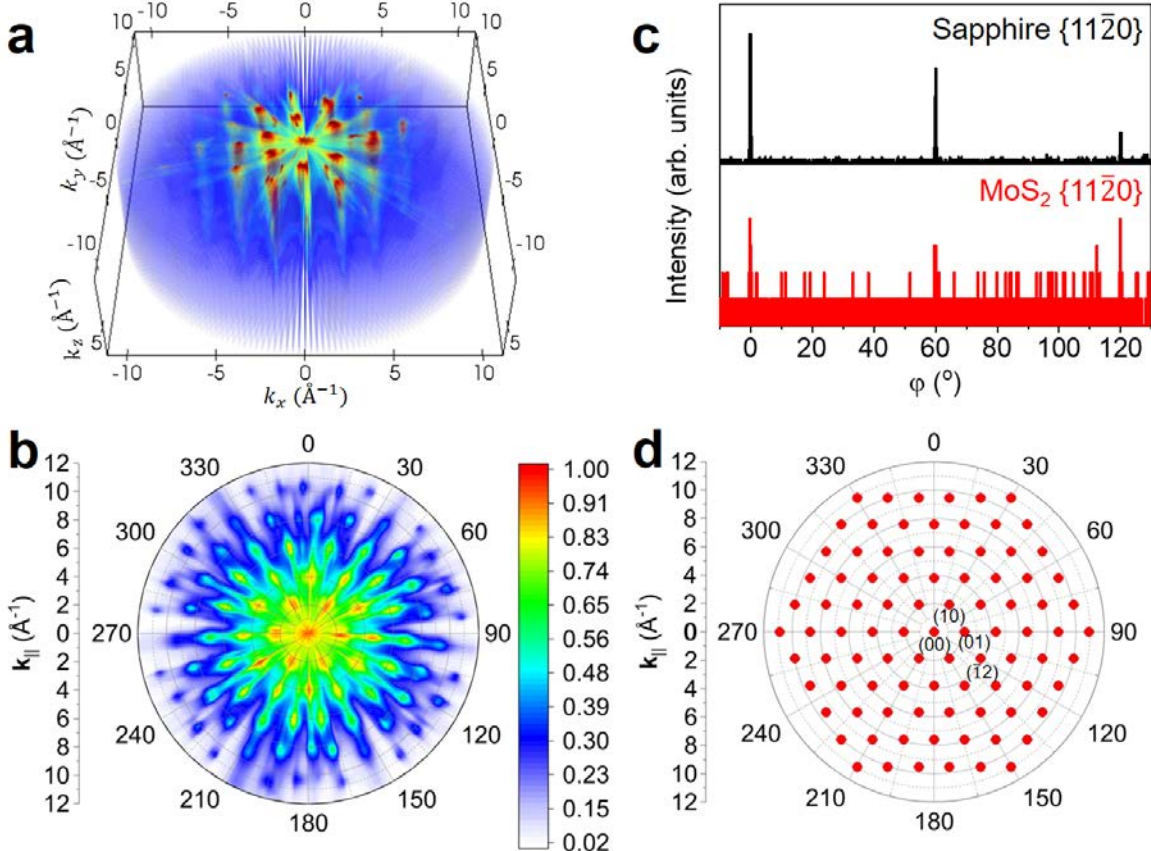


Figure 3.7: (a) A snapshot of the 3D reciprocal space map measured by ARHEED from MoS₂/sapphire. (b) Experimentally constructed ARHEED 2D reciprocal space map sliced from (a) at $k_z = 3.97 \text{ \AA}^{-1}$. The radial axis represents the momentum transfer parallel to the surface (k_{\parallel}) and the azimuthal angle ranges from 0° to 360° . (c) GIXRD azimuthal scans from sapphire $\{11\bar{2}0\}$ (upper) and MoS₂ sapphire $\{11\bar{2}0\}$ (lower). Their peaks line up, implying a parallel epitaxial relationship: $[11\bar{2}0]_{\text{MoS}_2} \parallel [11\bar{2}0]_{\text{sapphire}}$. (d) The theoretical simulation of the 2D reciprocal space map from MoS₂. Some low order Miller indices are labeled on (d).

epitaxy: $[11\bar{2}0]_{\text{MoS}_2} \parallel [11\bar{2}0]_{\text{sapphire}}$, despite the $\sim 34\%$ in-plane lattice constant mismatch

between MoS₂ and sapphire. We can understand this parallel epitaxy via GSAM simulation^{37, 38}.

The Al-terminated c-sapphire lattice parameters used in the GSAM model are $a_{\text{sapphire}} =$

$b_{\text{sapphire}} = 4.76 \text{ \AA}$, and $\theta_{\text{sapphire}} = 60.0^\circ$. The TMDC lattice parameters used in the model are

$a_{\text{MoS}_2} = b_{\text{MoS}_2} = 3.15 \text{ \AA}$, and $\theta_{\text{MoS}_2} = 60.0^\circ$. According to the GSAM simulation results, the

parallel epitaxy with 0° rotation angle (ϕ_R), along with rotational angles of 10.9° and 19.1° are

geometrically preferred. Figure 3.8(a) shows the superlattice area mismatch (ΔA) as a function of

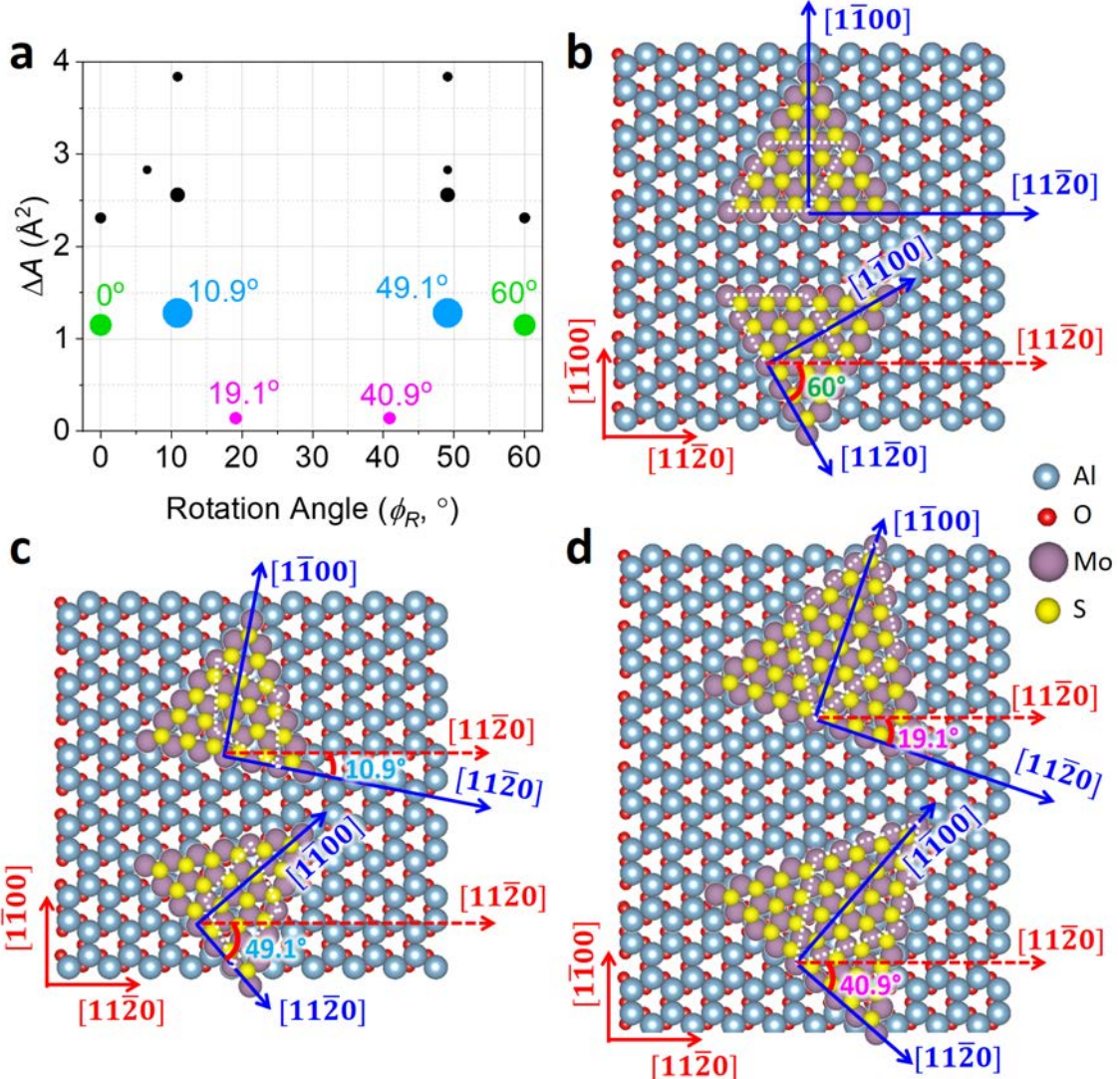


Figure 3.8: (a) A bubble plot of ΔA vs. ϕ_R resulting from the GSAM simulation of MoS₂ on c-sapphire. The range of ϕ_R is chosen from 0 to 60°, because both basal planes of TMDC and c-sapphire have a six-fold symmetry and thus the simulation result repeats itself every 60°. In the plot, the diameter of a bubble is inversely proportional to the area of superlattice A_1 (A_2). A small ΔA or a small area of superlattice (large bubble) means a high probability of observing a superlattice at the corresponding ϕ_R . The favorable ϕ_R values occur at 0°, 10.9°, 19.1°, 40.9°, 49.1°, and 60°. The atomic ball model of MoS₂ overlay on c-sapphire at (b) $\phi_R = 0^\circ$ and $\phi_R = 60^\circ$, (c) $\phi_R = 10.9^\circ$ and $\phi_R = 49.1^\circ$ and (d) $\phi_R = 19.1^\circ$ and $\phi_R = 40.9^\circ$. The MoS₂ domains aligned along these two ϕ_R are twin to each other. The yellow dashed parallelograms represent the superlattices formed under such conditions.

ϕ_R . Note that because both MoS₂ and sapphire c plane has a six-fold symmetry, the rotational angles of 0°, 10.9° and 19.1° are equivalent to 60°, 49.1° and 40.9°, respectively. Although the

superlattice area mismatch (ΔA) for $\phi_R = 19.1^\circ$ is smaller than $\phi_R = 0^\circ$, the parallel epitaxy is more energetically favorable according to Dumcenco *et al.*⁸, which agrees with our experimental observation. Figures 3.8(b), (c) and (d) show the atomic ball models of MoS₂ overlay on c-sapphire at $\phi_R = 0^\circ$, 10.9° and 19.1° , respectively.

One especially anomalous observation from this 3D map is the huge in-plane broadening of the reciprocal rods. The HWHM of the (00) spot at a fixed value of k_\perp along a certain azimuthal direction is determined by first subtracting the linear background, then finding out the two positions ($k_{\parallel 1}$, $k_{\parallel 2}$) that correspond to half-maximum intensity of the remaining profile and finally obtaining $HWHM = (k_{\parallel 1} - k_{\parallel 2})/2$. The process was repeated for all the k_\perp values and the azimuthal angles accessible in the 3D map. The red curve in Figure 3.9(a) shows a slice of the measured HWHMs of the (00) spot *vs.* azimuthal angle at a fixed $k_\perp = 3.97 \text{ \AA}^{-1}$ from the ML MoS₂/sapphire sample. The in-plane directions of MoS₂ was indicated by the two arrows in Fig. 3.9(a), which was determined from the 2D map shown in Fig. 3.7(b). The HWHMs from 180° to 360° are replicas of that from 0° to 180° due to the fact that the (00) spot is symmetric about the center and are therefore plotted as the dotted curve. The measured HWHMs range from $\sim 0.4 \text{ \AA}^{-1}$ to $\sim 0.6 \text{ \AA}^{-1}$, which is much larger than the instrument response function width (h_{inst}) of $\sim 0.1 \text{ \AA}^{-1}$ determined from the high-quality epitaxial graphene grown on copper substrate² as shown in Fig. 3.10(a) and (b). Similar broadening of the (00) spot were observed at other k_\perp values but is not presented here.

It is well known that various surface defects including point defects, step atoms and mosaic tilts could give rise to the diffraction peak broadening⁹⁰, as elaborated in the following: (1) Point defects. Random point defects itself will only increase the background intensity but not the broadening in the diffraction spots^{90, 106}. For vacancy complex, the nearby atoms may relax locally and the distance between atoms could contract⁸⁶. This produces microstrains which might account

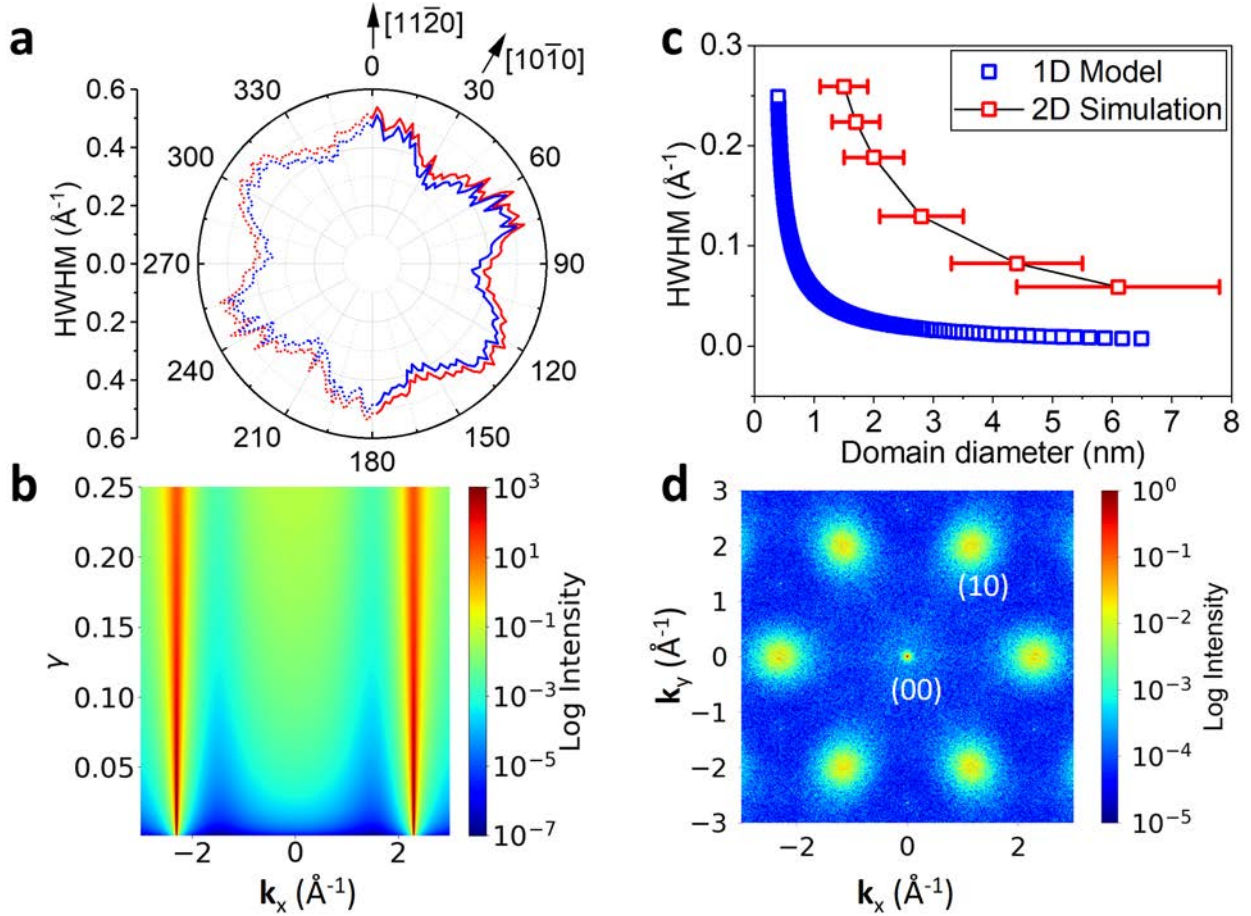


Figure 3.9: (a) A slice of the measured HWHMs of the (00) spot vs. azimuthal angle at a fixed $k_{\perp} = 3.97 \text{ \AA}^{-1}$ from the ML MoS₂/sapphire. The red and blue curves are before and after deconvolution with instrument response and the mosaic tilt induced broadening, respectively. The in-plane directions of MoS₂ were indicated by the two arrows in (a). The average HWHM before and after deconvolution are $0.46 \pm 0.05 \text{ \AA}^{-1}$ and $0.43 \pm 0.05 \text{ \AA}^{-1}$, respectively. (b) The intensity profile along the k_x direction for a series of γ values ranging from 0 to 0.25 calculated from the 1D incommensurate domain model. (c) The HWHM of the (10) spot as a function of the diameter of the incommensurate domain calculated from the 1D model (the blue squares) and the 2D model (the red squares). (d) The simulated 2D reciprocal space map from MoS₂/sapphire using the 2D model with nucleation density $\rho = 0.1$ or domain diameter $D = 2.0 \pm 0.5 \text{ nm}$. The (00) and (10) spots are labeled on the figure.

for part of the peak broadening. Our ML MoS₂ sample, however, has few defects as evidenced by the strong photoluminescence ⁸⁴ shown in Fig. 3.11(a) and the Raman spectrum that is free of LA(M) peak at $\sim 227 \text{ cm}^{-1}$ ¹⁰⁷ shown in Fig. 3.11(b). Therefore, the point defect induced broadening is ignored in this case. (2) Step density. The atomic scattering intensities from stepped surfaces has been studied by Spadacini *et al.*¹⁰⁸. According to their proposed theory, the HWHM of the

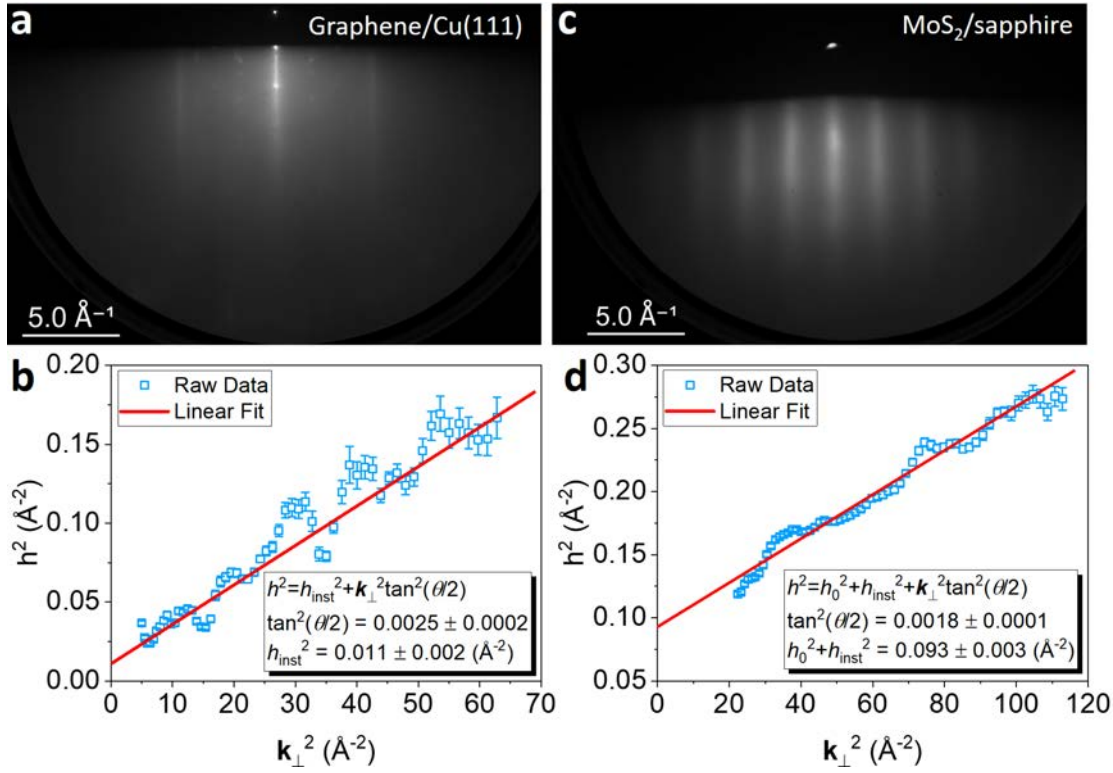


Figure 3.11: RHEED patterns taken from (a) epitaxial graphene/Cu(111) and (c) MoS₂/sapphire samples using 20 keV electrons. (b)(d) The square of half-width-at-half-maximum (h^2) plotted as a function of k_{\perp}^2 for the central diffraction streaks from (a) and (c), respectively. The instrument response is determined to be $h_{inst} = \sqrt{0.011 \pm 0.002}$ Å⁻¹ = 0.10 ± 0.01 Å⁻¹ from graphene/Cu(111) and the mosaic tilt induced broadening for MoS₂/sapphire is $|k_{\perp}| \tan(\theta/2) = 0.17$ Å⁻¹.

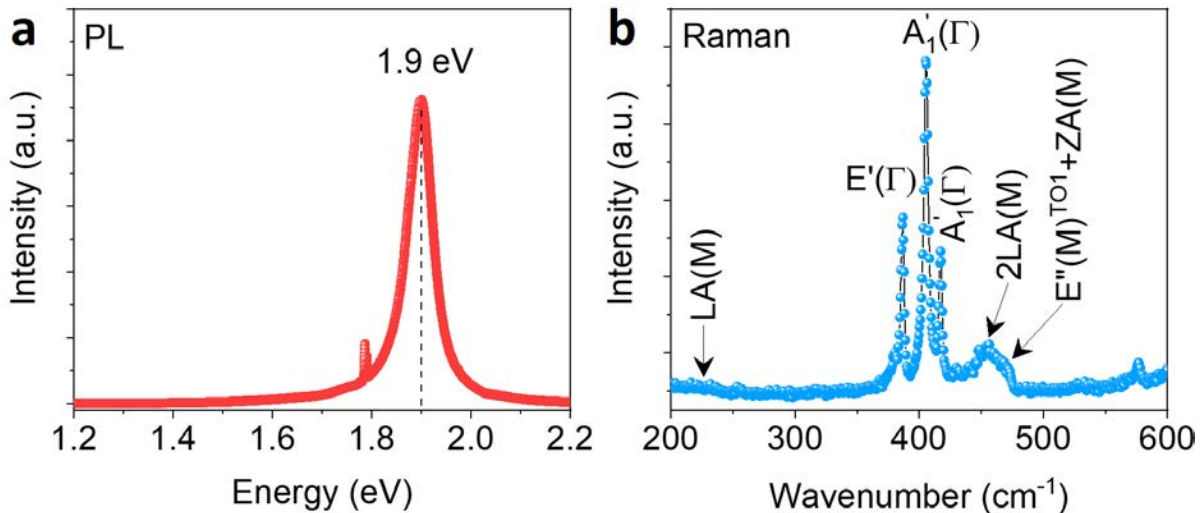


Figure 3.10: (a) Photoluminescence (PL) and (b) Raman spectrum from the MoS₂/sapphire sample. The strong PL peak at ~1.9 eV and the absence of LA(M) peak in Raman spectrum indicate that few point defects exist in the MoS₂.

diffraction spot increases linearly as a function of the step atom density (σ). Figures 3.12(a1-a6) show the simulated (00) spots using Spadacini's theory for the atomic scattering intensities from stepped surfaces with step atom densities $\sigma = 0.1, 0.2, 0.5, 1.0, 1.5$ and 2.0% , respectively. Figure 3.12(b) summarizes the relationship between the peak's HWHM and the step atom density from Figs. 3.12(a1-a6). In our case of MoS₂/sapphire, the step atom density can be estimated from the average terrace width of the sapphire surface to be $\sigma = 0.315 \text{ nm}/70 \text{ nm} \approx 0.5\%$. According to Fig. 3.12(b), those step atoms will result in $\sim 0.004 \text{ \AA}^{-1}$ broadening in the diffraction spots, which is negligible.

(3) Mosaic tilts. According to the previous AFM analysis in Fig. 3.6(b), the average inclination angle from the horizontal plane of MoS₂ is about 0.5° . However, this might underestimate the tilt angle since the AFM scans only very local regions. It is more meaningful to look at the statistical average of the mosaic tilt angle ($\theta/2$) across the surface. This can be done by plotting the square of HWHM (h^2) as a function of the k_\perp^2 using the data extracted from the 3D reciprocal space map, exactly the same way as how we determined the instrument response previously⁹²:

$$h^2 = h_0^2 + h_{inst}^2 + k_\perp^2 \tan^2 \left(\frac{\theta}{2} \right). \quad (3.2)$$

Therefore, both $\theta/2$ and the intrinsic broadening h_0 can be determined by doing a linear fit between h^2 and k_\perp^2 . Based on the analysis presented in Fig. 3.10(c), (d) for the MoS₂/sapphire sample, $\theta/2$ is found to be about 2.4° . Since Fig. 3.9(a) was measured at $k_\perp = 3.97 \text{ \AA}^{-1}$, therefore the contribution to the broadening from mosaic tilts is about $k_\perp \tan(\theta/2) = 0.17 \text{ \AA}^{-1}$.

The blue curve in Fig. 3.9(a) shows the HWHMs spot *vs.* azimuthal angle after deconvoluting all the contributing factors mentioned above. There's still a significant broadening of at least $\sim 0.3 \text{ \AA}^{-1}$. We believe it is mainly caused by the large amount of domain boundaries in

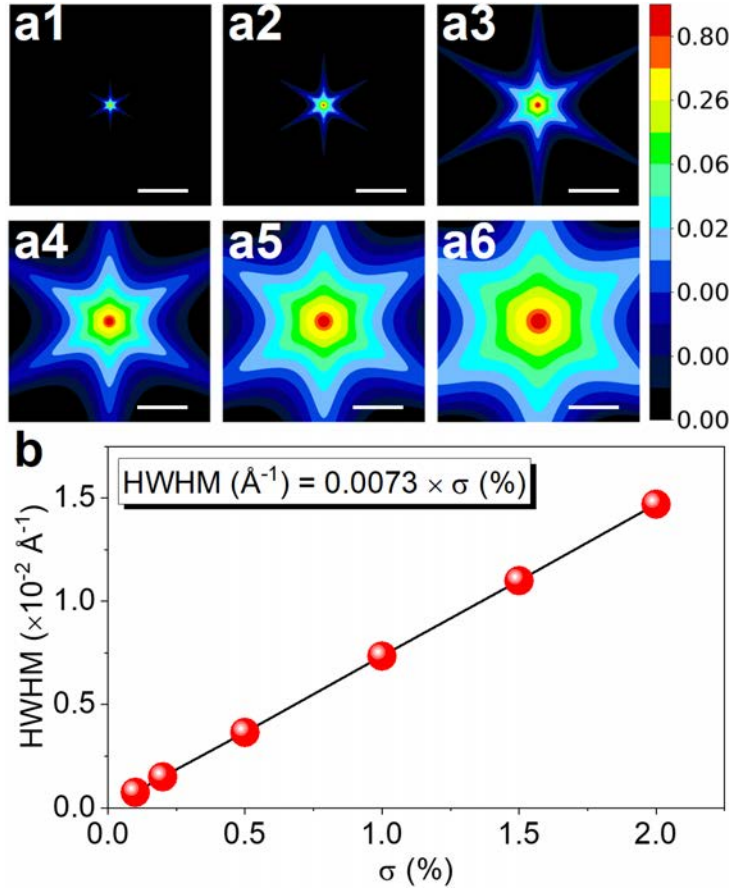


Figure 3.12: Simulated (00) spots using Spadacini's theory for the atomic scattering intensities from stepped surfaces with different step atom densities (σ): (a1) $\sigma = 0.1\%$, (a2) $\sigma = 0.2\%$, (a3) $\sigma = 0.5\%$, (a4) $\sigma = 1.0\%$, (a5) $\sigma = 1.5\%$ and (a6) $\sigma = 2.0\%$, respectively. The scale bar in each figure is 0.05 \AA^{-1} . (b) The relationship between the peak's HWHM and the step atom density summarized from (a1-a6).

the MoS₂ sample. Generally, for the CVD grown ML TMDC on sapphire, the initial nucleation centers distribute randomly on the sapphire surface sites. Because of the distinctly different lattice constants between the TMDC (3.15 Å) and sapphire (4.76 Å), when their sizes grow and meet, they form domain boundaries ^{9,85}. The dimension of such domains can be as small as only a few nanometers according to the STEM images from WSe₂ on sapphire reported in the literature ⁸⁵. If there's no rotation of domains involved in the CVD growth, which is indeed the case as we did not see noticeable peak splitting in the diffraction spots shown in Fig. 3.7(b), such type of boundaries can be described using a incommensurate domain model ⁹¹ (see more details in Appendix A).

Using this 1D incommensurate domain model, the 1D intensity profile covering $(\bar{1}0)$, (00) and (10) spots has been simulated for different γ value, which is the probability of finding a boundary between any two sites. The simulation result is presented in Fig. 3.9(b), showing the intensity profile along k_x for γ ranging from 0 to 0.25. The diffraction spot is delta function-like if there's no boundary at all ($\gamma = 0$) but becomes increasingly broader as the γ value goes higher. Since the diameter of a domain (D) is directly related to the γ value through $D = b/\gamma$, where $b = 3.15 \text{ \AA}$ is the lattice constant of MoS₂, the dependence of (10) spot's HWHM on the domain diameter is calculated and summarized as the blue open squares in Fig. 3.9(b). From this figure we found that the HWHM will be less than 0.05 \AA^{-1} if the domain size is larger than $\sim 1 \text{ nm}$, which apparently does not explain the huge broadening $\sim 0.4 \text{ \AA}^{-1}$. We attribute the failure of this 1D incommensurate domain model to be the oversimplification made in the analytical solution, including the assumptions that the domain size follows a geometric distribution and that domain boundaries along two base vectors are independent. Similar results have been obtained from the 2nd batch MoS₂/sapphire sample and the WS₂/sapphire sample, which are summarized in Fig. 3.13 and Fig. 3.14, respectively.

In order to overcome the limitation of this 1D model, we have developed a 2D incommensurate domain model with numerical simulation (see more details in the Appendix B). In this 2D model, we start from the random nucleation of the epilayer on the surface of the substrate lattice sites with a certain nucleation probability. The domains grow from these “seeds” and meet to form various boundaries. Assuming the growth of each domain is isotropic, the boundaries formed during the coalescence process are described using the Voronoi diagram ¹⁰⁹. In addition, we have required the distance between any two atoms be larger than the lattice constant of epilayer. Figures 3.15(a1)-(f1) show the simulated epilayer lattice sites with nucleation probabilities ranging

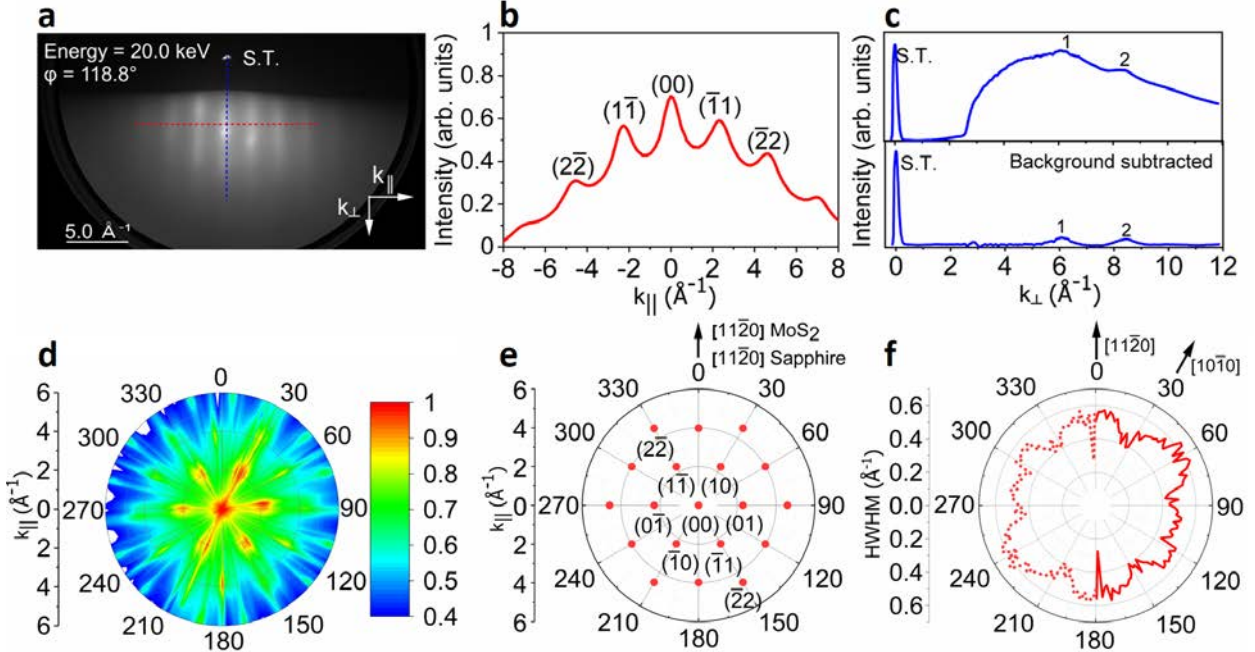


Figure 3.13: (a) A RHEED pattern of MoS₂ on sapphire substrate taken at azimuthal angle $\varphi = 118.8^\circ$. (b) The integrated intensity $I(k_{\parallel})$ along the red dashed line in (a) plotted in parallel momentum transfer k_{\parallel} direction. Peaks are labeled by Miller indices $(2\bar{2})$, $(1\bar{1})$, (00) , $(\bar{1}1)$, $(\bar{2}2)$. The average reciprocal separation Δk_{\parallel} of adjacent peaks is $2.27 \pm 0.06 \text{ \AA}^{-1}$. For hexagonal lattice: $|\vec{G}(hk)| = 4\pi/\sqrt{3}a \times \sqrt{h^2 + hk + k^2}$, where a is bulk in-plane lattice constant of MoS₂ = 3.1500 \AA . Theoretically, $|\vec{G}(\bar{1}1)| = 2.3 \text{ \AA}^{-1}$, which is in good agreement with our measurements of $2.27 \pm 0.06 \text{ \AA}^{-1}$. From the experimental value, the in-plane lattice constant of MoS₂ is determined to be $a = 3.19 \pm 0.06 \text{ \AA}$. (c) The integrated intensity $I(k_{\perp})$ along the blue dashed line in (a) plotted in perpendicular momentum transfer k_{\perp} direction. Peak at $k_{\perp} = 0$ is from straight through beam (S.T.). Two peaks (labeled 1 and 2) are result of constructive interference between MoS₂ monolayer and the substrate. The reciprocal space separation Δk_{\perp} of the two adjacent peaks is $2.36 \pm 0.04 \text{ \AA}^{-1}$ and the vertical distance between MoS₂ monolayer and the sapphire is determined to be $d = 2\pi/\Delta k_{\perp} = 2.66 \pm 0.06 \text{ \AA}$. (d) Experimentally constructed RHEED 2D reciprocal space map of MoS₂ monolayer plotted as the intensity $I(k_{\parallel}, \varphi)$ contour map in polar coordinate system. RHEED 2D reciprocal space structure exhibits a 6-fold symmetry and agrees with (e) the theoretical simulation viewed along the $[0001]$ direction of MoS₂, suggesting that the monolayer of MoS₂ is single crystal. (f) Experimentally measured half-width-at-half-maxima (HWHM) of the MoS₂ (00) in-phase diffraction spot in polar coordinate system. The radial and angular axes represent HWHM and the azimuthal angle φ , respectively. The (00) spot exhibits slightly broadening along $<11\bar{2}0>$ direction with a value of $\sim 0.6 \text{ \AA}^{-1}$ and the minimum broadening is $\sim 0.4 \text{ \AA}^{-1}$.

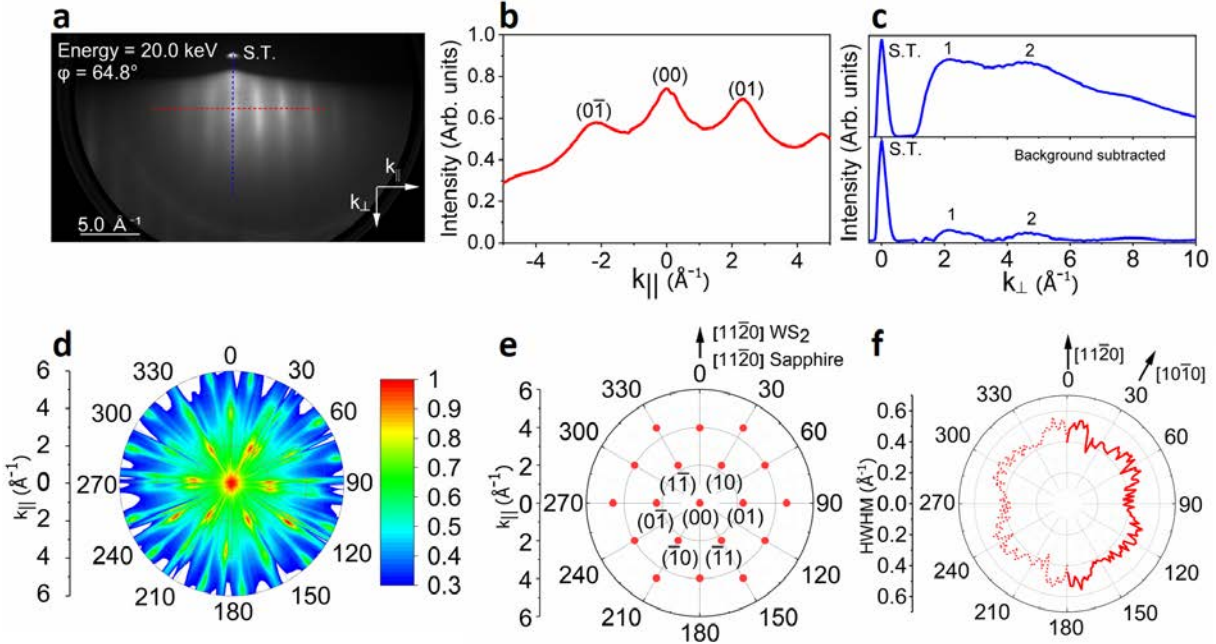


Figure 3.14: (a) A RHEED pattern of WS_2 on sapphire taken at azimuthal angle defined as $\varphi = 64.8^\circ$. (b) The integrated intensity $I(k_{\parallel})$ along the red dashed line in (a) plotted in parallel momentum transfer k_{\parallel} direction. Peaks are labeled by Miller indices $(0\bar{1})$, (00) and (01) . The average reciprocal separation Δk_{\parallel} of adjacent peaks is $2.17 \pm 0.07 \text{ \AA}^{-1}$. The bulk in-plane lattice constant of WS_2 is $a = 3.1532 \text{ \AA}$. Theoretically, $\Delta k_{\parallel} = |\vec{G}(01)| = 2.21 \text{ \AA}^{-1}$, which is in good agreement with our measurements of $2.17 \pm 0.07 \text{ \AA}^{-1}$. From the experimental value, the in-plane lattice constant of WS_2 is determined to be $a = 3.34 \pm 0.07 \text{ \AA}$. (c) The integrated intensity $I(k_{\perp})$ along the blue dashed line in (a) plotted in perpendicular momentum transfer k_{\perp} direction. Peak at $k_{\perp} = 0$ is from straight through beam. Two peaks (labeled 1 and 2) are result of constructive interference between WS_2 monolayer and the substrate. The reciprocal separation Δk_{\perp} of the two adjacent peaks is $2.29 \pm 0.04 \text{ \AA}^{-1}$ and the vertical distance between WS_2 monolayer and the sapphire is determined to be $d = 2\pi/\Delta k_{\perp} = 2.74 \pm 0.05 \text{ \AA}$. (d) Experimentally constructed RHEED 2D reciprocal space map of WS_2 monolayer plotted as the intensity $I(k_{\parallel}, \varphi)$ contour map in polar coordinate system. RHEED 2D reciprocal space structure exhibits a 6-fold symmetry and agrees with (e) the theoretical simulation viewed along the $[0001]$ direction of WS_2 , suggesting that the monolayer of WS_2 is single crystal. (f) Experimentally measured HWHMs of the WS_2 (00) in-phase diffraction spot in polar coordinate system. The radial and angular axes represent HWHM and the azimuthal angle φ , respectively. The (00) spot exhibits slight broadening along the $<11\bar{2}0>$ direction with a HWHM value of $\sim 0.5 \text{ \AA}^{-1}$ and the minimum broadening is $\sim 0.4 \text{ \AA}^{-1}$.

from 0.01 to 0.2. Figs. 3.15(a2)-(f2) are the corresponding zoomed-in views while the histograms in Figs. 3.15(a3)-(f3) show the domain size distributions. For higher nucleation probability, the average domain diameter became smaller. From those simulated lattices, we have calculated diffraction patterns using the kinematic scattering approach⁵⁶, which are shown in Figs. 3.15(a4)-(f4). Obviously, the peaks are broader for higher nucleation probability. To be more quantitative, we have determined the HWHM of the (10) spot from each simulated diffraction pattern by fitting with a 2D Gaussian distribution, as shown in Figs. 3.15(a5)-(f5). Finally, the dependence of HWHM on the average domain diameter is summarized and plotted as the red open squares in Fig. 3.9(c) in order to compare with the 1D model. From Fig. 3.9(c) we can see that the HWHM decreases as the domain diameter increases, following the same trend as the 1D model but the magnitude is several times higher. Assuming the average domain size in the ML MoS₂ sample to be \sim 2 nm, the corresponding broadening in HWHM is \sim 0.15 Å⁻¹. The simulated 2D reciprocal space intensity under this condition is shown in Fig. 3.9(d).

3.3 Conclusion

The 3D reciprocal space mapping using ARHEED has provided rich structural information about ML TMDCS on sapphire substrates. The in-plane lattice constant of ML TMDCs and its epitaxial relationship with sapphire are determined experimentally as well as the out-of-plane interlayer spacing between TMDC and sapphire. From RHEED and TEM we have confirmed the existence of a S passivation layer at the MoS₂-sapphire interface. This is supported by AFM measurements and DFT calculations. According to the DFT results, the formation of this S passivation layer is more energetically favorable and is necessary for the van der Waals epitaxy. That the observed broadenings of diffraction spots are larger than the instrument response width indicates extended defects exist in wafer scale ML TMDCs. Part of the spot broadening in the

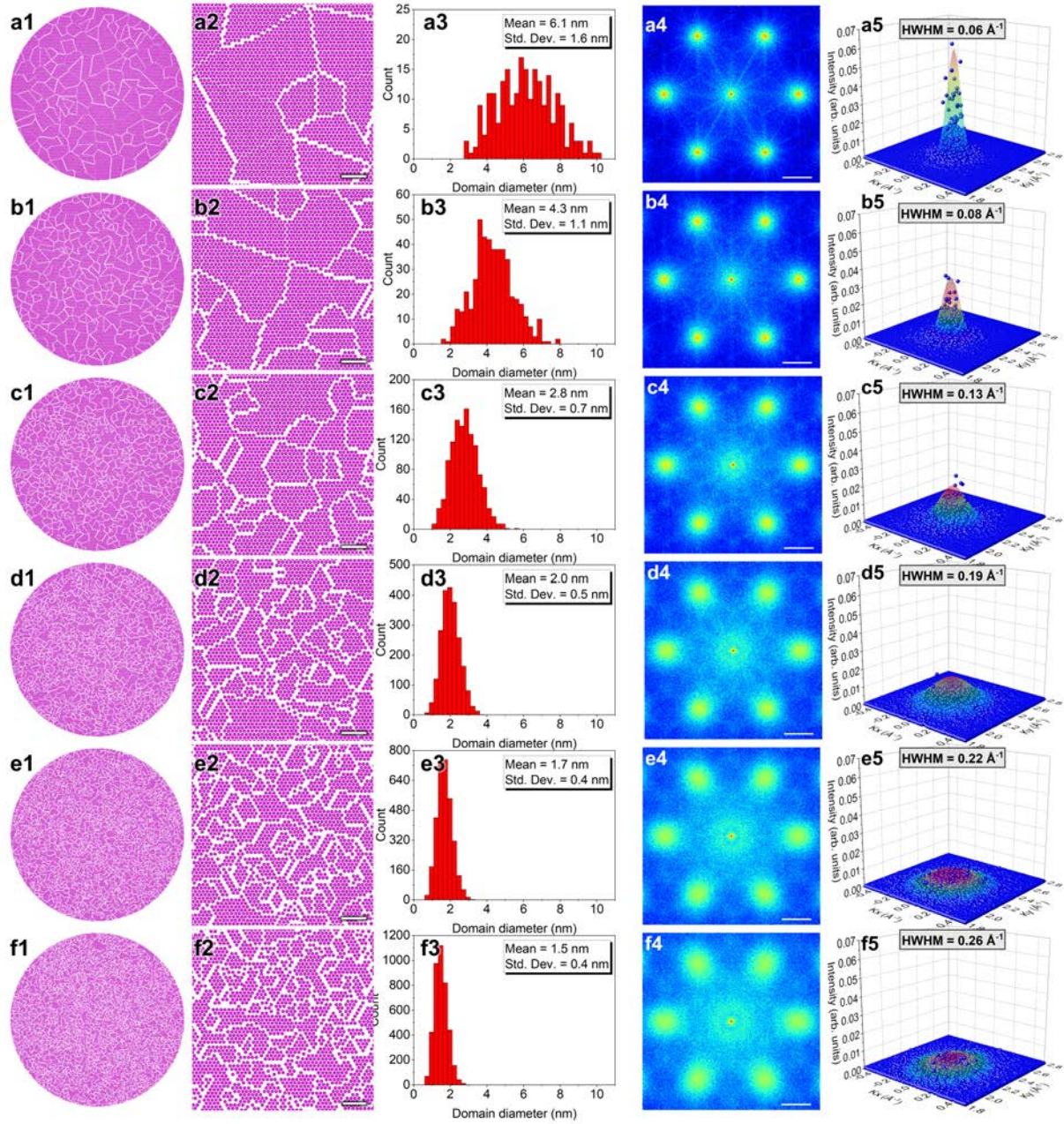


Figure 3.15: (a1-f1) The generated circular-shape epilayer lattices of diameter $D = 70$ nm, (a2-f2) the 5×5 zoom-in views of the corresponding lattices, (a3-f3) the size distributions, (a4-f4) simulated 2D reciprocal space intensities $I(k_x, k_y, k_z = 0)$ and (a5-f5) the simulated 2D intensities around (10) spot (the scattered points) and their Gaussian surface fit (blue at low intensity and red at high intensity) from the numerical simulations using nucleation density $\rho = 0.01, 0.02, 0.05, 0.10, 0.15$ and 0.20 , respectively. The scale bars in (a2-f2) are all of 2 nm. The mean and standard deviation of the sized distributions are labeled on each of the (a3-f3) figures, showing a descending trend as ρ becomes larger. The scale bars in (a4-f4) are all of 1 Å⁻¹. The HWHMs are determined for the (10) spots by Gaussian fit and labeled on the top each of (a5-f5).

RHEED patterns can be simulated by a 2D diffraction model with domain boundaries that are generated by the incommensurate MoS₂ layer on sapphire substrate. These domain boundaries were observed by real space imaging techniques (TEM and STEM) and were reported in the literatures. We demonstrated that ARHEED is sensitive to ML coverage and can provides wafer scale structural information through the measurement of the 3D reciprocal space map.

4. HRLEED CHARACTERIZATION OF EPITAXIAL GRAPHENE ON COPPER(111)

4.1 Introduction

Although subjected to severe charging effect when a non-conductive substrate is used, HRLEED is still one of the most direct and quantitative way to detect the symmetry and perfection of various 2D materials such as graphene^{110, 111}, hexagonal boron nitride (h-BN)¹¹² and monolayer MoS₂¹¹³. In HRLEED, electrons are typically incident normally onto the surface of graphene and the reflected diffraction pattern would reveal the symmetry and perfection of the 2D lattice. The diffraction pattern is close (not exactly) to represent the 2D reciprocal space lattice structure. Therefore, from HRLEED one can get the 2D reciprocal space map in just one shot, compared to the time-consuming data acquisition and analysis process using ARHEED. In addition, HRLEED is significantly better than ARHEED in terms of the spatial resolution, angular resolution and dynamical range¹¹⁴. Table 4.1 is a comparison between ARHEED and HRLEED.

Table 4.1: A comparison between ARHEED and HRLEED

	ARHEED	HRLEED
Primary Electron Energy	10 - 30 keV	50 - 300 eV
Incident Angle	~1°	~90°
Dynamic Effect	Strong	Weak
Charging Effect	Weak	Strong
Working Pressure	~10 ⁻⁷ torr	~10 ⁻¹⁰ torr
Spot Diameter	~1 mm	~100 μm
Spatial Resolution	~0.1 Å	~0.03 Å
Angular Resolution	1.8°	~0.006°
Dynamical Range	10 ²	10 ⁶

In this chapter, I'll present the HRLEED study of epitaxial graphene as-grown on Cu(111) on spinel(111) substrate. While the ARHEED results of this sample from Chapter 2 might contain the mixed signal from both graphene and Cu(111) due to the shallow but non-neglectable electron penetration depth, we were able to clearly resolve the diffraction peaks from copper and that from graphene in HRLEED by analyzing the profiles of (01) diffraction spot.

4.2 Experimental

4.2.1 Sample Holder Design

A customized sample holder has been made for the HRLEED system with three major requirements: (1) hold the sample with various size (10 mm - 15 mm) in the vertical direction. (2) heat the sample up to about 1200 °C in a short time. (3) be float-grounded and maintain electrically isolated from other parts of the sample holder.

Those requirements can be properly addressed in the following way: (1) the sample is clamped with two tantalum strips. One of the strips has two circular holes at two ends, allowing it to be fixed by the bolts and nuts. The other strip has two stadium-shape holes, which can not only be fixed by the bolts and nuts but also move along the hole within a ~5 mm range once the nuts are loosened. This design offers the flexibility to accommodate samples with various sizes. (2) The requirement for the capability of heating up to 1200 °C is imposed by the cleaning process of a Si(111) surface ¹¹⁵, which is used as the standard sample to calibrate the HRLEED system. There are several different kinds of methods to heat up the sample in vacuum, including direct current heating, radiative heating and electron bombardment heating ¹¹⁶. A combination of radiative heating and electron bombardment heating was utilized in the sample holder design, since it does not depend on the electrical resistance of the sample and provides excellent control over the temperature. A homemade “pancake” filament, which was made from tungsten wire of diameter

0.01 inch, was used to radiatively heat the sample and to emit hot electrons. With radiative heating alone, the sample can be heated up to ~ 250 °C. In order to accelerate the hot electrons to bombard on the sample, the filament was negatively biased to a high potential while the sample was connected to the floating ground of the high voltage power supply. Combining both radiation heating and electron bombardment heating together, the sample temperature can be raised up to ~ 1500 °C in a few seconds. (3) Since the energy of electrons used in HRLEED is only tens of eV, the electrons are very sensitive to the surface charge. Therefore, accumulated charge must be drained through a grounding wire during the experiment. In the meanwhile, the sample should be electrically isolated from the filament in order to avoid short circuit. It must be isolated from the sample holder housing as well because otherwise the electrons will be drawn to both the sample and the housing, causing a waste of power and an excessive outgassing. Those issues can be solved by putting the sample on a metal shield that is isolated from the housing using ceramic washers and screws. This metal shield is made from low-outgassing Ta plate, leaving a square-hole in the center to allow electrons passing through. Another merit of using this shield is that the strong light emitted by the filament can be blocked to avoid an interference with the pyrometer for temperature measurements.

Schematics of this sample holder design are presented in Figs. 4.1(a)-(f). All parts are UHV-compatible and non-magnetic.

4.2.2 Calibration

Due to the electrical deflection of electrons using the octupoles, the spots in an electron diffraction pattern have minute deviations from their theoretical positions near the edges of a diffraction pattern. The Si(111) (7 \times 7) reconstruction has many diffraction spots over the entire diffraction pattern and is an ideal system to calibrate the deviation of spots from theoretical

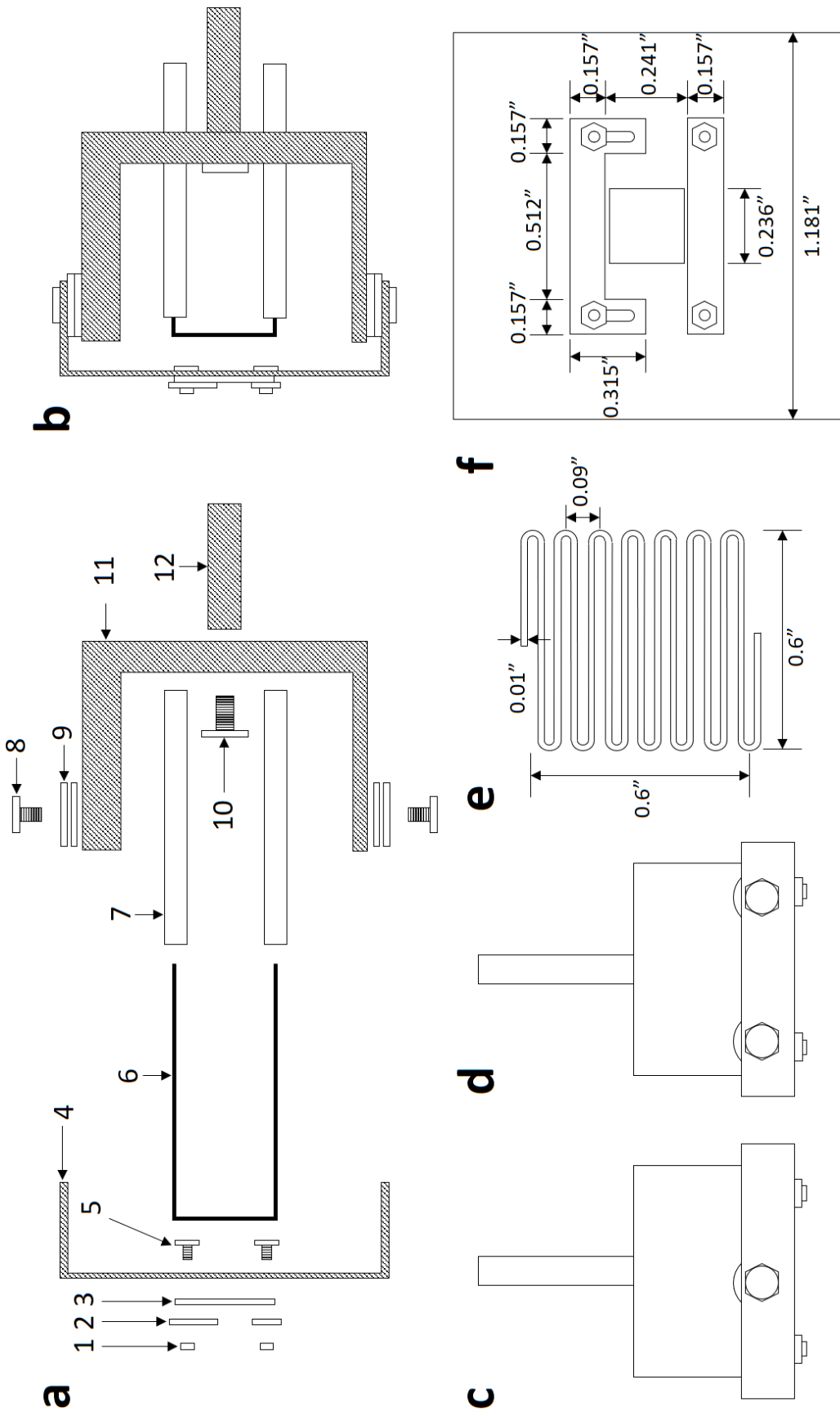


Figure 4.1: (a) Schematics of the disassembled parts of the sample holder: 1. Stainless steel nuts, 2. Tantalum strips, 3. Sample, 4. Tantalum shield, 5. Stainless steel bolts, 6. Tungsten filament, 7. Ceramic tubes, 8. Ceramic bolts, 9. Ceramic washers, 10. Stainless steel bolt, 11. Stainless steel sample housing, 12. Stainless steel shaft. (b) Schematic of the assembled sample holder. (c) Top-view and (d) bottom-view of the sample holder. (e) Schematic of the “pancake” tungsten filament with dimensions written. (f) Front view of the sample housing shield and two tantalum strips with dimensions labeled.

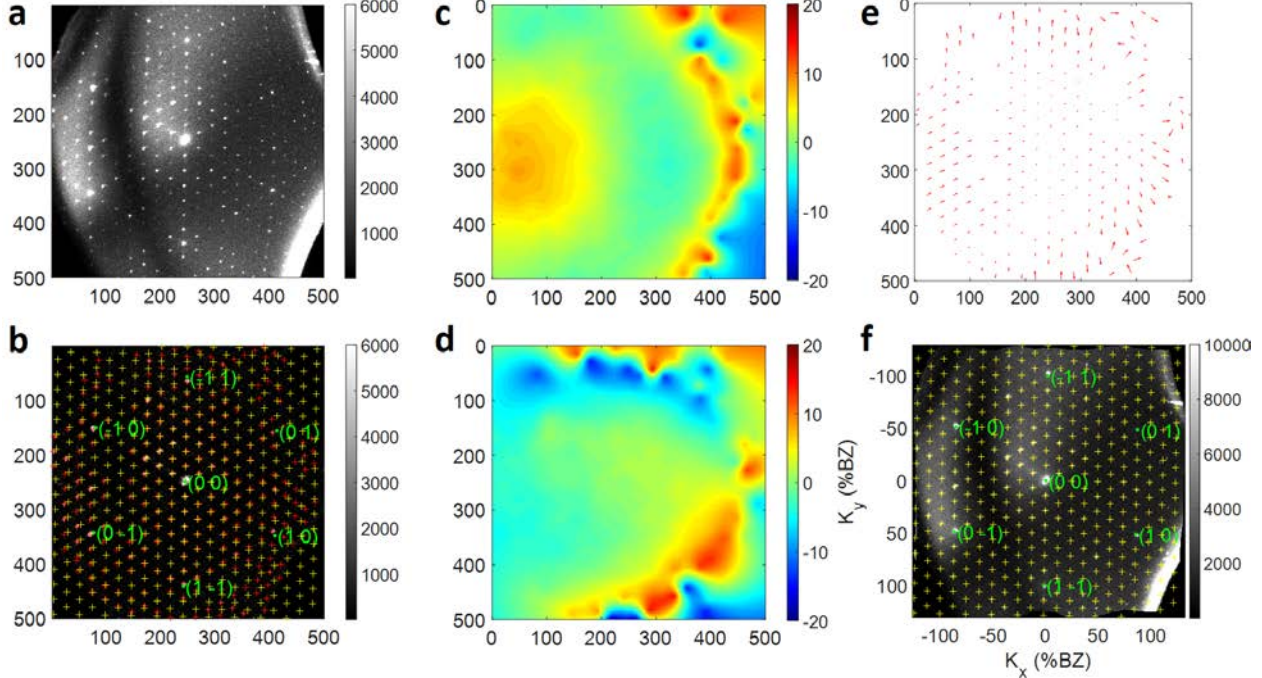


Figure 4.2: (a) Room temperature experimental HRLEED pattern of Si(111) (7×7) reconstruction taken at an incident energy of 126.5 eV. (b) HRLEED pattern after the subtraction of background intensity. The red crosses are positions of experimental spots in (a) and the yellow crosses are theoretical peak positions. Deviations between red and yellow crosses in the (c) x and (d) y directions, respectively. (e) A map of the discrete deviation vector field. The units of the k_x (horizontal) and k_y (vertical) axes are in units of pixels. (f) HRLEED pattern after the correction of the experimental spots using the deviation field. The experimental spot positions and theoretical spot positions are coincident. The units of the k_x and k_y axes are in percentages of Brillouin zone (%BZ).

positions. The Si(111) (7×7) reconstruction was observed in the viewing mode after *in situ* thermal flashing to ~ 1200 °C. The angular profiles of the (00) diffraction spot was measured every other 2 volts from 65 to 200 eV. The high intensity that corresponds to the in-phase condition is within 2 to 3 V from the kinematic in-phase condition. The Si(111) (7×7) reconstruction pattern taken at 126.5 eV is shown in units of pixels in Fig. 4.2(a). The background in the pattern is not uniform and the brightest arc near the bottom right of the pattern is due to the octupole effect. The background was first subtracted from the diffraction pattern and the diffraction spots were picked and indexed using the home-developed MATLAB program as shown in Fig. 4.2(b). The red crosses mark the experimental positions while the yellow crosses indicate where they should be

theoretically. The red and yellow diffraction spots near the center (00) spot overlap. However, the spots farther away from the center (00) spot do not overlap. The deviations between theoretical diffraction spot position vectors $\vec{R}(i,j)_{\text{theory}}$ and experimental diffraction spot position vectors $\vec{R}(i,j)_{\text{experiment}}$ for all spots are mapped as discrete deviation vectors $\vec{D}(i,j) = \vec{R}(i,j)_{\text{theory}} - \vec{R}(i,j)_{\text{experiment}}$ in Fig. 4.2(c) where the magnitude of each vector is the difference between the experimental position and theoretical position and the direction is pointing from the experimental position to the theoretical position. Since the map of deviation vectors in Fig. 4.2(c) is not continuous, the continuous deviations in the x and y directions are approximated as component $D_x(i,j)$ and component $D_y(i,j)$ in Figs. 4.2(d) and 4.2(e), respectively, using a radial-basis-function of multi-quadratic type. The value indicated by the color bar on each pixel represents the deviation of the experimental position from the theoretical position in that direction. In order to convert pixels to percentages of Brillouin zone in reciprocal space, the sensitivity factor was determined to be 3.21 ± 0.01 VÅ, by minimizing the difference between experimental spot and theoretical diffraction spot positions. Figure 4.2(f) shows the corrected HRLEED pattern in units of percentage Brillouin zone (%BZ).

4.2.3 Instrument Response

The measured FWHM and transfer width¹¹⁷ from the Si(111) surface was used as the instrument response for the HRLEED system. The Si(111) surface has a hexagonal lattice with the lattice constant $a = 3.84$ Å. A HRLEED line scan along the [10̄10] direction of this hexagonal lattice was collected at 126.5 eV. The black curve in Fig. 4.3 shows the line scan profile after distortion correction and background removal. The Miller indices of peaks from the primary Si(111) lattice are labeled in blue color. Other peaks are due to the (7×7) super lattice of surface reconstruction. Each peak has been fitted with a pseudo-voigt function, shown as the colored curve

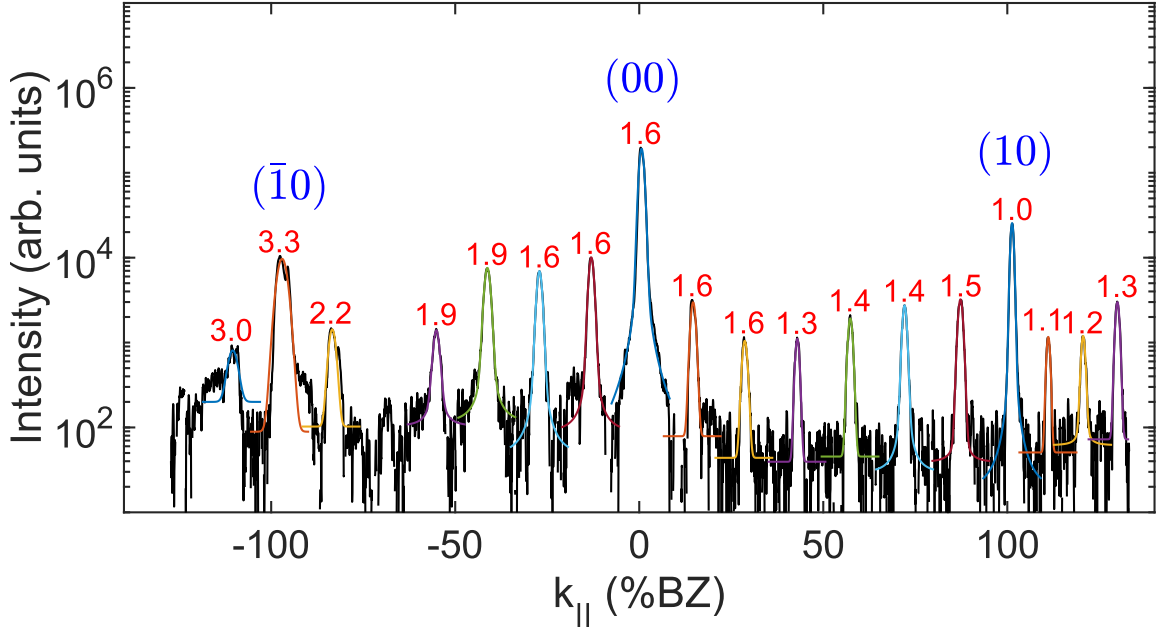


Figure 4.3: HRLEED line scan from the Si(111) surface collected at 126.5 eV along the $[10\bar{1}0]$ direction. The black curve shows the profile after the distortion correction and background removal. The blue labels are the primary Miller indices from the Si(111) hexagonal lattice. The colored curves are the fitted pseudo-voigt profile for each peak. The red labels are the FWHMs of each peak in the unit of %BZ.

superposed on the original data in Fig. 4.3. The FWHMs from the fitting are labeled in red color on top of each peak in the unit of %BZ. The average FWHM is found to be $W = 1.7 \pm 0.6$ %BZ = 0.03 ± 0.01 \AA^{-1} and the corresponding transfer width is $T = 2\pi/W = 22 \pm 6$ nm. This instrument response will be convoluted with the signal from the materials other than this Si(111) sample in the future measurements.

4.3 Results and Discussion

4.3.1 AES and AFM

The graphene/Cu(111)/spinel sample was loaded into the HRLEED chamber without any prior treatment. The sample was annealed *in situ* at 500 °C for about one hour in order to remove contaminations on the graphene¹¹⁰. The surface chemical composition was checked with *in situ* AES measurements. Figure 4.4(a) shows the AES spectrum from the surface of the sample

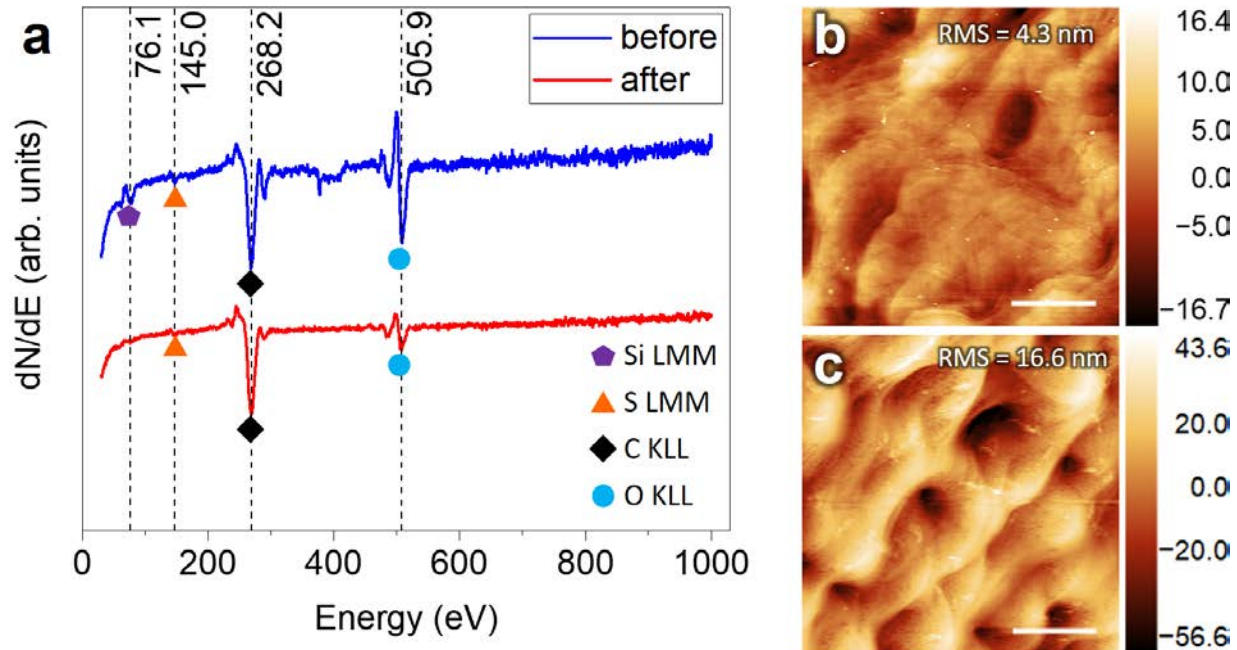


Figure 4.4: (a) AES spectrum from the graphene/Cu(111)/spinel sample surface before (blue curve) and after (red curve) the annealing at 500 °C for one hour. Auger peaks corresponding to the silicon LMM, sulfur LMM, carbon KLL and oxygen KLL transitions are labeled on the figure. AFM images measured *ex situ* from the graphene/Cu(111)/spinel sample surface (b) before and (c) after the annealing. The scale bars are both 10 μm .

Table 4.2: Atomic concentration analysis of graphene/Cu(111)/spinel sample from the AES spectrum shown in Fig. 4.4(a)

Element	Before annealing				After annealing			
	Si	S	C	O	Si	S	C	O
Peak-to-peak Intensity (I_X)	1142	759	8094	8410	0	863	13815	4507
Relative Sensitivity Factor (S_X)	0.36	0.85	0.20	0.50	0.36	0.85	0.20	0.50
I_X/S_X	3172	893	40470	16820	0	1015	69075	9014
Ratio of concentration (Si : S : C : O)	0.08 : 0.02 : 1.00 : 0.42				0.00 : 0.015 : 1.00 : 0.130			
Atomic Concentration (%)	5.2	1.5	66.0	27.4	0	1.3	87.3	11.4

before (the blue curve) and after (the red curve) the annealing. Cu LMM (\sim 920 eV) was absent in the AES spectrum, suggesting the graphene have nearly full coverage on the surface. Analysis of the atomic concentration from the AES spectrum is shown in Table 4.2. The oxygen concentration has been reduced to 11.4 % after the annealing compared to 27.4 % before. The silicon contamination is completely gone while a small amount (\sim 1.3 %) of sulfur contamination still exists on the surface after annealing.

AFM images from the graphene/Cu(111)/spinel sample surface before and after the 500 °C annealing were measured *ex situ* and shown in Figs. 4.4(b) and (c), respectively. Thermal annealing has been known for bringing roughness and defects to the copper surface^{118, 119}. The root-mean-square (RMS) roughness increased from 4.3 nm to 16.6 nm after the annealing.

4.3.2 HRLEED

Figure 4.5(a) shows the HRLEED 2D scan from this sample using 181.0 eV incident energy after the sample cooled down to room temperature. All spots are labeled with two Miller indices. There are six first order diffraction spots approximately evenly spaced. Three of them, namely, (01), (10) and ($\bar{1}\bar{1}$), have much stronger intensity than the others, which arises from the 3-fold symmetry of Cu(111). Figure 4.5(b) presents a series of the line profiles scanned along the [10 $\bar{1}0$] direction with different electron energies. The arrows in Fig. 4.5(a) denotes the [10 $\bar{1}0$] and [01 $\bar{1}0$] directions. Fig. 4.5(c) is extracted from Fig. 4.5(b), showing the profile details around (00) and (10) spots for energies ranging from 119 eV to 135 eV. With the maximum peak intensity of the (00) peaks at various energies aligned at \sim 984 pixels, one can see a splitting of (10) peaks in Fig. 4.5(c). The peak centers are indicated by two vertical dashed lines located at \sim 1852 and \sim 1884 pixels. Literature reported real space the lattice constants of graphene and Cu(111) are 2.46 Å and 2.55 Å, respectively. Since the reciprocal spacing is inversely proportional to the real spacing, the

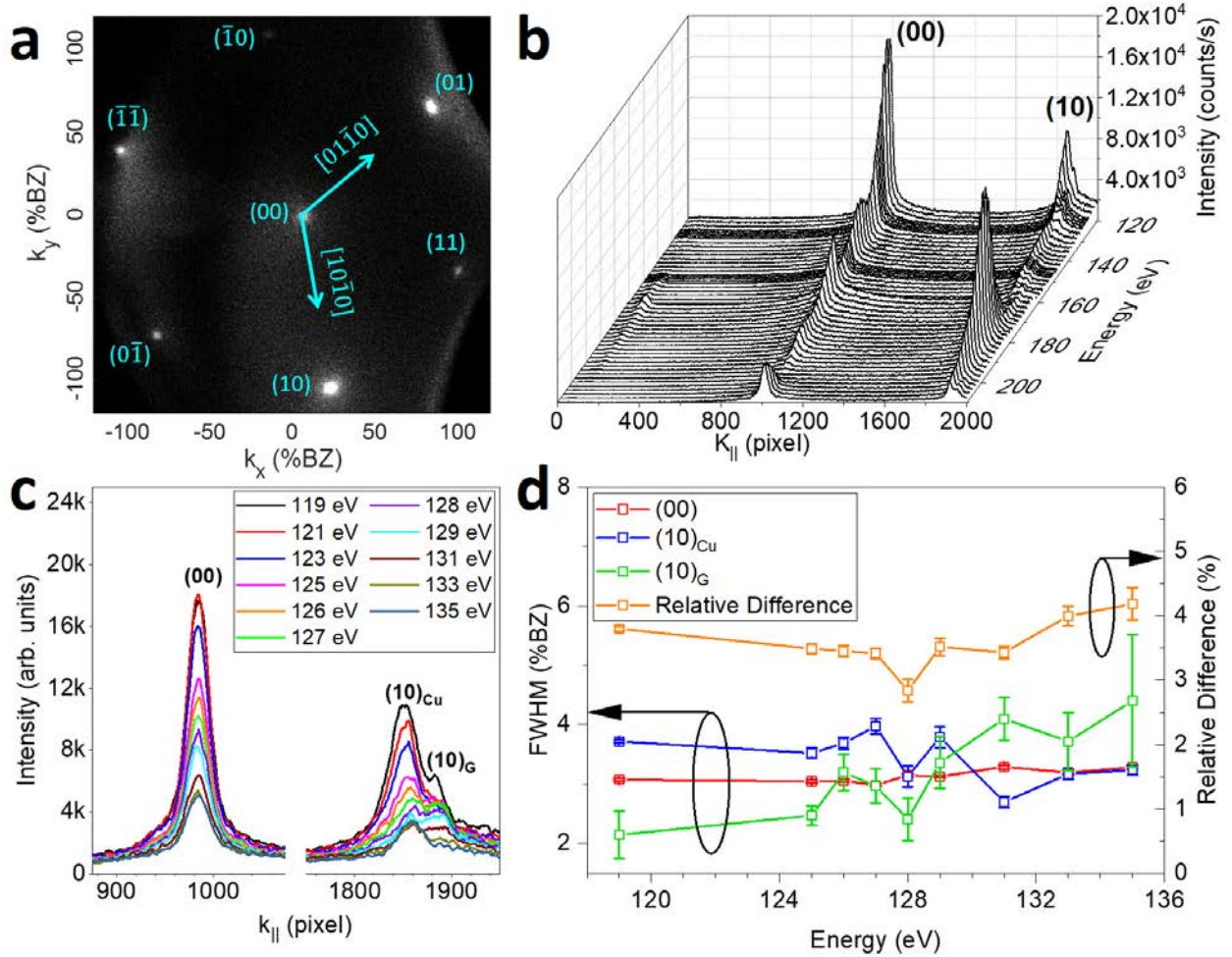


Figure 4.5: (a) Room temperature HRLEED pattern of the graphene/Cu(111)/spinel sample taken at 181 eV incident electron energy after one hour *in situ* annealing at 500 °C. The two arrows in (a) indicate the directions of $[10\bar{1}0]$ and $[01\bar{1}0]$. (b) HRLEED intensity line profiles in units of pixels scanned along the $[10\bar{1}0]$ direction with electron energies varying from 119 to 210 eV. (c) A portion of the intensity line scans extracted from (b), showing only the intensity line profiles near the (00) and (10) spots for energies ranging from 119 to 135 eV. The corresponding Miller indices are labeled above each peak. The (10) peak splits into two parts: $(10)_{Cu}$ from Cu(111) and $(10)_G$ from graphene. (d) The fitted FWHMs for the (00) , $(10)_{Cu}$, $(10)_G$ peaks and the calculated relative lattice constant difference between Cu(111) and graphene at various incident electron energies.

peak on the left is from Cu(111) and the peak on the right is from graphene, as are labeled on Fig. 4.5(c). Quantitative analyses of the profiles are carried out by fitting each peak with a pseudo-voigt function. From the fitted peak centers of those profiles we can determine the relative lattice constant difference between Cu(111) and graphene measured at various incident electron energies,

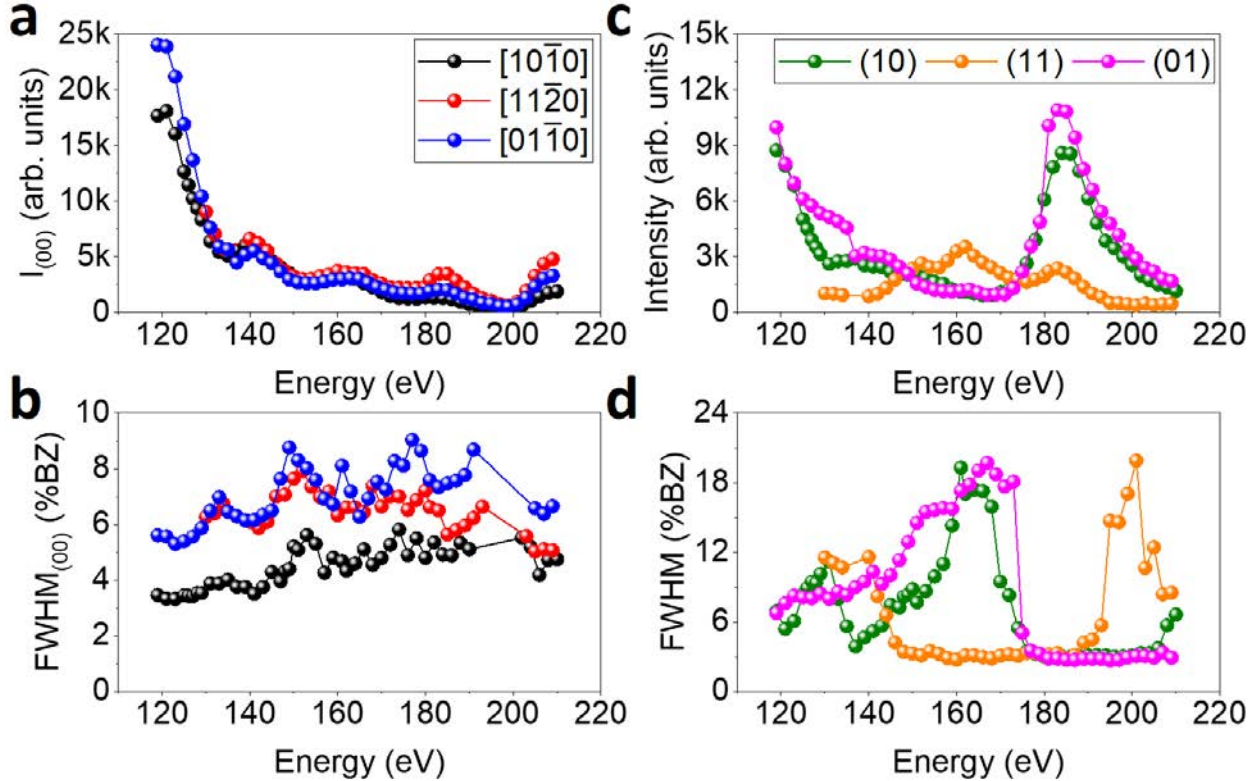


Figure 4.6: (a) Intensity vs. electron energy (IV) curves and (b) FWHM vs. electron energy curves measured at the (00) peak of the graphene/Cu(111)/spinel sample. The peak intensity or FWHM in those three curves are extracted from the fitting results of the HRLEED intensity line profiles scanned along $[10\bar{1}0]$, $[11\bar{2}0]$ and $[01\bar{1}0]$ directions, respectively. (c) IV and (d) FWHM vs. electron energy curves measured at (10), (11), and (01) peaks in a similar way as (a) and (b).

which is summarized as the orange curve in Fig. 4.5(d). The average relative difference was found to be 3.6 ± 0.4 %. This result agrees with the experimental value (3.3%) obtained by Robinson *et al.* from graphene grown *in situ* on single crystal Cu(111)¹¹⁰. In addition to the peak center positions, we also obtain the peak widths from the fitting, which are shown as the red, blue and green curves in Fig. 4.5(d) for (00), $(10)_\text{Cu}$ and $(10)_\text{G}$ peaks, respectively. Those three peaks have very similar FWHMs. The average broadening is 3.3 ± 0.5 %BZ = 0.09 ± 0.01 \AA^{-1} . This value is significantly larger than the instrument response of ~ 0.03 \AA^{-1} , suggesting a noticeable number of defects exist within both graphene and copper surface.

If we just focus on the intensity and FWHM measured at the peak center position as a function of the electron acceleration voltage, we obtain the intensity *vs.* voltage (IV) curve¹²⁰ and the FWHM *vs.* voltage curve, respectively. LEED IV curves have long been used for structure analysis of atomic positions in the surface unit cell. Figure 4.6 (a) shows the IV curves measured from the (00) peak of the graphene/Cu(111)/spinel sample with electron energies ranging from 119 to 210 eV. The three curves in Fig. 4.6(a) are extracted from the intensity line profiles scanned along [10̄10], [11̄20] and [01̄10] directions. They share a similar shape and show 5 peaks around 120 eV, 141 eV, 162 eV, 185 eV and 210 eV, respectively. Fig. 4.6(b) shows the fitted FWHMs from the (00) profiles measured at the corresponding energies. The intensity and FWHM exhibit opposite trend as a function of the energy, which is expected because the peaks are usually sharper at the in-phase conditions³⁵. The IV curve can also be obtained from non-(00) peaks. Figures 4.6(c) and (d) show the IV curves and the FWHM *vs.* energy curves, respectively, from the (10), (11) and (01) spots. The IV and FWHMs measured at (10) and (01) show similar trend while that measured at (11) is opposite. This confirms that the peak intensities as well as the FWHMs are modulated by the 3-fold symmetry of Cu(111).

Although a dynamic LEED theory is necessary for quantitative interpretation of the IV curves, a kinematic approach can still be applicable to surfaces with lightly scattering materials¹²¹. According to Horn-von Hoegen *et al.*³⁵, the LEED intensity is given by:

$$I(\mathbf{k}, k_i) = F(\mathbf{k}, k_i)G(\mathbf{k}), \quad (4.1)$$

where $F(\mathbf{k}, k_i)$ is the dynamical form factor and $G(\mathbf{k})$ is the lattice factor, which is given by:

$$G(\mathbf{k}) = \frac{1}{2\pi} \left| \sum_i e^{ia(k_x^i u_i + k_y^i v_i)} e^{idk_z^i h(u_i, v_i)} \right|^2. \quad (4.2)$$

In Eq. (4.2), $\mathbf{k} = (k_x, k_y, k_z)$ is the scattering vector, (u_i, v_i, w_i) are the fractional coordinates of the atoms within unit cell, a is the in-plan lattice constant and d is the step height in the out-of-plane direction. For the IV curve measured at the (00) spot, $k_x = k_y = 0$. If we further assume that the surface is flat without atomic steps, then $h(u_i, v_i)$ will be constant. Therefore, the lattice factor can be simplified as:

$$G_{00}(k_z) = \frac{1}{2\pi} \left| \sum_i e^{ik_z^i} \right|^2. \quad (4.3)$$

From Eq. (4.3) we can see that the step height d , which is the distance from graphene to the Cu(111) surface in our case, is solely responsible for the distribution of (00) intensity in the out-of-plane direction. Therefore, we can possibly determine d from our measured IV curve.

With that been said, a quantitative analysis of LEED IV curves is complicated by the existence of inner potential and multiple scattering, which have to be properly addressed in order to extract meaningful values. Inner potential has been known to shift the diffraction maxima¹²² (see more details in Appendix C). It could be measured by electron holograms¹²³, electron diffractions¹²⁴ and cathode ray reflection¹²⁵. In our case of graphene on copper, the inner potential is assumed to be similar as that of the bulk graphite. We have experimentally measured the inner potential of a highly oriented pyrolytic graphite (HOPG) sample using RHEED. Figure 4.7(a) shows the RHEED pattern collected from an HOPG sample with 20 keV electrons. The (00l) positions along the center streak do not agree with the expected positions, which are indicated by the red dots in Fig. 4.7(b) superposed on Fig. 4.7(a). The inner potential shifted the spots upwards. The RHEED spot positions with a series of different inner potentials has been calculated and compared with the spot positions observed in the experiment. We found that an inner potential of ~ 11.5 eV would shift the original red spots up and match the cyan spots in Fig. 4.7(b). The Miller

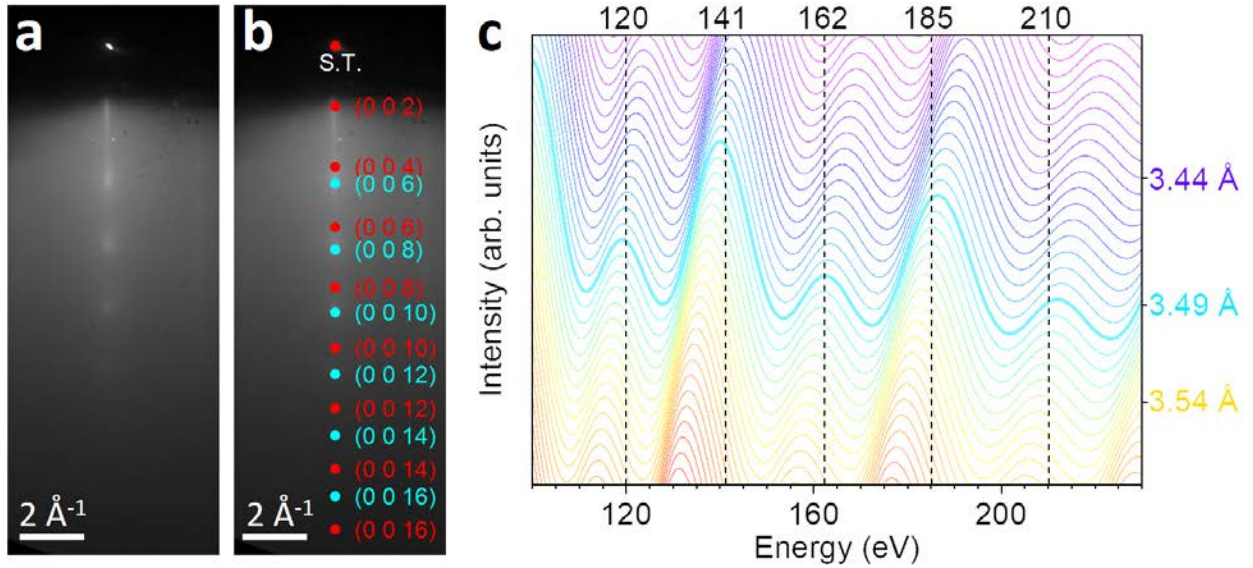


Figure 4.7: RHEED pattern from an HOPG sample using 20 keV electrons (a) without and (b) with the simulated $(00l)$ spots superposed on it. (c) Simulated LEED IV curves for a series d values ranging from 3.4 Å to 3.6 Å with a step size of 0.005 Å.

indices are labeled on the right-hand side of each spot. In literature, the reported values for the inner potential of graphite were 9 eV by LEED¹²⁶ and 10.7 eV by high-energy electron diffraction¹²⁷. Our result is close to both literature results.

Taking the inner potential \sim 11.5 eV and the double scattering effect into consideration, the LEED IV curves from graphene on copper have been simulated using the kinematic approach. Figure 4.7(c) shows a series of simulated LEED IV curves at (00) spot by varying d from 3.4 to 3.6 Å with a step size of 0.005 Å. The vertical dashed lines indicate the experimental peak positions observed in Fig. 4.6(a). The closest match between the experimental and simulated peak positions that we found from those simulated curves is at $d = 3.49$ Å, which was made obvious using a bold line in Fig. 4.7(c). Therefore we estimate the graphene to Cu(111) surface distance to be $d = 3.49 \pm 0.01$ Å from LEED IV. This result is close to that ($d = 3.27 \pm 0.07$ Å) determined by RHEED from multilayer graphene in Chapter 2.3.2.2 and the interlayer spacing of 3.36 Å in graphite.

4.4 Conclusion

This chapter presents the HRLEED characterization of the graphene on Cu(111) sample. The high resolving power of the instrument enabled us to differentiate the contribution from graphene and from Cu(111) to the diffraction intensity of the (10) spot in HRLEED 2D map. We have quantitatively analyzed the LEED IV curve from graphene on Cu(111) by comparing it with a kinematic simulation. The graphene to Cu(111) surface distance has been determined to be $d = 3.49 \pm 0.01$ Å. This suggests that the coupling between graphene and Cu metal is similar to a pure van der Waals interaction.

5. RHEED CHARACTERIZATION OF THIN FILMS GROWN VIA VAN DER WAALS EPITAXY

5.1 Introduction

Conventional hetero-epitaxial films are typically grown on lattice and symmetry matched single crystal substrates. However, the choices of such substrates are very limited. Besides, the chemical bonding at the interface is relatively strong. They may have several consequences: (1) Strain develops at the interface. (2) Various structural defects may nucleate in the overlayer. (3) The chemical inhomogeneity may be introduced in the overlayer. (4) The intermixing between the overlayer and substrate may occur at the interface. If the dangling bonds on a substrate are not fully passivated, the surface reconstruction and lattice relaxation could happen. This could affect the growth mode and structural quality of an overlayer grown on it later.

Limited choices of lattice matched single crystal substrates, possible structural imperfect overlayer, and chemical bondings at the interface of the hetero-junction in conventional hetero-epitaxy led researchers to grow high quality epitaxial films via van der Waals epitaxy (vdWE)¹²⁸. Compared to conventional hetero-epitaxies, the van der Waals substrate may not give rise to large strain in the overlayer, and therefore high density structural and chemical defects may not develop in the overlayer and at the interface¹²⁹. Thus, the lattices between the overlayer and the substrate could have a large mismatch and the overlayer could be incommensurate with the substrate at the interface¹³⁰. The lift of this restriction on lattice match greatly broadens the choices of materials used in hetero-epitaxy systems. One can imagine the growth of either layer¹³¹ or even non-layer

Portions of this chapter previously appeared as: Xiang, Y.; Yang, Y.; Guo, F.; Sun, X.; Lu, Z.; Mohanty, D.; Bhat, I.; Washington, M.; Lu, T.-M.; Wang, G.-C., van der Waals epitaxy of SnS film on single crystal graphene buffer layer on amorphous SiO₂/Si. *Appl. Surf. Sci.* **2018**, 435, 759-768.

¹³²⁻¹³⁴ epitaxial films or non-planar nanostructures ¹³⁰ on the van der Waals substrates such as graphene.

Two particularly interesting thin film materials that have recently been successfully grown via van der Waals epitaxy are tin mono-sulfide (SnS), a layered material and cadmium telluride (CdTe), a 3D material. SnS has drawn interests among photovoltaic cells (PVCs) research community worldwide ^{135, 136}. The advantages of SnS film include an optical energy band gap of 1.3 eV which is close to the optimum value required for efficient light absorption, a high optical absorption coefficient of $> 10^4 \text{ cm}^{-1}$ above the photon energy threshold ($\sim 1.3 \text{ eV}$) ¹³⁷, low cost, and non-toxic. SnS also has other applications in photodetectors ¹³⁸, gas sensors ¹³⁹, and Li-ion batteries ¹⁴⁰. One of the major challenges in the SnS thin film-based PVCs is producing high quality materials ¹⁴¹. In either case, reliable characterization as well as synthesis of electronic grade ML TMDCs are essential for translating new electronic and optical properties into applications ¹⁴². CdTe, on the other hand, is one of the most important II-VI compound semi-conductor due to its excellent optoelectronic properties ^{143, 144}. While it is commonly believed that conventional 3D materials such as GaN and CdTe do not have a 2D counterpart, recent experiment ¹⁴⁵ and first-principles calculations ¹⁴⁶ have suggested that many traditional 3D materials, including CdTe, may also exist in stable layered forms with a distinct double layer honeycomb (DLHC) structure. This bears great significance because the 2D structure not only brings new physical phenomena due to the quantum confinement effect, but also enables potential applications in flexible electronic and optoelectronic devices. Recently, ultra-thin CdTe down to $\sim 4.8 \text{ nm}$ has been successfully synthesized through VTD method ¹⁴⁷. However, detailed structural determination of this ultra-thin CdTe film was missing. It would be especially interesting to check whether the predicted DLHC structure ¹⁴⁶ exists.

In this chapter, I'll present the RHEED characterization of SnS thin film grown on single crystal graphene buffer layer on amorphous SiO₂/Si using thermal evaporation and cadmium telluride (CdTe) thin film grown on mica using vapor transport deposition (VTD). For the SnS part, I'll present the morphological characterization of graphene and SnS film using atomic force microscopy (AFM) and scanning electron microscopy (SEM). The graphene symmetry and number of orientation domains were examined by reflection high-energy electron diffraction (RHEED) 2D reciprocal space mapping. The structure and texture of the SnS thin films were measured by X-ray diffraction (XRD) and X-ray pole figure. Combining the XRD and RHEED results, we proved that the SnS film followed the symmetry of graphene in this van der Waals epitaxial growth. RHEED has also been used to characterize the structure and texture near the film surface, which is different from the bulk. The in-plane epitaxial relationship at the interface of SnS and graphene was determined by combining XRD and RHEED azimuthal scans. For the CdTe part, I'll present the characterization of the CdTe thin film using AFM and RHEED. The CdTe film has two sides, one being the surface originally facing the CdTe vapor during VTD growth and the other being the interface revealed after the exfoliation described in Chapter 1.3.1.6. I will refer to them as the CdTe surface and the CdTe interface, respectively, in the rest of this thesis. The morphology and structure of both the CdTe surface and interface have been characterized and compared with each other. Attempt has been made to characterize the CdTe interface using HRLEED but failed because of the severely warped surface after *in situ* thermal annealing.

5.2 van der Waals Epitaxy of SnS on Graphene

5.2.1 SEM, AFM and EBSD

Figures. 5.1(a) and (b) show the SEM top views of the polycrystalline graphene and single crystal graphene on SiO₂/Si substrate, respectively. Both Figs. 5.1(a) and (b) show that the major

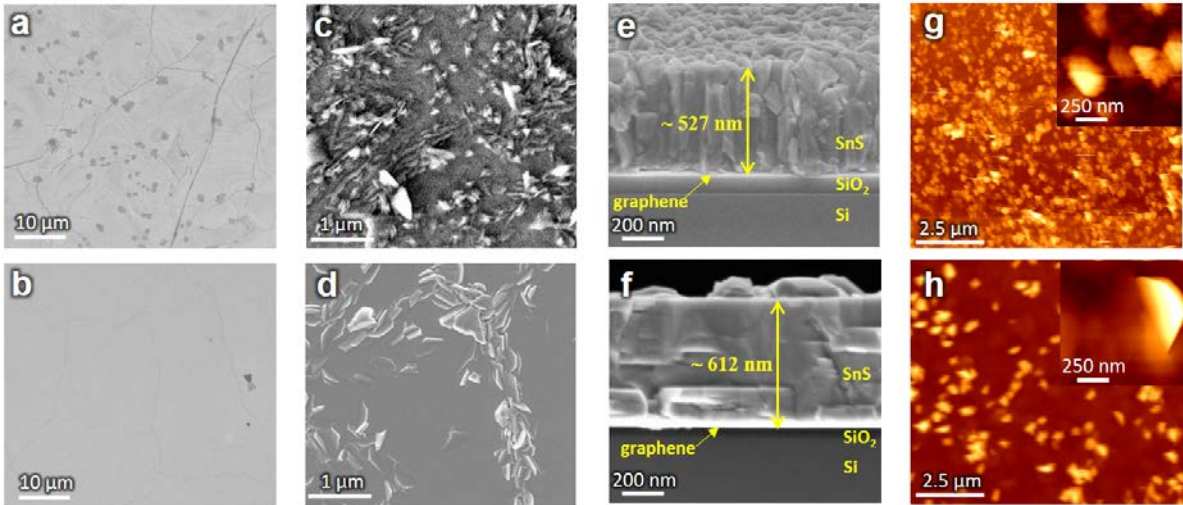


Figure 5.1: SEM top-view images of (a) bare commercial polycrystalline graphene on $\text{SiO}_2/\text{Si}(100)$, (b) bare homemade single crystal graphene on $\text{SiO}_2/\text{Si}(100)$, (c) after the deposition of SnS film on the polycrystalline graphene, and (d) after the deposition of SnS film on the single crystal graphene. SEM cross-section view images of (e) SnS film on the polycrystalline graphene on $\text{SiO}_2/\text{Si}(100)$ and (f) SnS film grown on the single crystal graphene on $\text{SiO}_2/\text{Si}(100)$. AFM top-view images of (g) SnS film on the polycrystalline graphene and (h) SnS film on the single crystal graphene. The insets in (g) and (h) show zoomed-in views from small areas in (g) and (h), respectively.

part of the surface is covered by a graphene layer, but there exist grain boundaries (dark curves), wrinkles and bilayer graphene islands. The lateral size of the bilayer island is about $2\ \mu\text{m}$ for both substrates, but the single crystal graphene surface was covered by fewer bilayer islands than that on the polycrystalline graphene. Figures 5.1(c) and (d) show SEM top views of SnS films grown on the polycrystalline and single crystal graphene substrates, respectively. The surfaces of both SnS films show many flakes scattered on a continuous film. The typical size of an individual flake for the SnS film grown on the single crystal graphene (about $400\ \text{nm}$) is larger than the one grown on the polycrystalline graphene (about $250\ \text{nm}$). Literature reports that adsorbates or particles often decorate at graphene grain boundaries¹⁴⁸. It was predicted that lines of adsorbates and particles are more reactive than the pristine lattice of graphene. Experimentally we observed that the SnS flakes form clusters along the graphene grain boundaries shown in Figs. 5.1(a) and (b). This may be due to the fact that these sites are more reactive to initiate the growth of SnS flakes. The number

density of SnS flakes on single crystal graphene is lower than that on the polycrystalline graphene, which may be attributed to fewer grain boundaries in the single crystal graphene. Figs. 5.1(e) and (f) show SEM cross section views of mechanically cleaved SnS films grown on polycrystalline graphene and single crystal graphene substrates, respectively. The thicknesses of the films are ~527 nm and ~612 nm in Figs. 5.1(e) and (f), respectively. The SnS film grown on the polycrystalline graphene has columnar like structure while that grown on the single crystal graphene has large size grains. This large size is supported by the EBSD data to be presented later.

Figures. 5.1(g) and (h) show AFM top views of the SnS films grown on polycrystalline graphene and single crystal graphene, respectively. Both films show island-like features over the surface. The high magnification images in the insets of Figs. 5.1(g) and (h) reveal the details of these features. The root-mean-square roughness of the two surfaces shown in Figs. 5.1(g) and (h) are ~37.8 nm and ~34.3 nm, respectively, which are very comparable. In the literature, typical root-mean-square roughness of 500 nm SnS films synthesized through thermal evaporation on various substrates at 300 °C are around 10 nm¹⁴⁹. Comparing to their results, our SnS films have rougher surfaces. This could be attributed to (1) the surface energy of SnS(010) (~154 mJ/m²¹⁵⁰) is higher than the surface energy of the graphene (~46.7 mJ/m² at room temperature¹⁵¹). Thus, SnS does not wet graphene and favors island growth. (2) low surface diffusion of SnS at the relatively low substrate temperature¹⁵². Recall that our substrate was held at 280 °C during growth. The film is columnar and grainy. (3) the wrinkles formed (~10 nm in height) on the initial graphene surface due to graphene's relaxation on SiO₂/Si substrates². The lateral correlation lengths of the surfaces in Figs. 5.1(g) and (h) are ~167 nm and ~286 nm, respectively. This indicates that the distribution of flakes is denser on the polycrystalline graphene than that on the single crystal graphene, which is consistent with the SEM results.

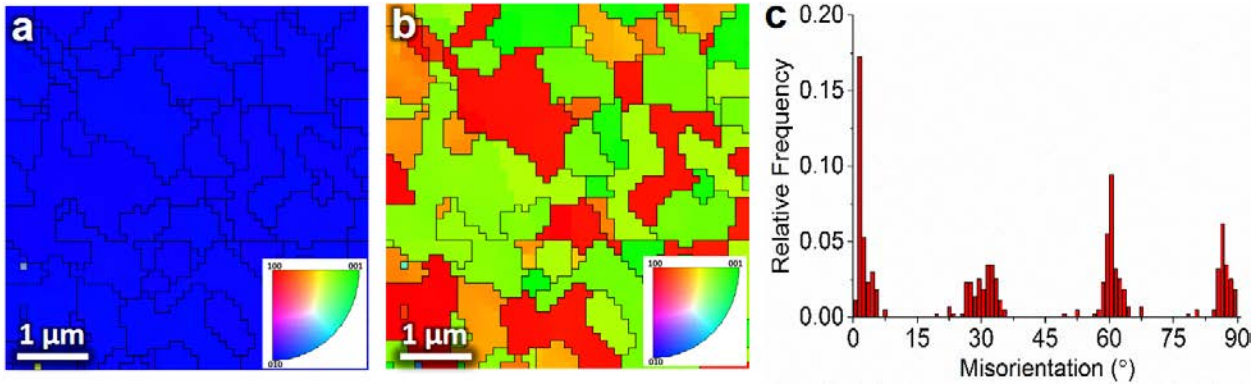


Figure 5.2 (a) EBSD IPF-Z crystallographic orientation map that shows the out-of-plane orientation in the SnS film on the homemade single crystal graphene. (b) IPF-X map which indicates the in-plane crystallographic orientations and unveils the grain boundaries in the SnS film grown on the single crystal graphene. The scale bars in (a) and (b) are 1 μm. (c) grain boundary misorientation histograms indicating the grain boundary misorientation distributions in the SnS film grown on the single crystal graphene.

The SnS film on polycrystalline graphene has a rough surface, therefore a significant fraction of the area was unresolved during the EBSD scan. In contrast, majority of the surface area can be resolved for the smoother SnS film grown on single crystal graphene. The SnS phase is detected to be orthorhombic with a space group of 62 (*Pbnm*). Figure 5.2(a) shows the crystallographic orientation map using the inverse pole figure component in the Z-direction (IPF-Z). The uniform blue color map for the SnS film on the single crystal graphene in Fig. 5.2(a) indicates a homogeneous out-of-plane orientation. Figure 5.2(b) shows the IPF-X map indicating the in-plane crystallographic orientation distribution in the SnS film. SnS grain boundaries on the single crystal graphene are well resolved in Fig. 5.2(b). The green color indicates the [001] crystal direction, and the red color indicates the [100] crystal direction. The estimated grain size is about 1 μm for this SnS film. Fig. 5.2(c) is the grain boundary misorientation histograms for SnS film on single crystal graphene. The plots show that the preferred misorientation angle for SnS film on single crystal graphene are $i \cdot 30^\circ$ where i is an integer.

5.2.2 XRD and Pole Figure

Figures 5.3(a) and (b) show X-ray diffraction intensity plotted in a logarithmic scale vs 2θ from SnS films grown on the polycrystalline graphene and the single crystal graphene, respectively. For the SnS film shown in Fig. 5.3(a), SnS(020), (040), (080) peaks at $2\theta = 15.72^\circ$, 31.87° , and 66.64° as well as Si(400) peak at 69.27° were observed. From these peaks the lattice constant b of SnS is determined to be 11.236 ± 0.007 Å (bulk lattice constant $b = 11.192$ Å). The inset a1 in Fig. 5.3(a) is a one degree zoomed-in view at the vicinity of the SnS(040) peak plotted in a linear scale showing a SnS(111) peak at 31.64° adjacent to the SnS(040) peak at 31.87° . This implies that the SnS film grown on the polycrystalline graphene may develop more than one crystal orientation. A similar behavior was observed by Devika *et al.* for the SnS film grown on a glass substrate at 300 °C using thermal evaporation¹⁵³. For the SnS film shown in Fig. 5.3(b), SnS(020), (040), (080) peaks at $2\theta = 15.80^\circ$, 31.91° , and 66.70° as well as Si(400) peak at 69.15° were observed. The lattice constant b of SnS film is determined to be 11.207 ± 0.008 Å, closer to the bulk lattice constant b . A one degree zoomed-in view plotted in inset b1 shows no SnS(111) peak, unlike the SnS film grown on the polycrystalline graphene. This means that the SnS film grown on the single crystal graphene has a single orientation.

The average vertical coherent domain size τ can be estimated from the full-width-at-half-maximum (FWHM) of X-ray peak intensity profile using Scherrer formula = $K\lambda \cdot \cos\theta/\beta$, where $K = 0.89$ is the shape factor, λ is the X-ray wavelength, and β is the experimental FWHM of the respective (hkl) diffraction peak in units of radians. For the SnS film grown on the polycrystalline graphene, the FWHM of the (020) peak is 0.21 ± 0.01 °. The estimated average vertical coherent domain size is 49.56 ± 0.02 nm. Similarly, the estimated average vertical coherent domain size for the SnS film grown on the single crystal graphene is 51.50 ± 0.02 nm.

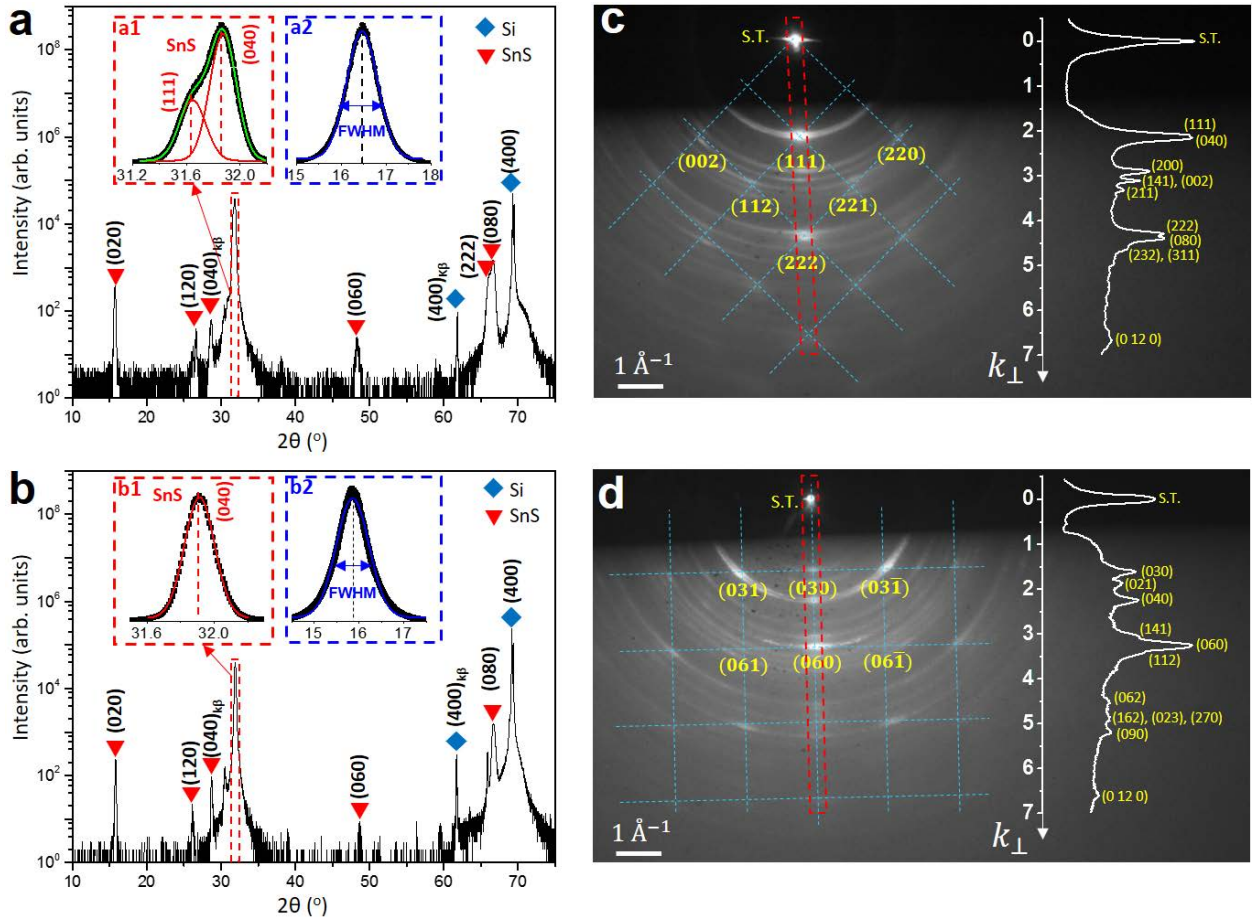


Figure 5.3: (a) XRD θ vs 2θ scan from the SnS film deposited on the commercial polycrystalline graphene/SiO₂/Si(100) substrate and the intensity is plotted in a logarithmic scale. Inset a1: A zoomed-in view of the XRD θ vs 2θ scan of the SnS film within the range $31.2^{\circ} < 2\theta < 32.2^{\circ}$ and the intensity is plotted in a linear scale. The profile contains (111) and (040) peaks. Inset a2: The XRD (040) rocking curve of the SnS film with the intensity plotted in a linear scale and 3-degree ω angular range. (b) The XRD θ vs 2θ scan from the SnS film deposited on the single crystal graphene/SiO₂/Si(100) substrate and the intensity is plotted in a logarithmic scale. Inset b1: A zoomed-in view of XRD θ vs 2θ scan of SnS film within the range $31.5^{\circ} < 2\theta < 32.5^{\circ}$ and the intensity is plotted in a linear scale. Inset b2: The XRD (040) rocking curve of the SnS film with intensity plotted in a linear scale and 3-degree ω angular range. RHEED pattern using a 15 keV electron beam collected from (c) SnS film grown on the polycrystalline graphene/SiO₂/Si(100), and (d) SnS film deposited on the single crystal graphene/SiO₂/Si(100) substrates. In each RHEED pattern, (hkl) indices were labeled below diffraction spots. The out-of-plane directions in (c) and (d) are [111] and [010], respectively. The diamond and square unit mesh are outlined in blue dashed lines in (c) and (d), respectively. Insets in (c) and (d) show radial intensity vs reciprocal distance or perpendicular momentum transfer k_{\perp} along the direction perpendicular to the substrate. The red dashed rectangular box in the RHEED pattern indicates the area where the intensity is integrated. The (hkl) indices of peaks and rings are labeled.

These values are smaller than the film thickness observed from SEM and AFM because each morphological feature may consist of many coherent domains. Note that these coherent domain sizes are estimated from measured FWHM without deconvoluting the instrument response's FWHM. Therefore, the sizes are lower limits or underestimated.

Insets a2 and b2 in Figs. 5.3(a) and (b) show the corresponding rocking curves or omega scans of the SnS(040) peak measured at theta (θ) angle of 15.93° and 15.96° from the SnS films grown on polycrystalline and single crystal graphene, respectively. The FWHMs of rocking curves fitted from the SnS films (without any instrument response deconvolution) by a Gaussian function on the polycrystalline graphene and the single crystal graphene are $0.837 \pm 0.002^\circ$ and $0.860 \pm 0.002^\circ$, respectively. As a reference, the FWHM of the rocking curve measured from the substrate Si(400) peak at θ angle 34.49° was $0.031 \pm 0.001^\circ$. Our measured FWHMs of around 0.85° are larger than the FWHM of rocking curve of 0.37° observed from SnS film grown on graphene/GaAs(100) or graphene/SiO₂/Si but smaller than 2.96° measured from SnS film grown directly on GaAs(100) or $\sim 4^\circ$ measured from SnS on glass ¹⁵⁴. Note that the reported FWHMs of rocking curves by Wang *et al.* were measured from ~ 1 μm thick SnS film grown on bi-layer graphene at 400 °C while the thicknesses of our film is only about 500 nm, and our films were grown at 280 °C.

The strong (010) out-of-plane orientation and narrow rocking curve of SnS films grown on graphene buffer layers presented above do not reveal the in-plane epitaxy of the SnS film. Figures 5.4(a)and (b) show X-ray {160} pole figures of SnS film on polycrystalline and single crystal graphene, respectively, for the (010) out-of-plane orientation. The 2θ angle for the pole figure measurements was set at 53.443°, and the step size for the azimuthal angle (ϕ) and chi angle (χ) scans were both 1°. In the SnS {160} pole figure from the SnS film grown on the polycrystalline

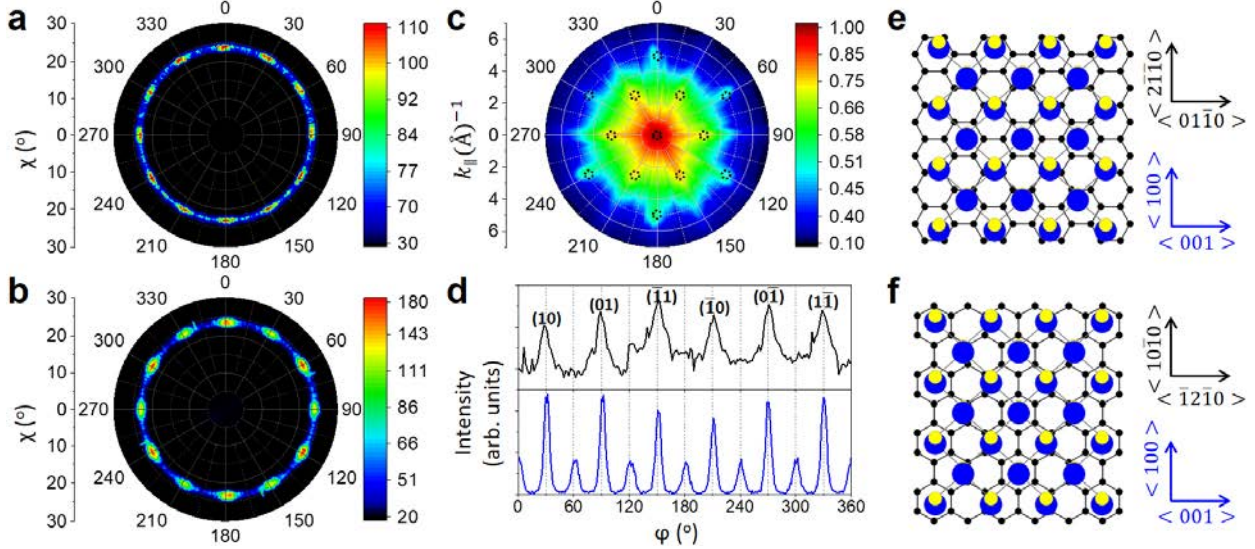


Figure 5.4: X-ray $\{160\}$ pole figures with the (010) out-of-plane orientation measured from the SnS films grown on (a) the commercial polycrystalline graphene/SiO₂/Si(100) substrate, and (b) the homemade single crystal graphene/SiO₂/Si(100) substrate. (c) RHEED 2D reciprocal space structure measured from the single crystal graphene on SiO₂/Si(100) substrate. The black dashed circles are the theoretical positions of the reciprocal lattice points of a single crystal graphene. (d) RHEED azimuthal scan (upper curve) from single crystal graphene at $k_{\parallel} = 2.9 \text{ \AA}^{-1}$ and XRD SnS(160) azimuthal scan (bottom curve) taken at $2\theta = 53.443^\circ$ and $\chi = 23.311^\circ$. The corresponding (hk) indices of single crystal graphene are labeled above each peak in the RHEED azimuthal scan. Top view of the atomic structure at the SnS/graphene interface showing the epitaxial relationship: (e) $<100>_{\text{SnS}} // <2\bar{1}\bar{1}0>_{\text{graphene}}$ and (f) $<100>_{\text{SnS}} // <10\bar{1}0>_{\text{graphene}}$. Note that $[10\bar{1}0]_{\text{graphene}}$ is rotated 30° from $[2\bar{1}\bar{1}0]_{\text{graphene}}$. Carbon, tin and sulfur atoms are represented by black, blue and yellow balls, respectively. Two perpendicular arrows indicate the crystal directions of graphene (black) and SnS (blue) next to each atomic structure.

graphene shown in Fig. 5.4(a), 12 almost even intensity poles 30° apart azimuthally at $\chi \sim 23^\circ$ were observed. For the $\{160\}$ pole figure of SnS film grown on the single crystal graphene shown in Fig. 5.4(b), there are 12 poles, but six out of 12 poles have stronger intensity. The six stronger intensity poles are 60° apart azimuthally and so are the six weaker intensity poles.

5.2.3 RHEED

The difference in the pole figures from films deposited on the polycrystalline and single crystal graphene arises from the structural difference between the polycrystalline graphene and single crystal graphene. As was reported in our earlier ARHEED work ¹, commercial

polycrystalline graphene exhibits a 12-fold symmetry and the SnS film grown on it will follow the symmetry. That's why the 12 poles of equal intensity were observed. Similar structural characterization using azimuthal RHEED has been performed on the homemade single crystal graphene. Fig. 5.4(c) shows the 2D reciprocal space structure measured from the single crystal graphene. It is clear that the single crystal graphene has only a 6-fold symmetry, which indicates that the graphene is in the single-crystal form. After the orientation of the single crystal graphene on SiO_2/Si substrate was determined, a 500 nm thick SnS film was deposited on it. It is then expected that the SnS film grown on single crystal graphene will also have a 6-fold symmetry.

Figure 5.4(d) shows a comparison between RHEED azimuthal scan from the single crystal graphene measured at parallel momentum transfer $k_{\parallel} = 2.9 \text{ \AA}^{-1}$ (upper curve) and XRD $\{160\}$ azimuthal scan from SnS film measured at $2\theta = 53.443^\circ$ and $\chi = 23.311^\circ$ (lower curve). The in-plane projection of the SnS(160) plane's normal vector has the same direction as SnS [100]. The azimuthal angle $\varphi = 0^\circ$ was defined as being parallel to graphene $[2\bar{1}\bar{1}0]$ direction (the angle between the base vectors of the graphene unit cell is chosen to be 120°) while taking XRD data. RHEED azimuthal scan in upper curve of Fig. 5.4(d) has six peaks, corresponding to (10) , (01) , $(\bar{1}1)$, $(\bar{1}0)$, $(0\bar{1})$ and $(1\bar{1})$ in the 2D reciprocal space of graphene. In the XRD azimuthal scan from the SnS $\{160\}$ planes, we expect a 6-fold symmetry. However, there are azimuthally evenly spaced 12 peaks instead of six, and the average separation between two adjacent peaks is $30 \pm 1^\circ$. Among those 12 peaks, six peaks' azimuthal positions align with the six peak positions in the RHEED azimuthal scan from the graphene and the intensities are two to three times higher than the intensities of the six peaks that are 30° apart. This means that although SnS film follows the symmetry of graphene, there exists two sets of domains having preferred relative rotation angles between SnS film and graphene with different probability. Atomic ball models showing 0° and 30°

rotation at the interface between SnS(010) lattice and graphene lattice are presented in Figs. 5.4(e) and (f), respectively. The two perpendicular arrows in black color near each atomic model indicate the in-plane orientation of graphene lattice (black balls) while the arrows in blue indicate that of SnS(010) lattice (blue and yellow balls representing Sn and S atoms, respectively). Majority of the grains in the SnS film follows $<100>_{\text{SnS}} // <10\bar{1}0>_{\text{graphene}}$ epitaxial relationship while the rest follows $<100>_{\text{SnS}} // <2\bar{1}\bar{1}0>_{\text{graphene}}$. Note that the angle between $[10\bar{1}0]$ direction and $[2\bar{1}\bar{1}0]$ direction is 30° . The corresponding rotation angles are $(i \cdot 60^\circ + 30^\circ)$ and $i \cdot 60^\circ$ (where i is an integer). The relative rotation angle is defined as 0° while the SnS $[100]$ direction is aligned with graphene $[2\bar{1}\bar{1}0]$ direction. First-principles calculation of the interaction energy for SnS/graphene system has been reported earlier by Leung *et al.*¹³¹, where they found the surface potential energy between SnS layer and graphene has a global minimum at rotation angle of $i \cdot 60^\circ$ and a local minimum at $(i \cdot 60^\circ + 30^\circ)$. The values of these two angles agree with our experimental results. However, they claimed that $i \cdot 60^\circ$ is the most preferred rotation angle while we found $(i \cdot 60^\circ + 30^\circ)$ angles dominates.

Literature reports studies of hetero systems using graphene as a buffer layer for van der Waals epitaxy. Examples are: (1) Metalorganic chemical vapor deposition of parallel epitaxial CdTe(111) was grown on graphene buffered SiO₂/Si¹³³. The lattice mismatch between CdTe and graphene is 46% and the symmetry changes from hexagonal graphene to Cubic CdTe. (2) Thermal evaporation of epitaxial CdS(001) film was grown on single crystal graphene buffered SiO₂/Si substrate¹³⁴. (3) GaAs film was grown on either exfoliated graphite flakes on Si substrate or CVD graphene on Si substrate. The GaAs film has a good (111) rocking curve of 0.06° but the pole figure shows a polycrystalline film¹⁵⁵. (4) Over 50% of 2D GaSe domains grown on transferred graphene buffer layer on SiO₂/Si substrate adopts a preferred orientation with $10.5 \pm 0.3^\circ$ interlayer

rotation¹⁵⁶. This lack of in-plane epitaxy in a film results from the random grain boundaries existed in transferred graphene layer that often has wrinkles⁶³. Clear and definite epitaxial film was demonstrated when the graphene layer was grown *in situ* from SiC wafer. An example is the growth of topological insulating Bi₂Se₃ film on either graphene buffer layer grown *in situ* on 4H-SiC wafer substrate¹⁵⁷ or double-layer graphene buffer layer grown *in situ* on 6H-SiC(0001) substrate¹⁵⁸. Non-layered epitaxial GaN film with 0.06° rocking curve has also be demonstrated on graphene grown *in situ* on 4H-SiC(0001)¹³². These previous reports indicate that a transferred graphene buffer layer on an amorphous substrate differs from the graphene layer grown on a single crystal substrate. The structural and grain boundaries of CVD grown graphene on polycrystalline Cu metal foils have relative rotational angles that exist among different grains⁶².

In addition to the 12 poles observed in the X-ray pole figure shown in Figs. 5.4(a) and (b), there is also a continuous ring at the same chi angle. The ring implies the existence of grains without a preferred in-plane-orientation, which may be associated with the randomly distributed flakes on the flat surface found in the SEM images. To confirm this, we used the surface sensitive RHEED measurement, to characterize the film structure and texture near surface. Figures 5.3(c) and (d) show the RHEED patterns of the SnS films grown on the polycrystalline graphene and the single crystal graphene taken at certain sample's in-plane azimuthal angles. The pattern consists of closely spaced concentric rings of intensity centered on the straight-through (S.T.) spot as well as some localized diffraction intensities at certain positions on each ring. Those rings in RHEED pattern indicate the presence of randomly distributed grains near the surface of the SnS film. Similar RHEED patterns were observed at other in-plane azimuthal angles. The fact that the intensities in the rings are not uniform indicates that the grain orientations near the surface of the SnS films have a texture consisted of grains that are not completely random in all directions¹⁵⁹.

Quantitative analyses of RHEED patterns in the radial direction are presented in the following to obtain the structure near the surface. The corresponding radial scans are inserted on the right in Figs. 5.3(c) and (d) to show the intensity variation as a function of reciprocal distance or as a function of momentum transfer perpendicular to the substrate (k_{\perp}) for SnS films grown on polycrystalline graphene and single crystal graphene, respectively. These curves were obtained by integrating intensity between the red dashed lines perpendicular to the substrate in the RHEED patterns shown in Figs. 5.3(c) and (d). Each peak in the radial scans corresponds to a diffraction ring in the RHEED pattern. The shape of each peak is fitted using a Gaussian function after subtracting the background, which is taken to be the diffraction intensity slightly outside of the ring⁹². We took the center of the fitted Gaussian function as the peak position. Setting the straight-through spot as the origin, we can determine the radii of each ring, or namely, the reciprocal distance from the origin to a point on a certain ring, as its corresponding peak position in the radial scan. The reciprocal distance k is related to the lattice constants of an orthorhombic crystal through the relation: $k^2 = \frac{1}{d_{hkl}^2} = \frac{h^2}{a^2} + \frac{k^2}{b^2} + \frac{l^2}{c^2}$. The lattice constants of SnS determined from the XRD are: $a = 4.33 \text{ \AA}$, $b = 11.19 \text{ \AA}$, $c = 3.98 \text{ \AA}$. Using these values, we calculated the expected radii of rings associated with different (hkl) indices for SnS film. By matching calculated radii with the measured positions of peaks k , we determined the (hkl) for each peak, as is labeled at each peak in the radial scan.

Using the same methodology just described, the spots in the RHEED patterns shown in Figs. 5.3(c) and (d) were indexed. The SnS film grown on the commercial graphene shows an (111) out-of-plane orientation (diamond unit mesh outlined by dashed blue lines) while the SnS film grown on single crystal graphene shows an (010) out-of-plane orientation (square unit mesh outlined by dashed blue lines). Compared to the XRD results, the RHEED results confirmed the

(010) orientation near the surface of the SnS film grown on the single crystal graphene and a dominant (111) orientation near the surface of the SnS film grown on the polycrystalline graphene. Due to the strong electron scattering and the near surface protrusions seen in Figs. 5.1(c) – (f), RHEED can reveal orientation(s) within the electron mean free path (tens nm) near a surface. The radial scan in Fig. 5.3(c) shows orientations such as (200), (141), (002), and (211), in addition to the (111) out-of-plane orientation from near the surface of SnS on the polycrystalline graphene. Similarly, more orientations such as (021), (141), and (112), in addition to the (010) out-of-plane orientation were observed near the surface of the SnS film grown on the single crystal graphene. This means there exist additional minor orientations near the surface that XRD are not able to detect.

5.3 van der Waals Epitaxy of CdTe on Mica

5.3.1 AFM and RHEED

van der Waals epitaxial CdTe thin film has been grown on mica substrate using the VTD method (see more details in Chapter 1.3.1.5). Figure 5.5(a) shows the RHEED pattern measured from the CdTe surface using 20 keV electrons. The zone axis (ZA) is along the [0 $\bar{1}$ 1] direction of CdTe. The intensity of the diffraction spots is very weak, but still visible. The (hkl) indices are labeled beside some diffraction spots. The spots in the central vertical dashed line in Fig. 5.5(a) are identified as (333) and (444), suggesting a (111) out-of-plane orientation. The spots on the two sides appear in pairs, which is caused by the crystal twining along the [111] twin axis. This result is very similar to what has been reported in the literature for CdTe grown on mica using MOCVD¹⁶⁰. The reason for such a weak intensity is that the surface of this CdTe/mica sample is too rough. Therefore, the diffracted signal gets buried in a diffuse background in the diffraction pattern.

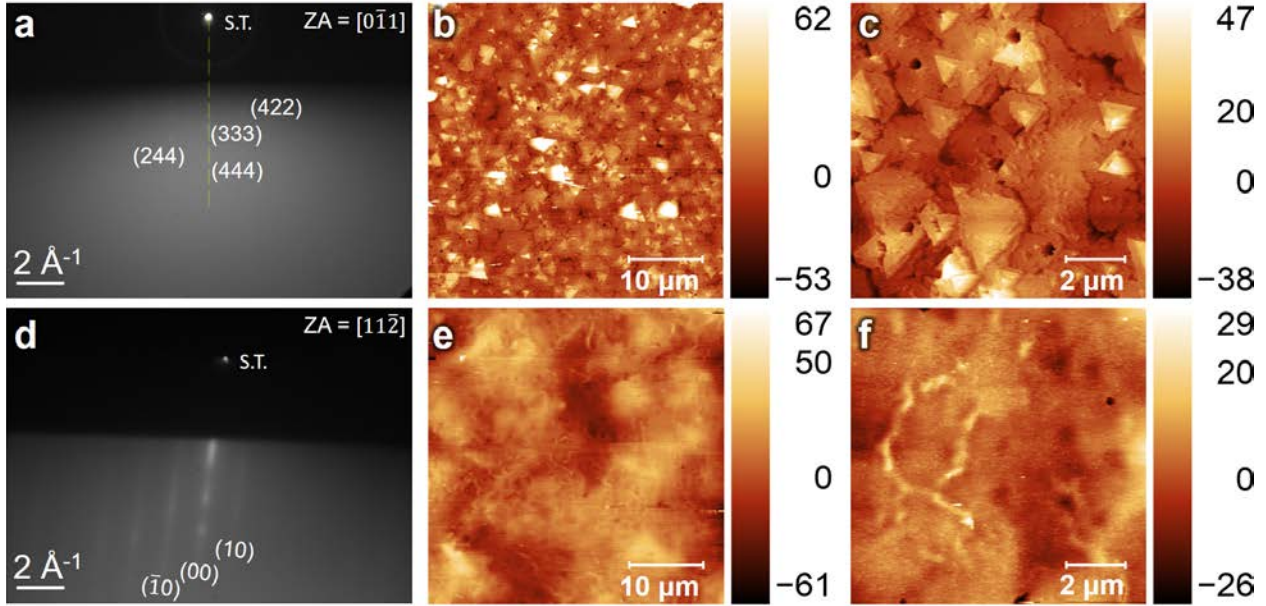


Figure 5.5: RHEED patterns from (a) the CdTe surface and (d) the CdTe interface revealed by the exfoliation. The Miller indices, the straight through (S.T.) spot and the zone axis (ZA) are labeled in both figures. A central dashed line is drawn on (a) to indicate the out-of-plane direction. AFM images from (b), (c) the CdTe surface and (e), (f) the CdTe interface. The unit in the color bars in (b), (c), (e) and (f) is nanometer.

The surface morphology has been measured from this sample using AFM, as shown in Figures 5.5(b) and (c). From Fig. 5.5(b) we calculated the RMS roughness to be $w = 16.5 \pm 0.1$ nm, the lateral correlation length to be $\xi = 1.0 \pm 0.1$ μm, and the roughness exponent to be $\alpha = 0.7 \pm 0.1$ assuming a self-affine surface. The lateral correlation length ξ represents the average flake lateral size. The relatively large RMS roughness of ~16.5 nm proves that the surface might indeed have contributed to a lot of diffuse scattering in the RHEED measurement. Figure 5.5(c) shows a zoomed-in view of Fig. 5.5(b), which shows that the triangle flakes are sitting on a coalesced layer. The thickness of each flake is measured to be ~15 nm.

After the characterization of the CdTe surface, this CdTe film has been successfully exfoliated from the mica substrate (see details in Chapter 1.3.1.6). The revealed CdTe interface is supposed to be much smoother than the CdTe surface due to the flat mica surface. This has been checked with AFM and RHEED measurements. Figure 5.5(d) shows the RHEED pattern measured

from the CdTe interface using 20 keV electrons along the $[11\bar{2}]$ zone axis of CdTe. The streaky RHEED pattern indicates that the surface is smooth in the microscopic scale. The streaks at the center are labeled using two Miller indices on Fig. 5.5(d). Notice that the streaks are tilted to the left while the shadowing edge is almost horizontal. This might indicate that the CdTe interface is not flat in the macroscopic scale after the exfoliation process. Figures 5.5(e) and (f) show the AFM images measured from the CdTe interface. From Fig. 5.5(e) the RMS roughness, lateral correlation length, and roughness exponent are calculated to be $w = 14.5 \pm 0.1$ nm, $\zeta = 3.7 \pm 0.1$ μm , and $\alpha = 0.9 \pm 0.1$, respectively. The roughness of the CdTe interface is comparable to that of the CdTe surface, but the lateral correlation length is about 4 times larger. In addition, no triangle-shape flake has been observed from the CdTe interface. More study on the origin of roughness is needed.

5.3.2 HRLEED

In order to quantitatively analyze the structure of the CdTe interface, the CdTe/epoxy/Si sample after the exfoliation process has been loaded into the HRLEED chamber for HRLEED measurements. Figures 5.6(a) and (b) compare the photos of the CdTe interface/epoxy/Si sample mounted on the HRLEED sample holder before and after the *in situ* annealing, respectively. From Fig. 5.6(b) we can see that the CdTe film became severely warped after the *in situ* annealing at around 200 °C for ~4 hours. In addition, the surface was covered with contaminants consisting of carbon and oxygen, as evidenced by the AES scan taken after the *in situ* annealing shown in Fig. 5.6(c). The surface condition was no longer suitable for HRLEED measurement. Future attempts will be made to finish the HRLEED characterization.

5.4 Conclusion

We demonstrate that a sub-micron thick layered metal chalcogenide SnS film can be grown epitaxially on an amorphous substrate buffered by a monolayer single crystal graphene, and that

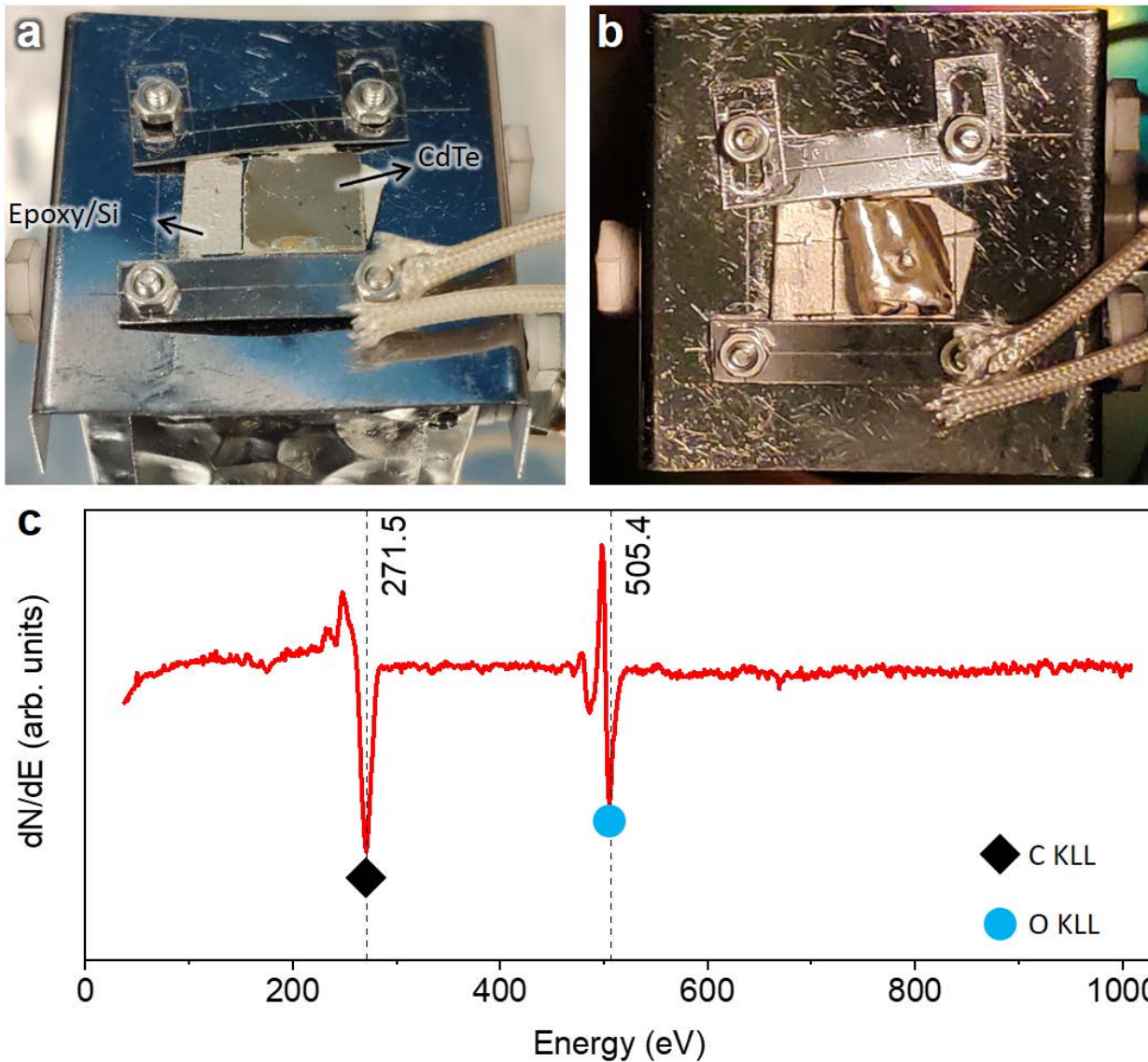


Figure 5.6: Photos of the CdTe interface /epoxy/Si sample mounted on the HRLEED sample holder (a) before and (b) after the *in situ* annealing at around 200 °C for ~4 hours. The positions of the CdTe film and the epoxy coated Si wafer are indicated in (a). (c) The AES spectrum from the surface of CdTe interface after annealing. The carbon KLL and oxygen KLL peak positions are labeled in (c).

CdTe thin film can be grown on the mica substrate and then exfoliated off to reveal a flat surface. For the SnS film, our structural characterization through X-ray pole figure shows (1) the SnS films grown on both commercial polycrystalline and homemade single crystal graphene substrates are epitaxial films with the $[010]_{\text{SnS}} // [0001]_{\text{graphene}}$ out-of-plane orientation. (2) For vdWE growth, the

structure of the graphene substrate has an influence on the SnS epi-layer. The SnS film will follow the symmetry of the graphene substrate. Even though the SnS film grown on the single crystal graphene exhibits a 6-fold symmetry, there exists two sets of relative rotation angles ($i \cdot 60^\circ$ and $i \cdot 60^\circ + 30^\circ$) between SnS and graphene while the ($i \cdot 60^\circ + 30^\circ$) angles dominate. The in-plane epitaxy for the dominant domains follows $<100>_{\text{SnS}} // <10\bar{1}0>_{\text{graphene}}$ while the minor domains follows $<100>_{\text{SnS}} // <2\bar{1}\bar{1}0>_{\text{graphene}}$. (3) EBSD IPF-X maps of SnS(010) films on both graphene substrates reveal the in-plane grain boundaries with grain orientation in 30° increment consistent with X-ray result. The grain size in SnS(010) film grown on single crystal graphene is about 1 μm . (4) The RHEED measurement shows that the near surface texture of the SnS film grown on single crystal graphene is (010) while the near surface texture of SnS film grown on polycrystalline graphene has a mixture of (010) and (111) with more dominant (111).

For the CdTe film, the RHEED pattern from the CdTe surface shows that it has a rough surface with the (111) out-of-plane orientation and crystal twinning around the [111] twin axis. The AFM images show triangle CdTe flakes with $\sim 1 \mu\text{m}$ lateral size and $\sim 15 \text{ nm}$ thickness. As a comparison, the RHEED pattern from the CdTe interface indicates a microscopically smooth but macroscopically warped surface, while the AFM images show that the CdTe interface has a similar roughness as the CdTe surface but the lateral correlation length is much larger.

6. FUTURE WORK

The work presented in this thesis has enabled us to study the 2D materials from some new perspectives. It paves the way for future studies on the novel applications of electron diffraction techniques and the undiscovered properties of the 2D materials. They include:

1. Direct structural determination by Weissenberg RHEED, which is an alternative terminology for ARHEED, has been demonstrated by Abukawa *et al.* through quantitative analysis of the 3D Patterson function¹⁶¹. This technique may be used to confirm the arrangement of the buffer layer atoms observed at the interface of MoS₂ and sapphire by TEM imaging and supported by DFT calculations.
2. Pristine MoS₂ is a diamagnetic material. But the ferromagnetism can be induced in ML or ultra-thin MoS₂ at room temperature by the formation of defects using hydrogenation¹⁶², hydrothermal treatment¹⁶³ or strain¹⁶⁴. As presented in Chapter 3, the defects give rise to diffraction peak broadening. Therefore, ARHEED can be combined with the magneto optical Kerr effect (MOKE) and magnetic force microscopy (MFM) to study the effect of defects on the induced ferromagnetism in MoS₂.
3. The exfoliated CdTe film from mica substrate became severally warped after the *in situ* annealing at around 200 °C for ~4 hours, making it impossible to be studied using HRLEED. This deformation might be due to that the two consecutively cured epoxy layers failed to make a seamless and secured contact during the exfoliation process. The exfoliation process needs to be optimized to make sure the bonding between the two epoxy layers are strong enough to hold them together when heated up to ~200 °C. The O and C contaminations also need to be removed by *in situ* Ar ion sputtering and annealing at an elevated temperature. Once the exfoliation process of CdTe from mica is optimized and

can survive under the temperature annealing, the structure of the CdTe surface revealed by the exfoliation can be quantitatively studied using HRLEED. The ideal experiment is to perform *in situ* CdTe growth and *in situ* HRLEED measurement of ultrathin CdTe. This will avoid sample contamination and sample exfoliation. This will increase the chance to grow and discover the double layer honeycomb (DLHC) structure predicted by DFT theory.

REFERENCES

1. Xiang, Y.; Guo, F. W.; Lu, T.-M.; Wang, G.-C., Reflection high-energy electron diffraction measurements of reciprocal space structure of 2D materials. *Nanotechnology* **2016**, *27* (48), 485703.
2. Lu, Z.; Sun, X.; Xiang, Y.; Washington, M. A.; Wang, G.-C.; Lu, T.-M., Revealing the Crystalline Integrity of Wafer-Scale Graphene on SiO₂/Si: An Azimuthal RHEED Approach. *ACS Appl. Mater. & Interfaces* **2017**, *9* (27), 23081-23091.
3. Gupta, A.; Sakthivel, T.; Seal, S., Recent development in 2D materials beyond graphene. *Prog. Mater. Sci.* **2015**, *73*, 44-126.
4. Geim, A. K.; Grigorieva, I. V., Van der Waals heterostructures. *Nature* **2013**, *499* (7459), 419-425.
5. Shi, Y.; Zhou, W.; Lu, A.-Y.; Fang, W.; Lee, Y.-H.; Hsu, A. L.; Kim, S. M.; Kim, K. K.; Yang, H. Y.; Li, L.-J., van der Waals epitaxy of MoS₂ layers using graphene as growth templates. *Nano Lett.* **2012**, *12* (6), 2784-2791.
6. Lee, Y. H.; Zhang, X. Q.; Zhang, W.; Chang, M. T.; Lin, C. T.; Chang, K. D.; Yu, Y. C.; Wang, J. T. W.; Chang, C. S.; Li, L. J., Synthesis of large-area MoS₂ atomic layers with chemical vapor deposition. *Adv. Mater.* **2012**, *24* (17), 2320-2325.
7. Wu, S.; Huang, C.; Aivazian, G.; Ross, J. S.; Cobden, D. H.; Xu, X., Vapor–solid growth of high optical quality MoS₂ monolayers with near-unity valley polarization. *ACS Nano* **2013**, *7* (3), 2768-2772.
8. Dumcenco, D.; Ovchinnikov, D.; Marinov, K.; Lazic, P.; Gibertini, M.; Marzari, N.; Sanchez, O. L.; Kung, Y.-C.; Krasnozhon, D.; Chen, M.-W., Large-area epitaxial monolayer MoS₂. *ACS Nano* **2015**, *9* (4), 4611-4620.
9. Zhang, X.; Choudhury, T. H.; Chubarov, M.; Xiang, Y.; Jariwala, B.; Zhang, F.; Alem, N.; Wang, G.-C.; Robinson, J. A.; Redwing, J. M., Diffusion-Controlled Epitaxy of Large Area Coalesced WSe₂ Monolayers on Sapphire. *Nano Lett.* **2018**, *18* (2), 1049-1056.
10. Hernandez, Y.; Nicolosi, V.; Lotya, M.; Blighe, F. M.; Sun, Z.; De, S.; McGovern, I.; Holland, B.; Byrne, M.; Gun'Ko, Y. K., High-yield production of graphene by liquid-phase exfoliation of graphite. *Nat. Nanotechnol.* **2008**, *3* (9), 563.
11. Li, H.; Zhang, Q.; Yap, C. C. R.; Tay, B. K.; Edwin, T. H. T.; Olivier, A.; Baillargeat, D., From Bulk to Monolayer MoS₂: Evolution of Raman Scattering. *Adv. Funct. Mater.* **2012**, *22* (7), 1385-1390.

12. Zhang, P.; Yang, S.; Pineda-Gómez, R.; Ibarlucea, B.; Ma, J.; Lohe, M. R.; Akbar, T. F.; Baraban, L.; Cuniberti, G.; Feng, X., Electrochemically Exfoliated High-Quality 2H-MoS₂ for Multiflake Thin Film Flexible Biosensors. *Small* **2019**, *15* (23), 1901265.
13. Kittel, C.; McEuen, P.; McEuen, P., "Wave Diffraction and the Reciprocal Lattice." In *Introduction to solid state physics*. edited by Stuart Johnson, 23-43. New York, NY: John Wiley & Sons, 2004.
14. Li, X.; Magnuson, C. W.; Venugopal, A.; Tromp, R. M.; Hannon, J. B.; Vogel, E. M.; Colombo, L.; Ruoff, R. S., Large-area graphene single crystals grown by low-pressure chemical vapor deposition of methane on copper. *J. Am. Chem. Soc.* **2011**, *133* (9), 2816-2819.
15. Miseikis, V.; Convertino, D.; Mishra, N.; Gemmi, M.; Mashoff, T.; Heun, S.; Haghigian, N.; Bisio, F.; Canepa, M.; Piazza, V., Rapid CVD growth of millimetre-sized single crystal graphene using a cold-wall reactor. *2D Mater.* **2015**, *2* (1), 014006.
16. Liang, X.; Sperling, B. A.; Calizo, I.; Cheng, G.; Hacker, C. A.; Zhang, Q.; Obeng, Y.; Yan, K.; Peng, H.; Li, Q., Toward clean and crackless transfer of graphene. *ACS Nano* **2011**, *5* (11), 9144-9153.
17. Li, X.; Zhu, Y.; Cai, W.; Borysiak, M.; Han, B.; Chen, D.; Piner, R. D.; Colombo, L.; Ruoff, R. S., Transfer of Large-Area Graphene Films for High-Performance Transparent Conductive Electrodes. *Nano Lett.* **2009**, *9* (12), 4359-4363.
18. Colin, R.; Drowart, J., Thermodynamic study of tin sulfide and lead sulfide using a mass spectrometer. *J. Chem. Phys.* **1962**, *37* (5), 1120-1125.
19. Qiu, X. P.; Shin, Y. J.; Niu, J.; Kulothungasagar, N.; Kalon, G.; Qiu, C.; Yu, T.; Yang, H., Disorder-free sputtering method on graphene. *AIP Advances* **2012**, *2* (3), 032121.
20. Novoselov, K. S.; Geim, A. K.; Morozov, S. V.; Jiang, D.; Zhang, Y.; Dubonos, S. V.; Grigorieva, I. V.; Firsov, A. A., Electric field effect in atomically thin carbon films. *Science* **2004**, *306* (5696), 666-669.
21. Radisavljevic, B.; Radenovic, A.; Brivio, J.; Giacometti, V.; Kis, A., Single-layer MoS₂ transistors. *Nat. Nanotechnol.* **2011**, *6*, 147.
22. Kikuchi, S., Diffraction of cathode rays by mica. *Proc. Imp. Acad.* **1928**, *4* (6), 271-274.
23. Harris, J.; Joyce, B.; Dobson, P., Oscillations in the surface structure of Sn-doped GaAs during growth by MBE. *Surf. Sci. Lett.* **1981**, *103* (1), L90-L96.
24. Wood, C. E., RED intensity oscillations during MBE of GaAs. *Surf. Sci. Lett.* **1981**, *108* (2), L441-L443.

25. Menadue, J., Si (111) surface structures by glancing-incidence high-energy electron diffraction. *Acta Crystallographica Section A: Crystal Physics, Diffraction, Theoretical and General Crystallography* **1972**, 28 (1), 1-11.
26. Maksym, P., Analysis of intensity data for RHEED by the MgO (001) surface. *Surf. Sci.* **1985**, 149 (1), 157-174.
27. Tang, F.; Wang, G. C.; Lu, T. M., Surface pole figures by reflection high-energy electron diffraction. *Appl. Phys. Lett.* **2006**, 89 (24), 241903.
28. Tang, F.; Parker, T.; Wang, G. C.; Lu, T. M., Surface texture evolution of polycrystalline and nanostructured films: RHEED surface pole figure analysis. *J. Phys. D* **2007**, 40 (23), R427-R439.
29. Wang, G.-C.; Lu, T.-M., "RHEED Transmission Mode and RHEED Pole Figure" In *RHEED Transmission Mode and Pole Figures*, 73-106, Troy, NY: Springer 2014.
30. Davisson, C.; Germer, L. H., Diffraction of Electrons by a Crystal of Nickel. *Phys. Rev.* **1927**, 30 (6), 705-740.
31. Sproull, W. T., A new type of apparatus for experiments in secondary electron diffraction. *Rev. Sci. Instrum.* **1933**, 4 (4), 193-196.
32. Estrup, P.; McRae, E., Surface studies by electron diffraction. *Surf. Sci.* **1971**, 25 (1), 1-52.
33. Lagally, M.; Martin, J., Instrumentation for low - energy electron diffraction. *Rev. Sci. Instrum.* **1983**, 54 (10), 1273-1288.
34. Scheithauer, U.; Meyer, G.; Henzler, M., A new LEED instrument for quantitative spot profile analysis. *Surf. Sci.* **1986**, 178 (1-3), 441-451.
35. Horn-von Hoegen, M., Growth of semiconductor layers studied by spot profile analysing low energy electron diffraction-Part I. *Zeitschrift für Kristallographie* **1999**, 214 (10), 591-629.
36. Eckert, M., Max von Laue and the discovery of X - ray diffraction in 1912. *Ann. Phys.* **2012**, 524 (5).
37. Zur, A.; McGill, T. C., Lattice match: An application to heteroepitaxy. *J. Appl. Phys.* **1984**, 55 (2), 378.
38. Yapsir, A.; Choi, C. H.; Lu, T. M., Observation of a new Al (111)/Si (111) orientational epitaxy. *J. Appl. Phys.* **1990**, 67 (2), 796-799.
39. Kresse, G.; Furthmüller, J., Efficient iterative schemes for ab initio total-energy calculations using a plane-wave basis set. *Phys. Rev. B* **1996**, 54, 11169.

40. Blöchl, P. E., Projector augmented-wave method. *Phys. Rev. B* **1994**, *50*, 17953.
41. Perdew, J. P.; Burke, K.; Ernzerhof, M., Generalized gradient approximation made simple. *Phys. Rev. Lett.* **1996**, *77*, 3865.
42. Klimeš, J.; Bowler, D. R.; Michaelides, A., Chemical accuracy for the van der Waals density functional. *J. Phys. Condens. Matter.* **2009**, *22*, 022201.
43. Klimeš, J.; Bowler, D. R.; Michaelides, A., Van der Waals density functionals applied to solids. *Phys. Rev. B* **2011**, *83*, 195131.
44. Ago, H.; Ohta, Y.; Hibino, H.; Yoshimura, D.; Takizawa, R.; Uchida, Y.; Tsuji, M.; Okajima, T.; Mitani, H.; Mizuno, S., Growth dynamics of single-layer graphene on epitaxial Cu surfaces. *Chem. Mater.* **2015**, *27* (15), 5377-5385.
45. Lee, J.-H.; Lee, E. K.; Joo, W.-J.; Jang, Y.; Kim, B.-S.; Lim, J. Y.; Choi, S.-H.; Ahn, S. J.; Ahn, J. R.; Park, M.-H., Wafer-scale growth of single-crystal monolayer graphene on reusable hydrogen-terminated germanium. *Science* **2014**, *344* (6181), 286-289.
46. Mun, J. H.; Cho, B. J., Synthesis of monolayer graphene having a negligible amount of wrinkles by stress relaxation. *Nano Lett.* **2013**, *13* (6), 2496-2499.
47. Pan, Y.; Zhang, H.; Shi, D.; Sun, J.; Du, S.; Liu, F.; Gao, H. j., Highly ordered, millimeter - scale, continuous, single - crystalline graphene monolayer formed on Ru (0001). *Adv. Mater.* **2009**, *21* (27), 2777-2780.
48. Zhou, H.; Yu, W. J.; Liu, L.; Cheng, R.; Chen, Y.; Huang, X.; Liu, Y.; Wang, Y.; Huang, Y.; Duan, X., Chemical vapour deposition growth of large single crystals of monolayer and bilayer graphene. *Nat. Commun.* **2013**, *4*, 2096.
49. Yan, Z.; Lin, J.; Peng, Z.; Sun, Z.; Zhu, Y.; Li, L.; Xiang, C.; Samuel, E. L.; Kittrell, C.; Tour, J. M., Toward the synthesis of wafer-scale single-crystal graphene on copper foils. *ACS Nano* **2012**, *6* (10), 9110-9117.
50. Mohsin, A.; Liu, L.; Liu, P.; Deng, W.; Ivanov, I. N.; Li, G.; Dyck, O. E.; Duscher, G.; Dunlap, J. R.; Xiao, K., Synthesis of millimeter-size hexagon-shaped graphene single crystals on resolidified copper. *ACS Nano* **2013**, *7* (10), 8924-8931.
51. Lee, Y.; Bae, S.; Jang, H.; Jang, S.; Zhu, S.-E.; Sim, S. H.; Song, Y. I.; Hong, B. H.; Ahn, J.-H., Wafer-Scale Synthesis and Transfer of Graphene Films. *Nano Lett.* **2010**, *10* (2), 490-493.
52. Nguyen, V. L.; Perello, D. J.; Lee, S.; Nai, C. T.; Shin, B. G.; Kim, J. G.; Park, H. Y.; Jeong, H. Y.; Zhao, J.; Vu, Q. A., Wafer - Scale Single - Crystalline AB - Stacked Bilayer Graphene. *Adv. Mater.* **2016**, *28* (37), 8177-8183.

53. Lee, S.; Lee, K.; Zhong, Z., Wafer Scale Homogeneous Bilayer Graphene Films by Chemical Vapor Deposition. *Nano Lett.* **2010**, *10* (11), 4702-4707.
54. Ta, H. Q.; Perello, D. J.; Duong, D. L.; Han, G. H.; Gorantla, S.; Nguyen, V. L.; Bachmatiuk, A.; Rotkin, S. V.; Lee, Y. H.; Rümmeli, M. H., Stranski-Krastanov and Volmer-Weber CVD Growth Regimes To Control the Stacking Order in Bilayer Graphene. *Nano Lett.* **2016**, *16* (10), 6403-6410.
55. Zhang, Y.; Tang, T.-T.; Girit, C.; Hao, Z.; Martin, M. C.; Zettl, A.; Crommie, M. F.; Shen, Y. R.; Wang, F., Direct observation of a widely tunable bandgap in bilayer graphene. *Nature* **2009**, *459* (7248), 820.
56. Ichimiya, A.; Cohen, P. I., *Reflection high-energy electron diffraction*. Cambridge, UK: Cambridge University Press: Cambridge, 2004.
57. Braun, W.; Möller, H.; Zhang, Y.-H., Reflection high-energy electron diffraction during substrate rotation: A new dimension for in situ characterization. *J. Vac. Sci. Technol. B* **1998**, *16* (3), 1507-1510.
58. Satapathy, D. K.; Jenichen, B.; Ploog, K. H.; Braun, W., Azimuthal reflection high-energy electron diffraction study of MnAs growth on GaAs(001) by molecular beam epitaxy. *J. Appl. Phys.* **2011**, *110* (2), 023505.
59. Boschker, J. E.; Momand, J.; Bragaglia, V.; Wang, R.; Perumal, K.; Giussani, A.; Kooi, B. J.; Riechert, H.; Calarco, R., Surface Reconstruction-Induced Coincidence Lattice Formation Between Two-Dimensionally Bonded Materials and a Three-Dimensionally Bonded Substrate. *Nano Lett.* **2014**, *14* (6), 3534-3538.
60. Allen, M. J.; Tung, V. C.; Kaner, R. B., Honeycomb carbon: a review of graphene. *Chem. Rev.* **2009**, *110* (1), 132-145.
61. Li, X.; Cai, W.; An, J.; Kim, S.; Nah, J.; Yang, D.; Piner, R.; Velamakanni, A.; Jung, I.; Tutuc, E.; Banerjee, S. K.; Colombo, L.; Ruoff, R. S., Large-area synthesis of high-quality and uniform graphene films on copper foils. *Science* **2009**, *324* (5932), 1312-4.
62. Huang, P. Y.; Ruiz-Vargas, C. S.; van der Zande, A. M.; Whitney, W. S.; Levendorf, M. P.; Kevek, J. W.; Garg, S.; Alden, J. S.; Hustedt, C. J.; Zhu, Y.; Park, J.; McEuen, P. L.; Muller, D. A., Grains and grain boundaries in single-layer graphene atomic patchwork quilts. *Nature* **2011**, *469* (7330), 389-392.
63. Deng, S.; Berry, V., Wrinkled, rippled and crumpled graphene: an overview of formation mechanism, electronic properties, and applications. *Mater. Today* **2016**, *19* (4), 197-212.
64. Fasolino, A.; Los, J. H.; Katsnelson, M. I., Intrinsic ripples in graphene. *Nat. Mater.* **2007**, *6*, 858.

65. Chen, L.; Dash, J.; Su, P.; Lin, C.; Bhat, I.; Lu, T.-M.; Wang, G.-C., Instrument response of reflection high energy electron diffraction pole figure. *Appl. Surf. Sci.* **2014**, *288*, 458-465.
66. Meyer, J.; Geim, A.; Katsnelson, M.; Novoselov, K.; Obergfell, D.; Roth, S.; Girit, C.; Zettl, A., On the roughness of single-and bi-layer graphene membranes. *Solid State Commun.* **2007**, *143* (1), 101-109.
67. Lord Rayleigh, XXXI. Investigations in optics, with special reference to the spectroscope. *Phil. Mag. (5)* **1879**, *8* (49), 261-274.
68. Costa, S. D.; Righi, A.; Fantini, C.; Hao, Y.; Magnuson, C.; Colombo, L.; Ruoff, R. S.; Pimenta, M. A., Resonant Raman spectroscopy of graphene grown on copper substrates. *Solid State Commun.* **2012**, *152* (15), 1317-1320.
69. Mooradian, A., Photoluminescence of metals. *Phys. Rev. Lett.* **1969**, *22* (5), 185.
70. Verguts, K.; Vermeulen, B.; Vrancken, N.; Schouteden, K.; Van Haesendonck, C.; Huyghebaert, C.; Heyns, M.; De Gendt, S.; Brems, S., Epitaxial Al₂O₃ (0001)/Cu (111) template development for CVD graphene growth. *J. Phys. Chem. C* **2015**, *120* (1), 297-304.
71. Miller, D. L.; Keller, M. W.; Shaw, J. M.; Rice, K. P.; Keller, R. R.; Diederichsen, K. M., Giant secondary grain growth in Cu films on sapphire. *AIP Adv.* **2013**, *3* (8), 082105.
72. Tuinstra, F.; Koenig, J. L., Raman spectrum of graphite. *J. Chem. Phys.* **1970**, *53* (3), 1126-1130.
73. Ferrari, A. C., Raman spectroscopy of graphene and graphite: disorder, electron–phonon coupling, doping and nonadiabatic effects. *Solid State Commun.* **2007**, *143* (1-2), 47-57.
74. Pozzo, M.; Alfe, D.; Lacovic, P.; Hofmann, P.; Lizzit, S.; Baraldi, A., Thermal expansion of supported and freestanding graphene: lattice constant versus interatomic distance. *Phys. Rev. Lett.* **2011**, *106* (13), 135501.
75. Jacobberger, R. M.; Arnold, M. S., Graphene growth dynamics on epitaxial copper thin films. *Chem. Mater.* **2013**, *25* (6), 871-877.
76. Nie, S.; Wofford, J. M.; Bartelt, N. C.; Dubon, O. D.; McCarty, K. F., Origin of the mosaicity in graphene grown on Cu (111). *Phys. Rev. B* **2011**, *84* (15), 155425.
77. Ferralis, N.; Pussi, K.; Finberg, S.; Smerdon, J.; Lindroos, M.; McGrath, R.; Diehl, R., Low-energy electron diffraction study of potassium adsorbed on single-crystal graphite and highly oriented pyrolytic graphite. *Phys. Rev. B* **2004**, *70* (24), 245407.
78. Bhimanapati, G. R.; Lin, Z.; Meunier, V.; Jung, Y.; Cha, J.; Das, S.; Xiao, D.; Son, Y.; Strano, M. S.; Cooper, V. R.; Liang, L.; Louie, S. G.; Ringe, E.; Zhou, W.; Kim, S. S.; Naik, R. R.; Sumpster, B. G.; Terrones, H.; Xia, F.; Wang, Y.; Zhu, J.; Akinwande, D.; Alem, N.;

Schuller, J. A.; Schaak, R. E.; Terrones, M.; Robinson, J. A., Recent Advances in Two-Dimensional Materials beyond Graphene. *ACS Nano* **2015**, *9* (12), 11509-11539.

79. Zhang, X.; Meng, F.; Christianson, J. R.; Arroyo-Torres, C.; Lukowski, M. A.; Liang, D.; Schmidt, J. R.; Jin, S., Vertical Heterostructures of Layered Metal Chalcogenides by van der Waals Epitaxy. *Nano Lett.* **2014**, *14* (6), 3047-3054.

80. Guay, D.; Divigalpitiya, W. M. R.; Belanger, D.; Feng, X. H., Chemical Bonding in Restacked Single-Layer MoS₂ by X-ray Absorption Spectroscopy. *Chem. Mater.* **1994**, *6* (5), 614-619.

81. Lee, C.; Yan, H.; Brus, L. E.; Heinz, T. F.; Hone, J.; Ryu, S., Anomalous Lattice Vibrations of Single- and Few-Layer MoS₂. *ACS Nano* **2010**, *4* (5), 2695-2700.

82. Splendiani, A.; Sun, L.; Zhang, Y.; Li, T.; Kim, J.; Chim, C.-Y.; Galli, G.; Wang, F., Emerging photoluminescence in monolayer MoS₂. *Nano Lett.* **2010**, *10* (4), 1271-1275.

83. Yu, H.; Liao, M.; Zhao, W.; Liu, G.; Zhou, X. J.; Wei, Z.; Xu, X.; Liu, K.; Hu, Z.; Deng, K.; Zhou, S.; Shi, J.-A.; Gu, L.; Shen, C.; Zhang, T.; Du, L.; Xie, L.; Zhu, J.; Chen, W.; Yang, R.; Shi, D.; Zhang, G., Wafer-Scale Growth and Transfer of Highly-Oriented Monolayer MoS₂ Continuous Films. *ACS Nano* **2017**, *11* (12), 12001-12007.

84. Rosenberger, M. R.; Chuang, H.-J.; McCreary, K. M.; Li, C. H.; Jonker, B. T., Electrical Characterization of Discrete Defects and Impact of Defect Density on Photoluminescence in Monolayer WS₂. *ACS Nano* **2018**, *12* (2), 1793-1800.

85. Lin, Y.-C.; Jariwala, B.; Bersch, B. M.; Xu, K.; Nie, Y.; Wang, B.; Eichfeld, S. M.; Zhang, X.; Choudhury, T. H.; Pan, Y.; Addou, R.; Smyth, C. M.; Li, J.; Zhang, K.; Haque, M. A.; Fölsch, S.; Feenstra, R. M.; Wallace, R. M.; Cho, K.; Fullerton-Shirey, S. K.; Redwing, J. M.; Robinson, J. A., Realizing Large-Scale, Electronic-Grade Two-Dimensional Semiconductors. *ACS Nano* **2018**, *12* (2), 965-975.

86. Wang, S.; Lee, G.-D.; Lee, S.; Yoon, E.; Warner, J. H., Detailed Atomic Reconstruction of Extended Line Defects in Monolayer MoS₂. *ACS Nano* **2016**, *10* (5), 5419-5430.

87. Edelberg, D.; Rhodes, D.; Kerelsky, A.; Kim, B.; Wang, J.; Zangiabadi, A.; Kim, C.; Abhinandan, A.; Ardelean, J.; Scully, M.; Scullion, D.; Embon, L.; Zu, R.; Santos, E. J. G.; Balicas, L.; Marianetti, C.; Barmak, K.; Zhu, X.; Hone, J.; Pasupathy, A. N., Approaching the Intrinsic Limit in Transition Metal Diselenides via Point Defect Control. *Nano Lett.* **2019**, *19* (7), 4371-4379.

88. Henzler, M., LEED studies of surface imperfections. *Appl. Surf. Sci.* **1982**, *11-12*, 450-469.

89. Meyer, G.; Wollschläger, J.; Henzler, M., Epitaxial growth of thin copper layers on Cu(111) studied by high-resolution low-energy-electron-diffraction. *Surf. Sci.* **1990**, *231* (1), 64-75.

90. Henzler, M.; Marienhoff, P., High resolution measurement of the step distribution at the Si/SiO₂ interface. *J. Vac. Sci. Technol. B* **1984**, *2* (3), 346-348.
91. Lu, T.-M.; Wang, G.-C.; Lagally, M., Quantitative island size determination in the chemisorbed layer W (110) p (2× 1)—O: II. Theoretical models. *Surf. Sci.* **1981**, *107* (2-3), 494-518.
92. Drotar, J. T.; Lu, T. M.; Wang, G. C., Real-time observation of initial stages of copper film growth on silicon oxide using reflection high-energy electron diffraction. *J. Appl. Phys.* **2004**, *96* (12), 7071.
93. Cuccureddu, F.; Murphy, S.; Shvets, I. V.; Porcu, M.; Zandbergen, H. W.; Sidorov, N. S.; Bozhko, S. I., Surface morphology of c-plane sapphire (α -alumina) produced by high temperature anneal. *Surf. Sci.* **2010**, *604* (15), 1294-1299.
94. Kurnosikov, O.; Pham Van, L.; Cousty, J., About anisotropy of atomic-scale height step on (0001) sapphire surface. *Surf. Sci.* **2000**, *459* (3), 256-264.
95. Heffelfinger, J. R.; Bench, M. W.; Carter, C. B., Steps and the structure of the (0001) α -alumina surface. *Surf. Sci.* **1997**, *370* (1), L168-L172.
96. Chen, L.; Liu, B.; Ge, M.; Ma, Y.; Abbas, A. N.; Zhou, C., Step-Edge-Guided Nucleation and Growth of Aligned WSe₂ on Sapphire via a Layer-over-Layer Growth Mode. *ACS Nano* **2015**, *9* (8), 8368-8375.
97. Zhao, Y.; Wang, G.-C.; Lu, T.-M., *Characterization of Amorphous and Crystalline Rough Surface--Principles and Applications*. Troy, NY: Academic Press: 2000.
98. Wang, R.; Guo, D.; Xie, G.; Pan, G., Atomic Step Formation on Sapphire Surface in Ultra-precision Manufacturing. *Sci. Rep.* **2016**, *6*, 29964.
99. Tan, L. K.; Liu, B.; Teng, J. H.; Guo, S.; Low, H. Y.; Loh, K. P., Atomic layer deposition of a MoS₂ film. *Nanoscale* **2014**, *6* (18), 10584-10588.
100. Aljarb, A.; Cao, Z.; Tang, H.-L.; Huang, J.-K.; Li, M.; Hu, W.; Cavallo, L.; Li, L.-J., Substrate Lattice-Guided Seed Formation Controls the Orientation of 2D Transition-Metal Dichalcogenides. *ACS Nano* **2017**, *11* (9), 9215-9222.
101. Chen, W.; Zhao, J.; Zhang, J.; Gu, L.; Yang, Z.; Li, X.; Yu, H.; Zhu, X.; Yang, R.; Shi, D., Oxygen-assisted chemical vapor deposition growth of large single-crystal and high-quality monolayer MoS₂. *J. Am. Chem. Soc.* **2015**, *137* (50), 15632-15635.
102. Young, J. R.; Chilcote, M.; Barone, M.; Xu, J.; Katoch, J.; Luo, Y. K.; Mueller, S.; Asel, T. J.; Fullerton-Shirey, S. K.; Kawakami, R., Uniform large-area growth of nanotemplated high-quality monolayer MoS₂. *Appl. Phys. Lett.* **2017**, *110* (26), 263103.

103. Ji, Q.; Kan, M.; Zhang, Y.; Guo, Y.; Ma, D.; Shi, J.; Sun, Q.; Chen, Q.; Zhang, Y.; Liu, Z., Unravelling Orientation Distribution and Merging Behavior of Monolayer MoS₂ Domains on Sapphire. *Nano Lett.* **2015**, *15* (1), 198-205.
104. He, T.; Li, Y.; Zhou, Z.; Zeng, C.; Qiao, L.; Lan, C.; Yin, Y.; Li, C.; Liu, Y., Synthesis of large-area uniform MoS₂ films by substrate-moving atmospheric pressure chemical vapor deposition: from monolayer to multilayer. *2D Mater.* **2019**, *6* (2), 025030 (11pp).
105. Mikhail, C.; Tanushree, H. C.; Xiaotian, Z.; Joan, M. R., In-plane x-ray diffraction for characterization of monolayer and few-layer transition metal dichalcogenide films. *Nanotechnology* **2018**, *29* (5), 055706.
106. Yang, H. N.; Fang, K.; Wang, G. C.; Lu, T. M., Vacancy-induced disordering in the Pb(100) surface. *Phys. Rev. B* **1991**, *44* (3), 1306-1310.
107. Mignuzzi, S.; Pollard, A. J.; Bonini, N.; Brennan, B.; Gilmore, I. S.; Pimenta, M. A.; Richards, D.; Roy, D., Effect of disorder on Raman scattering of single-layer MoS₂. *Phys. Rev. B* **2015**, *91* (19), 195411.
108. Spadacini, R.; Tommei, G. E., A Markovian approach to atomic scattering from rough surfaces. *Surf. Sci.* **1983**, *133* (1), 216-232.
109. Aurenhammer, F., Voronoi diagrams—a survey of a fundamental geometric data structure. *ACM Comput. Surv.* **1991**, *23* (3), 345-405.
110. Robinson, Z. R.; Tyagi, P.; Mowll, T. R.; Ventrice Jr, C. A.; Hannon, J. B., Argon-assisted growth of epitaxial graphene on Cu (111). *Phys. Rev. B* **2012**, *86* (23), 235413.
111. Hattab, H.; N'Diaye, A. T.; Wall, D.; Klein, C.; Jnawali, G.; Coraux, J.; Busse, C.; van Gastel, R.; Poelsema, B.; Michely, T.; Meyer zu Heringdorf, F.-J.; Horn-von Hoegen, M., Interplay of Wrinkles, Strain, and Lattice Parameter in Graphene on Iridium. *Nano Lett.* **2012**, *12* (2), 678-682.
112. Orlando, F.; Lacovic, P.; Omiciuolo, L.; Apostol, N. G.; Larciprete, R.; Baraldi, A.; Lizzit, S., Epitaxial growth of a single-domain hexagonal boron nitride monolayer. *ACS Nano* **2014**, *8* (12), 12063-12070.
113. Bana, H.; Travaglia, E.; Bignardi, L.; Lacovic, P.; Sanders, C. E.; Dendzik, M.; Michiardi, M.; Bianchi, M.; Lizzit, D.; Presel, F.; De Angelis, D.; Apostol, N.; Kumar Das, P.; Fujii, J.; Vobornik, I.; Larciprete, R.; Baraldi, A.; Hofmann, P.; Lizzit, S., Epitaxial growth of single-orientation high-quality MoS₂ monolayers. *2D Mater.* **2018**, *5* (3), 035012.
114. Wang, G.-C.; Lu, T.-M., Strain measurement of ultrathin epitaxial films using electron diffraction techniques. *J. Appl. Phys.* **2019**, *125* (8), 082401.

115. Zuo, J. K.; Harper, R. A.; Wang , G.-C., Roughening of Si(111) surface under high-temperature thermal cycling. *Appl. Phys. Lett.* **1987**, *51* (4), 250-252.
116. Yates Jr, J. T., "Thermal Control." In *Experimental innovations in Surface Science*, 491-600. Pittsburgh,PA: Springer, 1998.
117. Park, R. L.; Houston, J. E.; Schreiner, D. G., The LEED Instrument Response Function. *Rev. Sci. Instrum.* **1971**, *42* (1), 60-65.
118. Villain, J.; Grempel, D. R.; Lapujoulade, J., Roughening transition of high-index crystal faces: the case of copper. *J. Phys. F Met. Phys.* **1985**, *15* (4), 809-834.
119. Bloch, J.; Lüpke, G.; Janz, S.; van Driel, H., Detection of thermally generated defects on a Cu (111) surface. *Phys. Rev. B* **1992**, *45* (20), 12011.
120. Van Hove, M. A.; Tong, S. Y., *Surface crystallography by LEED: theory, computation and structural results*, edited by Robert Gomer, Berkeley CA: Springer-Verlag Berlin Heidelberg, 2012.
121. Vanhove, M. A.; Weinberg, W. H.; Chan, C.-M., *Low-energy electron diffraction: experiment, theory and surface structure determination*, edited by Gerhard Ertl, Berkeley CA: Springer-Verlag Berlin Heidelberg, 2012.
122. Thomson, G. P., XCI. The effect of refraction on electron diffraction. *Lond. Edinb. Dubl. Phil. Mag.* **1928**, *6* (38), 939-942.
123. Gajdardziska-Josifovska, M.; McCartney, M. R.; de Ruijter, W. J.; Smith, D. J.; Weiss, J. K.; Zuo, J. M., Accurate measurements of mean inner potential of crystal wedges using digital electron holograms. *Ultramicroscopy* **1993**, *50* (3), 285-299.
124. Yamamoto, N.; Spence, J. C. H., Surface imaging of III-V semiconductors by reflection electron microscopy and inner potential measurements. *Thin Solid Films* **1983**, *104* (1), 43-55.
125. Yamaguti, T.; ocirc, Determination of Inner Potentials of some Crystals by Method of Cathode Ray Reflection. *Proc. Phys.-Math. Soc. Japan. 3rd Series* **1932**, *14*, 1-6.
126. Lander, J. J.; Morrison, J., Low - Energy Electron Diffraction Study of Graphite. *J. Appl. Phys.* **1964**, *35* (12), 3593-3598.
127. Jenkins, R. O., XXXV. Electron diffraction experiments with graphite and carbon surfaces. *Lond. Edinb. Dubl. Phil. Mag.* **1934**, *17* (112), 457-466.
128. Koma, A., Van der Waals epitaxy for highly lattice-mismatched systems. *J. Cryst. Growth* **1999**, *201-202*, 236-241.

129. Koma, A.; Sunouchi, K.; Miyajima, T., Special Issue on Nanometer Structure Electronics Fabrication and characterization of heterostructures with subnanometer thickness. *Microelectron. Eng.* **1984**, 2 (1), 129-136.
130. Bakti Utama, M. I.; Zhang, Q.; Zhang, J.; Yuan, Y.; Belarre, F. J.; Arbiol, J.; Xiong, Q., Recent developments and future directions in the growth of nanostructures by van der Waals epitaxy. *Nanoscale* **2013**, 5 (9), 3570-3588.
131. Leung, K. K.; Wang, W.; Shu, H.; Hui, Y. Y.; Wang, S.; Fong, P. W.; Ding, F.; Lau, S. P.; Lam, C.-h.; Surya, C., Theoretical and experimental investigations on the growth of SnS van der Waals epitaxies on graphene buffer layer. *Cryst. Growth Des.* **2013**, 13 (11), 4755-4759.
132. Kim, J.; Bayram, C.; Park, H.; Cheng, C.-W.; Dimitrakopoulos, C.; Ott, J. A.; Reuter, K. B.; Bedell, S. W.; Sadana, D. K., Principle of direct van der Waals epitaxy of single-crystalline films on epitaxial graphene. *Nat Commun* **2014**, 5.
133. Mohanty, D.; Xie, W.; Wang, Y.; Lu, Z.; Shi, J.; Zhang, S.; Wang, G.-C.; Lu, T.-M.; Bhat, I. B., van der Waals epitaxy of CdTe thin film on graphene. *Appl. Phys. Lett.* **2016**, 109 (14), 143109.
134. Sun, X.; Lu, Z.; Xie, W.; Wang, Y.; Shi, J.; Zhang, S.; Washington, M. A.; Lu, T.-M., van der Waals epitaxy of CdS thin films on single-crystalline graphene. *Appl. Phys. Lett.* **2017**, 110 (15), 153104.
135. Sinsermsuksakul, P.; Sun , L.; Lee , S. W.; Park , H. H.; Kim, S. B.; Yang , C.; Gordon, R. G., Overcoming Efficiency Limitations of SnS-Based Solar Cells. *Adv. Energy Mater.* **2014**, 4 (15), 1400496.
136. Andrade-Arvizu, J. A.; Courel-Piedrahita, M.; Vigil-Gala'n, O., SnS-based thin film solar cells: perspectives over the last 25 years. *J Mater Sci: Mater. Electron.* **2015**, 26 (7), 4541-4556.
137. Tanusevski, A., Optical and photoelectric properties of SnS thin films prepared by chemical bath deposition. *Semicond. Sci. Technol.* **2003**, 18 (6), 501.
138. Zhang, H.; Hu, C.; Wang, X.; Xi, Y.; Li, X., Synthesis and photosensitivity of SnS nanobelts. *J. Alloys Compd.* **2012**, 513, 1-5.
139. Lu, F.; Yang, J.; Li, R.; Huo, N.; Li, Y.; Wei, Z.; Li, J., Gas-dependent photoresponse of SnS nanoparticles-based photodetectors. *J. Mater. Chem. C* **2015**, 3 (6), 1397-1402.
140. Lu, J.; Nan, C.; Li, L.; Peng, Q.; Li, Y., Flexible SnS nanobelts: Facile synthesis, formation mechanism and application in Li-ion batteries. *Nano Res.* **2013**, 6 (1), 55-64.
141. Banai, R. E.; Horn, M. W.; Brownson, J. R. S., A review of tin (II) monosulfide and its potential as a photovoltaic absorber. *Sol. Energy Mater. Sol. Cells* **2016**, 150, 112-129.

142. Briggs, N.; Subramanian, S.; Lin, Z.; Li, X.; Zhang, X.; Zhang, K.; Xiao, K.; Geohegan, D.; Wallace, R.; Chen, L.-Q.; Terrones, M.; Ebrahimi, A.; Das, S.; Redwing, J.; Hinkle, C.; Momeni, K.; van Duin, A.; Crespi, V.; Kar, S.; Robinson, J. A., A roadmap for electronic grade 2D materials. *2D Mater.* **2019**, *6* (2), 022001.
143. Britt, J.; Ferekides, C., Thin - film CdS/CdTe solar cell with 15.8% efficiency. *Appl. Phys. Lett.* **1993**, *62* (22), 2851-2852.
144. Gloeckler, M.; Sankin, I.; Zhao, Z., CdTe solar cells at the threshold to 20% efficiency. *IEEE J. Photovolt.* **2013**, *3* (4), 1389-1393.
145. Al Balushi, Z. Y.; Wang, K.; Ghosh, R. K.; Vilá, R. A.; Eichfeld, S. M.; Caldwell, J. D.; Qin, X.; Lin, Y.-C.; DeSario, P. A.; Stone, G.; Subramanian, S.; Paul, D. F.; Wallace, R. M.; Datta, S.; Redwing, Joan M.; Robinson, J. A., Two-dimensional gallium nitride realized via graphene encapsulation. *Nat. Mater.* **2016**, *15*, 1166.
146. Lucking, M. C.; Xie, W.; Choe, D.-H.; West, D.; Lu, T.-M.; Zhang, S. B., Traditional Semiconductors in the Two-Dimensional Limit. *Phys. Rev. Lett.* **2018**, *120* (8), 086101.
147. Cheng, R.; Wen, Y.; Yin, L.; Wang, F.; Wang, F.; Liu, K.; Shifa, T. A.; Li, J.; Jiang, C.; Wang, Z., Ultrathin Single - Crystalline CdTe Nanosheets Realized via Van der Waals Epitaxy. *Adv. Mater.* **2017**.
148. Malola, S.; Häkkinen, H.; Koskinen, P., Structural, chemical, and dynamical trends in graphene grain boundaries. *Phys. Rev. B* **2010**, *81* (16), 165447.
149. Devika, M.; Reddy, N. K.; Ramesh, K.; Sumana, H.; Gunasekhar, K.; Gopal, E.; Reddy, K. R., The effect of substrate surface on the physical properties of SnS films. *Semicond. Sci. Technol.* **2006**, *21* (10), 1495.
150. Stevanović, V.; Hartman, K.; Jaramillo, R.; Ramanathan, S.; Buonassisi, T.; Graf, P., Variations of ionization potential and electron affinity as a function of surface orientation: The case of orthorhombic SnS. *Appl. Phys. Lett.* **2014**, *104* (21), 211603.
151. Wang, S.; Zhang, Y.; Abidi, N.; Cabrales, L., Wettability and surface free energy of graphene films. *Langmuir* **2009**, *25* (18), 11078-11081.
152. Minnam Reddy, V. R.; Gedi, S.; Park, C.; R.W, M.; K.T, R. R., Development of sulphurized SnS thin film solar cells. *Curr. Appl. Phys.* **2015**, *15* (5), 588-598.
153. Devika, M.; Koteeswara Reddy, N.; Prashantha, M.; Ramesh, K.; Venkatramana Reddy, S.; Hahn, Y.; Gunasekhar, K., The physical properties of SnS films grown on lattice - matched and amorphous substrates. *Phys. Status Solidi A* **2010**, *207* (8), 1864-1869.
154. Wang, W.; Leung, K. K.; Fong, W. K.; Wang, S. F.; Hui, Y. Y.; Lau, S. P.; Surya, C. In *Growth of high quality SnS van der Waals epitaxies on graphene buffer layer for photovoltaic*

applications, Solid-State and Integrated Circuit Technology (ICSICT), 2012 IEEE 11th International Conference on, Oct. 29 2012-Nov. 1 2012; 2012; pp 1-4.

155. Alaskar, Y.; Arafin, S.; Lin, Q.; Wickramaratne, D.; McKay, J.; Norman, A. G.; Zhang, Z.; Yao, L.; Ding, F.; Zou, J., Theoretical and experimental study of highly textured GaAs on silicon using a graphene buffer layer. *J. Cryst. Growth* **2015**, *425*, 268-273.
156. Li, X.; Basile, L.; Huang, B.; Ma, C.; Lee, J.; Vlassiouk, I. V.; Puretzky, A. A.; Lin, M.-W.; Yoon, M.; Chi, M.; Idrobo, J. C.; Rouleau, C. M.; Sumpter, B. G.; Geohegan, D. B.; Xiao, K., Van der Waals Epitaxial Growth of Two-Dimensional Single-Crystalline GaSe Domains on Graphene. *ACS Nano* **2015**, *9* (8), 8078-8088.
157. Liu, Y.; Weinert, M.; Li, L., Spiral Growth without Dislocations: Molecular Beam Epitaxy of the Topological Insulator Bi₂Se₃ on Epitaxial Graphene/SiC(0001). *Phys. Rev. Lett.* **2012**, *108* (11), 115501.
158. Song, C.-L.; Wang, Y.-L.; Jiang, Y.-P.; Zhang, Y.; Chang, C.-Z.; Wang, L.; He, K.; Chen, X.; Jia, J.-F.; Wang, Y.; Fang, Z.; Dai, X.; Xie, X.-C.; Qi, X.-L.; Zhang, S.-C.; Xue, Q.-K.; Ma, X., Topological insulator Bi₂Se₃ thin films grown on double-layer graphene by molecular beam epitaxy. *Appl. Phys. Lett.* **2010**, *97* (14), 143118.
159. Litvinov, D.; O'donnell, T.; Clarke, R., In situ thin-film texture determination. *J. Appl. Phys.* **1999**, *85* (4), 2151-2156.
160. Mohanty, D.; Lu, Z.; Sun, X.; Xiang, Y.; Wang, Y.; Ghoshal, D.; Shi, J.; Gao, L.; Shi, S.; Washington, M.; Wang, G.-C.; Lu, T.-M.; Bhat, I., Metalorganic vapor phase epitaxy of large size CdTe grains on mica through chemical and van der Waals interactions. *Phys. Rev. Mater.* **2018**, *2* (11), 113402.
161. Abukawa, T.; Yamazaki, T.; Yajima, K.; Yoshimura, K., Weissenberg Reflection High-Energy Electron Diffraction for Surface Crystallography. *Phys. Rev. Lett.* **2006**, *97* (24), 245502.
162. Han, S. W.; Hwang, Y. H.; Kim, S.-H.; Yun, W. S.; Lee, J. D.; Park, M. G.; Ryu, S.; Park, J. S.; Yoo, D.-H.; Yoon, S.-P., Controlling ferromagnetic easy axis in a layered MoS₂ single crystal. *Phys. Rev. Lett.* **2013**, *110* (24), 247201.
163. Cai, L.; He, J.; Liu, Q.; Yao, T.; Chen, L.; Yan, W.; Hu, F.; Jiang, Y.; Zhao, Y.; Hu, T.; Sun, Z.; Wei, S., Vacancy-Induced Ferromagnetism of MoS₂ Nanosheets. *J. Am. Chem. Soc.* **2015**, *137* (7), 2622-2627.
164. Zheng, H.; Yang, B.; Wang, D.; Han, R.; Du, X.; Yan, Y., Tuning magnetism of monolayer MoS₂ by doping vacancy and applying strain. *Appl. Phys. Lett.* **2014**, *104* (13), 132403.
165. Bézout, E., *Théorie générale des équations algébriques*. Ph.-D. Pierres: 1779.

APPENDIX A: 1D INCOMMENSURATE DOMAIN MODEL - ANALYTICAL SOLUTION

Crystals formed by coalescence of different domains usually develop antiphase domains⁹.

If the domains do not rotate relative to each other, they are also called translational antiphase domains. Antiphase domains by definition refer to those with $\pi/2$ phase difference. However, this is only a special case when the lattice constant of the over layer is twice that of the substrate. A more general terminology for those kinds of domains are the so called incommensurate domains. Let's denote the base vectors of the epilayer and the substrate by \mathbf{b} and \mathbf{a} , respectively. Suppose the lattice constants of the epilayer and the substrate are rational numbers up to the experimental precision, then there must exist two coprime integers B and A such that:

$$B\mathbf{b} = A\mathbf{a}. \quad (\text{A.1})$$

For any two lattice points in the epilayer, their coordinates are:

$$\mathbf{r}_i = n_i\mathbf{a} + v_i\mathbf{b}, \quad (\text{A.2a})$$

$$\mathbf{r}_j = n_j\mathbf{a} + v_j\mathbf{b}. \quad (\text{A.2b})$$

Their relative position vector is:

$$\begin{aligned} \Delta\mathbf{r} &= \mathbf{r}_i - \mathbf{r}_j \\ &= (n_i - n_j)\mathbf{a} + (v_i - v_j)\mathbf{b} \\ &= \Delta n\mathbf{a} + \Delta v\mathbf{b} = (\Delta nB + \Delta vA)\mathbf{b}/A. \end{aligned} \quad (\text{A.3})$$

At the boundary, the distance between the two lattice points must be equal or larger than b but smaller than $2b$, or namely:

$$b \leq |\Delta\mathbf{r}| = (\Delta nB + \Delta vA)b/A < 2b. \quad (\text{A.4})$$

Therefore,

$$A \leq \Delta nB + \Delta vA < 2A. \quad (\text{A.5})$$

Since Δn , Δv can be any integer numbers and A, B are coprime numbers, according to Bézout's identity¹⁶⁵, for any integer d , there exists integers Δn and Δv such that $\Delta nB + \Delta vA = d$. Thus, under the constrain of Eq. (A.5), in total $\Delta nB + \Delta vA$ can take A possible integer values. This means that there will be a total of A kinds of boundaries and the length of the gap at the boundary will be $(1 + n/A)b$, where $n = 0, 1, 2, \dots, A-1$, if $B\mathbf{b} = A\mathbf{a}$. The solution to the equation $\Delta nB + \Delta vA = n$ can be represented by:

$$(\Delta n, \Delta v) = (n\Delta n_0 - nkA, n\Delta v_0 + nkB), \quad (\text{A.6})$$

where Δn_0 and Δv_0 satisfy $\Delta n_0B + \Delta v_0A = 1$ and k is an arbitrary integer. The A possible n values, however, occur with different possibilities. The probability $P(n)$ of getting n that satisfies:

$$\begin{cases} \Delta nB + \Delta vA = n \\ A \leq n < 2A \end{cases}, \quad (\text{A.7})$$

is therefore given by:

$$P(n) = \frac{\frac{1}{nAnB}}{\sum_{i=A}^{2A-1} \frac{1}{i^2AB}} = \frac{\frac{1}{n^2}}{\sum_{i=A}^{2A-1} \frac{1}{i^2}} = \frac{1}{n^2(H_{2A-1,2} - H_{A-1,2})}, \quad (\text{A.8})$$

where $H_{n,2} = \sum_{k=1}^n \frac{1}{k^2}$ is the second order generalized harmonic number.

In the case of monolayer MoS₂ grown on a sapphire substrate, both the MoS₂ and sapphire have the hexagonal structure. The in-plane lattice constants of MoS₂ and sapphire(0001) are $b = 3.15 \text{ \AA}$ and $a = 4.76 \text{ \AA}$, respectively. The lattice mismatch is $\sim 34\% = (4.76 - 3.15)/4.76$. It's easy to find that $68 \times 3.15 = 45 \times 4.76$, so $B = 68$ and $A = 45$. Therefore, there are 45 different kinds of boundaries. Figure A1(a) is a schematic of the one-dimensional atomic ball model showing an MoS₂ overlayer on the sapphire substrate without any boundary. Figures A1(b), (c), and (d) are one-dimensional models illustrating some possible domain boundaries. The dashed lines indicate the positions where the epilayer site and the substrate site line up.

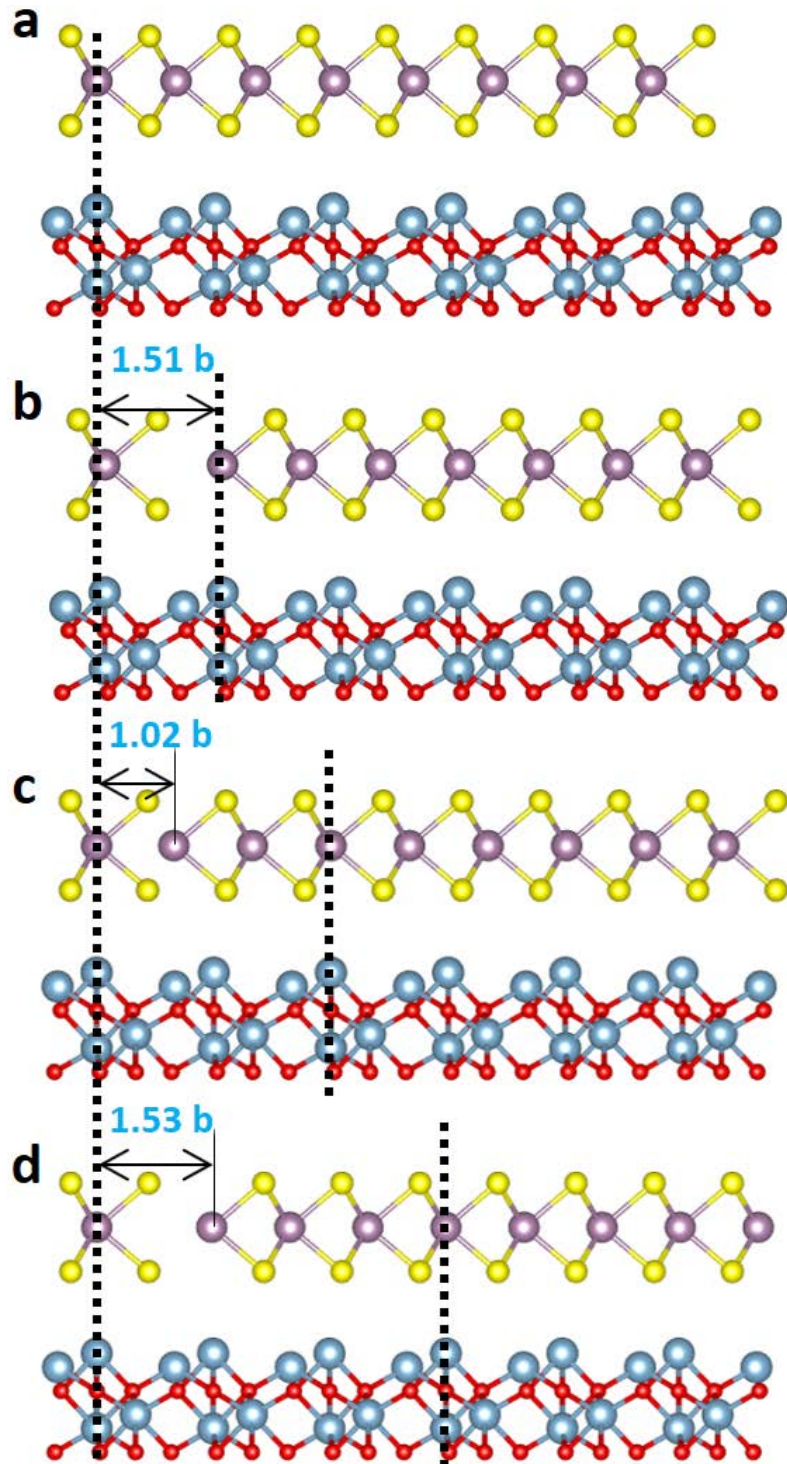


Figure A1: Schematics of some different types 1D incommensurate domain boundaries for MoS_2 forming parallel epitaxy with sapphire substrate with (a) no boundary, (b) boundary gap $= 1.51 b$, (c) boundary gap $= 1.02 b$ and (d) boundary gap $= 1.53 b$, where b is the MoS_2 lattice constant $b = 3.15 \text{ \AA}$. The vertical dashed lines represent where the epilayer lattice and substrate lattice line up.

The diffracted intensity from a one-dimensional randomly nucleated domains with a geometrical size distribution can be written as⁹¹:

$$I(x) = \frac{1 - f_b^2}{1 + f_b^2 - 2f_b \cos(2\pi x)}, \quad (\text{A.9})$$

where $f_b(x)$ is called the boundary structure factor and is given by:

$$f_b(x) = 1 - \gamma_b + \gamma_b \left\{ \sum_{n=0}^{A-1} \cos [2\pi(1 + n/A)x] P(n) \right\}, \quad (\text{A.10})$$

where $x = \mathbf{k} \cdot \mathbf{b}/2\pi$, γ_b is the probability of encountering a boundary when moving from one lattice to the adjacent one and $P(n)$ is defined in Eq. (A.8). Note that in the original work by Lu *et al.*, different types of boundaries are assumed to have equal probabilities. However, the larger gaps are less probable, that's why I/A is replaced with $P(n)$ here. According to the definition of γ_b , it is seen that the average domain size is b/γ_b . In Eq. (A.10), the intensity of the (00) diffraction spot diverges at $x = 0$, so the HWHM of the peak at $x = 0$ is left undetermined.

APPENDIX B: 2D INCOMMENSURATE DOMAIN MODEL - NUMERICAL SIMULATION

In the 2D case, denote the base vectors of the epilayer and the substrate as \mathbf{b}_1 , \mathbf{b}_2 and \mathbf{a}_1 , \mathbf{a}_2 , respectively. Similarly, we have:

$$B_1 \mathbf{b}_1 = A_1 \mathbf{a}_1, \quad (\text{B. 1a})$$

$$B_2 \mathbf{b}_2 = A_2 \mathbf{a}_2. \quad (\text{B. 1b})$$

And

$$\mathbf{r}_i = n_i \mathbf{a}_1 + m_i \mathbf{a}_2 + \nu_i \mathbf{b}_1 + \mu_i \mathbf{b}_2, \quad (\text{B. 2a})$$

$$\mathbf{r}_j = n_j \mathbf{a}_1 + m_j \mathbf{a}_2 + \nu_j \mathbf{b}_1 + \mu_j \mathbf{b}_2. \quad (\text{B. 2b})$$

$$\Delta \mathbf{r} = \left(\frac{\Delta n B_1}{A_1} + \Delta \nu \right) \mathbf{b}_1 + \left(\frac{\Delta m B_2}{A_2} + \Delta \mu \right) \mathbf{b}_2. \quad (\text{B. 3})$$

Suppose both epilayer and the substrate have hexagonal lattices, $|\mathbf{b}_1| = |\mathbf{b}_2| = b$ and $|\mathbf{a}_1| = |\mathbf{a}_2| = a$, the angle between base vectors is 60° . Thus Eq. (B.3) can be simplified as:

$$\Delta \mathbf{r} = (\Delta n B + \Delta \nu A) \mathbf{b}_1 / A + (\Delta m B + \Delta \mu A) \mathbf{b}_2 / A. \quad (\text{B. 4})$$

Substituting $\Delta n B + \Delta \nu A = n$ and $\Delta m B + \Delta \mu A = m$ into Eq. (B.4):

$$|\Delta \mathbf{r}| = \frac{b}{A} \sqrt{n^2 + m^2 + nm}. \quad (\text{B. 5})$$

By requiring that $b \leq |\Delta \mathbf{r}| < 2b$, we have:

$$A^2 \leq n^2 + m^2 + nm < 4A^2. \quad (\text{B. 6})$$

This is a second order Diophantine inequality. The existence of solution as well as the number of solutions to this inequality are very difficult to be expressed in an analytical form. However, we can determine the upper bound of the number of solutions to be $3A^2$. This means that in the 2D case, there will be at most $3A^2$ different types of boundaries.

Since it is difficult to proceed with the analytical derivation, we have instead switched to the numerical route starting from the nucleation of epilayer on the substrate. For this numerical simulation, the following assumptions are made:

1. Nucleation sites on the substrate are completely random.
2. Growth front of each domain is isotropic.
3. The epilayer grows only laterally, the nucleation centers do not shift during the growth.
4. Domains meet with each other at the domain boundaries and stop further growth there.

The process goes as following: First, read the structure of the epilayer and the substrate from the corresponding crystal information files (CIF). The information to be used are the in-plane lattice constants of the epilayer (b_1, b_2, θ_b) and the substrate (a_1, a_2, θ_a). Then generate the substrate lattice with the given shape (s) and diameter (D). This step will yield N (the total number of substrate lattice points) pairs of (x_i^S, y_i^S, z_i^S) coordinates for all the substrate lattice points. After that, nucleation sites (x_i^N, y_i^N, z_i^N) are chosen randomly from the N substrate sites with the given nucleation density ρ . The total number of nucleation sites would then be ρN . Next, a Voronoi diagram is created from the ρN nucleation sites. The output of this step includes the area of each domain (S_i) and the vertices (v_i^1, v_i^2) defining each domain boundary. From the collection of $N S_i$ values, we can get the domain size distribution. Each domain is then filled with the epilayer lattice points within the boundaries defined by the vertices under certain rules: (1) the epilayer and the substrate lattices coincide at (x_i^N, y_i^N, z_i^N) site in each domain. (2) the epilayer and the substrate lattices align parallel to each other. (3) the distance (r) between any two lattice points must satisfy:

$$\min(b_1, b_2) \leq r < 2 \max(b_1, b_2). \quad (\text{B.7})$$

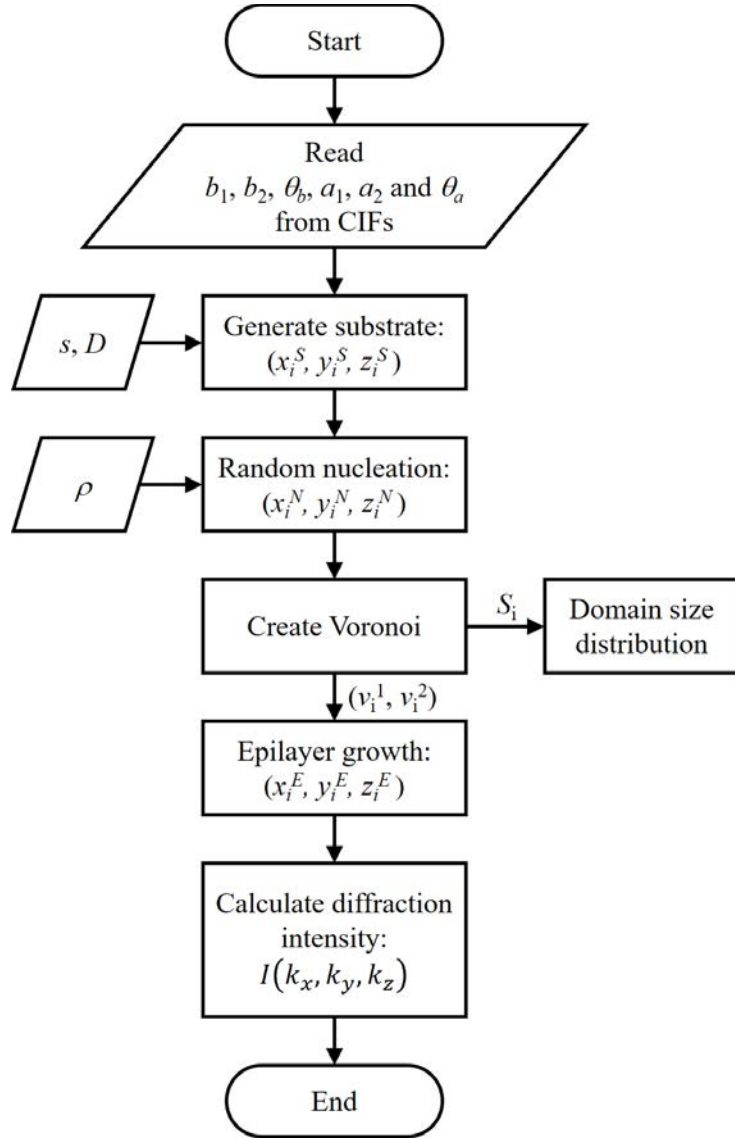


Figure B1: A flowchart for the numerical simulation used in the 2D incommensurate domain model.

After that, we obtain the coordinates of all epilayer lattice points (x_i^E, y_i^E, z_i^E) . Finally, the diffraction intensity is calculated from those lattice points kinematically using:

$$I(k_x, k_y, k_z) = \left| \sum_j f_i e^{i(k_x \cdot x_j^E + k_y \cdot y_j^E + k_z \cdot z_j^E)} \right|^2, \quad (\text{B.8})$$

where f_i is the atomic form factor, which is assumed to be a constant.

This process of this simulation is illustrated in the flowchart shown in Figure B1.

APPENDIX C: EFFECT OF INNER POTENTIAL ON THE RHEED PATTERNS

Let's denote the electron wave vectors inside and outside the crystal as K and k , respectively. The outside wave vector k , is related to the incident electron energy E_0 by:

$$E_0 = \frac{\hbar^2 k^2}{2m}. \quad (\text{C. 1})$$

When the electrons enter the crystal, they gain an energy of eV_I , where V_I is the inner potential. Therefore:

$$\frac{\hbar^2 K^2}{2m} = \frac{\hbar^2 k^2}{2m} + eV_I. \quad (\text{C. 2})$$

It is more convenient to define a quantity U that satisfy:

$$U = \frac{2meV_I}{\hbar^2}. \quad (\text{C. 3})$$

Therefore, the magnitudes of the electron wave vectors inside and outside the crystal are related by:

$$K^2 = k^2 + U. \quad (\text{C. 4})$$

A schematic showing the incident and the refracted electron beams are shown in Fig. C1. Note that in the real RHEED geometry, the intensity on the center streak is diffracted from planes slightly tilted from the sample surface plane due to the finite radius of the Ewald sphere. Since the parallel component of the electron wave vector is conserved:

$$k \cdot \cos\theta_1 = K \cdot \cos\theta'_1, \quad (\text{C. 5a})$$

$$K \cdot \cos\theta'_1 = k \cdot \cos\theta_2. \quad (\text{C. 5b})$$

According to the Bragg condition for diffraction (which takes place inside the crystal):

$$2d_{hkl} \cdot \sin \frac{\theta'_1 + \theta'_2}{2} = \lambda = \frac{2\pi}{K}. \quad (\text{C. 6})$$

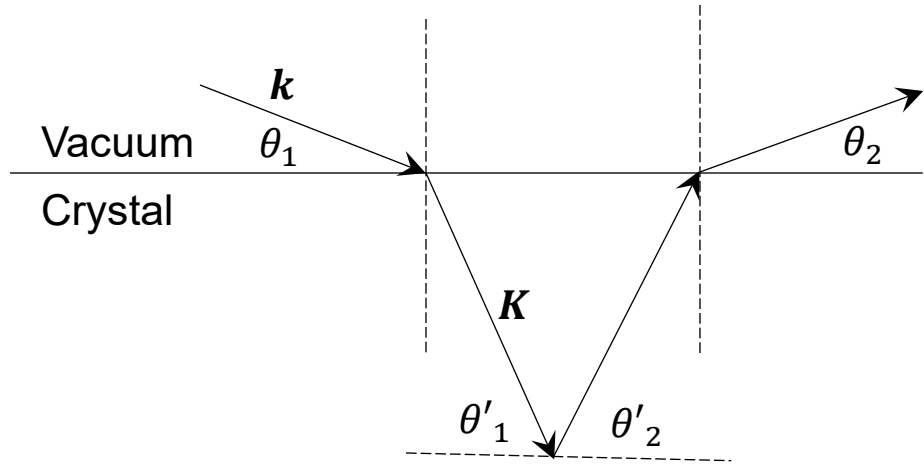


Figure C1: A schematic showing the RHEED geometry. \mathbf{K} and \mathbf{k} are the electron wave vectors inside and outside the crystal, respectively. θ_1 is the incident angle and θ_2 is the outgoing angle from the crystal surface. θ'_1 and θ'_2 are the incident angle and outgoing angle, respectively, from the plane by which the electron beam is diffracted inside the crystal.

Combining the above equations, one can express θ_2 in terms of θ_1 , E_0 and V_I for the $(00l)$ reflections as:

$$\theta_2^{00l} = \text{ArcCos} \left\{ \sqrt{\frac{E_0 + eV_I}{E_0}} \cos \left[\text{ArcCos} \left(\sqrt{\frac{E_0}{E_0 + eV_I}} \cos \theta_1 \right) - 2 \text{ArcSin} \left(\frac{0.015 \cdot l}{\sqrt{E_0 + eV_I}} \right) \right] \right\}. \quad (\text{C. 7})$$

APPENDIX D: HRLEED PATTERN AND IV SIMULATION FROM MONOLAYER CADMIUM TELLURIDE

As was predicted by Lucking *et al.*¹⁴⁶, conventional 3D materials such as CdTe could stabilize in DLHC structure. HRLEED would be an excellent tool to carry out an *in situ* study of the growth and structure of this material. While a dynamic LEED theory is necessary to describe the dependence between geometric atomic structure in the unit cell and the intensity³⁵, we can still qualitatively determine what the HRLEED pattern and IV curve would look like through a kinematic approximation because the multiple scattering which gives rise to the dynamical effects will never modify the spot positions on the HRLEED 2D map¹²⁰.

Three possible structures for a monolayer CdTe have been used for the simulation: zincblende ($a = b = 4.58 \text{ \AA}$, $c = 11.22 \text{ \AA}$, $\gamma = 120^\circ$), hexagonal ($a = b = 4.68 \text{ \AA}$, $c = 7.67 \text{ \AA}$, $\gamma = 120^\circ$) and DLHC ($a = b = 4.64 \text{ \AA}$, $c = 14.32 \text{ \AA}$, $\gamma = 120^\circ$). Atomic ball models of each structure are presented in Figs. D1(a), (b) and (c) in cross-section view and Figs. D1(d), (e) and (f) in top view. According to the kinematic diffraction theory, the diffraction intensity is proportional to the magnitude square of the structure factor. The simulated HRLEED patterns at $k_\perp = 0.84 \text{ \AA}^{-1}$ corresponding to zincblende, hexagonal and DLHC structures are shown in Figs. D1(g), (h) and (i), respectively. From the simulated patterns, we can conclude that both zincblende and DLHC structures are 3-fold symmetric, while the hexagonal structure has an exact 6-fold symmetry. This immediately gives us a way to tell the DLHC structure apart from the hexagonal structure.

Figures D2 shows the simulated IV curves from the three structures. The second peak positions are at 1.53 \AA^{-1} , 1.50 \AA^{-1} and 1.77 \AA^{-1} for zincblende, hexagonal and DLHC structures, respectively, as are labeled on Fig. D2. The IV curves from zincblende and hexagonal

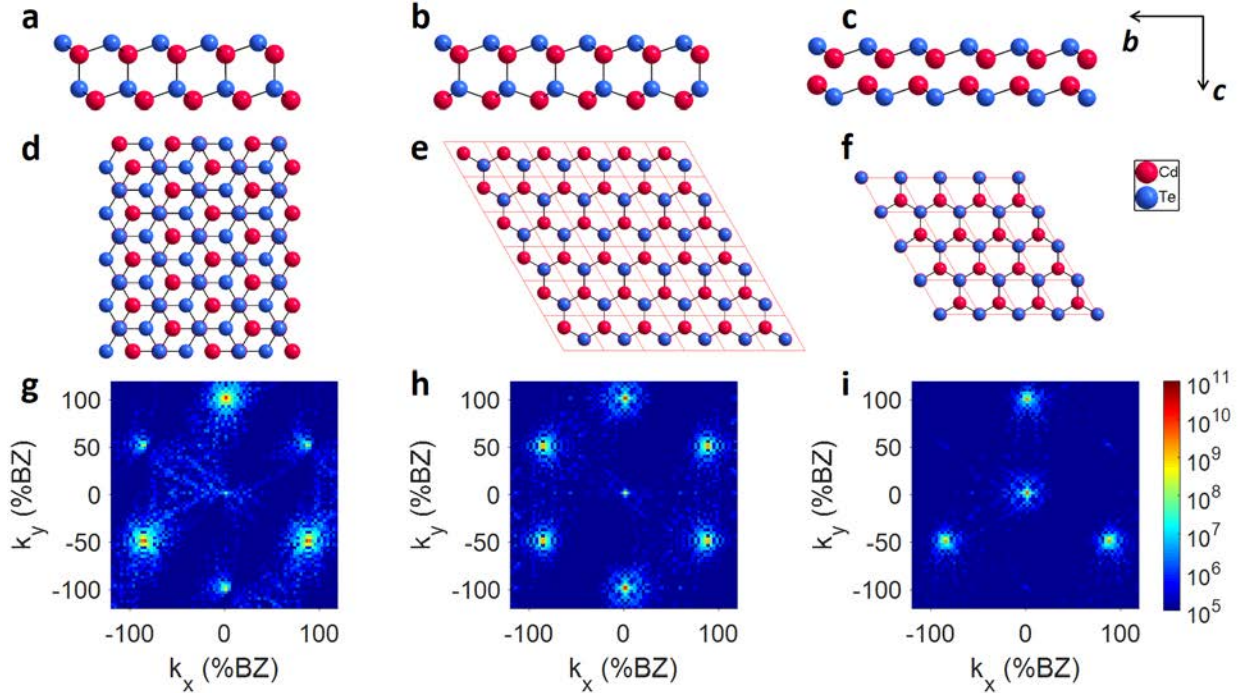


Figure D1: Cross-section view atomic ball models for monolayer CdTe in (a) zincblende, (b) hexagonal and (c) DLHC structures. Top-view atomic ball models for monolayer CdTe in (d) zincblende, (e) hexagonal and (f) DLHC structures. The two arrows on the top-right corner indicate the directions of CdTe base vectors b and c . Simulated HR-LEED patterns for monolayer CdTe in (g) zincblende, (h) hexagonal and (i) DLHC structures.

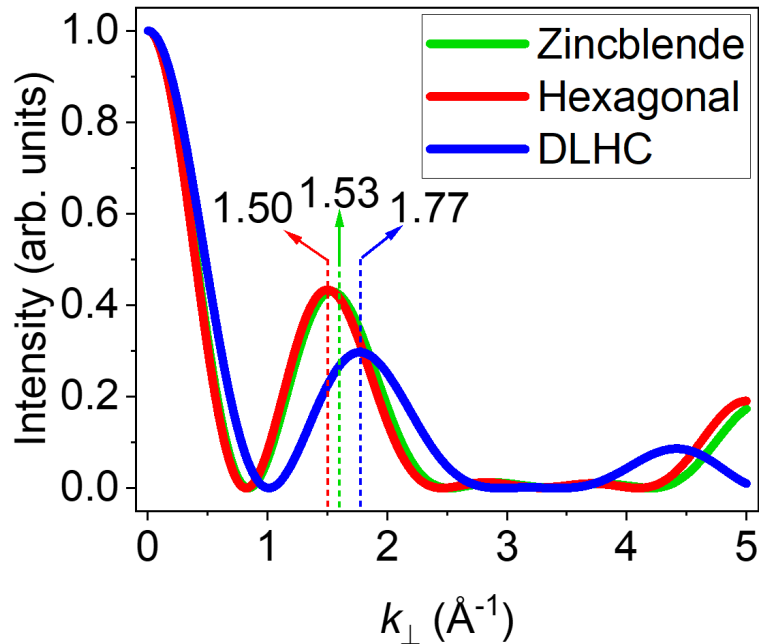


Figure D2: Simulated I-V curves for monolayer CdTe in zincblende, hexagonal and DLHC structures. The center positions of some peak in the simulated curves are labeled on the figure.

structures are almost the same, while that from DLHC is quite different. The center position of the second peak in the IV from DLHC structure differs by ~16 % from the zincblende and hexagonal structure. This makes it possible for us to distinguish DLHC from the other two. Combining the HRLEED pattern and the IV curve, we can determine what is the atomic structure of the CdTe film.